Antihydrogen via Two-Stage Charge Exchange

Daniel Fitzakerley

A DISSERTATION SUBMITTED TO THE FACULTY OF GRADUATE STUDIES IN PARTIAL FULFILLMENT OF THE REQUIREMENTS FOR THE DEGREE OF

GRADUATE PROGRAM IN DEPARTMENT OF PHYSICS AND ASTRONOMY
YORK UNIVERSITY
TORONTO, ONTARIO
September 2015

Abstract

This thesis describes positron and antihydrogen research performed at CERN in the context of the ATRAP collaboration. Positrons emitted from a radioactive source are moderated in a layer of frozen neon. The rate at which slow positrons exit the moderating material is precisely determined. The slow positrons are trapped in a differentially pumped Penning trap. Large numbers of positrons are accumulated and transferred into a cryogenic Penning trap at a record rate. Plasmas of up to 4×10^9 positrons are created — the largest number of positrons ever held in a single trap. Counting techniques for positron and electron plasmas are compared, validating the charge-counting techniques used for each. Positron plasmas are compressed using rotating electric fields in preparation of antihydrogen production experiments. Antihydrogen atoms are created via laser-controlled, two-stage charge exchange. These antihydrogen atoms, approximately 2000 per trial, should be created with low enough energy so that some of them can be confined in a magnetic quadrupole or octupole trap. The goal of ATRAP is to precisely measure the spectroscopy of these trapped antihydrogen atoms, and compare it to the spectroscopy of hydrogen to test CPT and Lorentz invariance.

For my family

Acknowledgements

More people than I could ever possibly count have had a hand in my success, both inside and outside of the AD. Thank you to everyone thats been a part of my life. The smallest interactions between two people can change their paths in life. Even if youre not mentioned below, please know that I wouldnt be the person I am today without all of you.

To my partner Brittany, thank you for giving me a reason to leave the lab and for supporting me when I couldnt. I would never have been able to accomplish so much without you. Thank you for giving me a family.

To my parents, thank you for your never-ending support, love, and unlimited space in your suitcases for maple syrup.

To my supervisor Prof. Eric, Hessels, thank you for taking a chance on a wide-eyed graduate with a big smile. You gave me an amazing opportunity and the encouragement to apply myself and reach my goals. Thank you for surrounding me with talented graduate students and post-docs. Thank you for your patience.

Thank you to all my colleagues at York University. To Joe Borbely and Matthew George, for showing me the ropes in the helium lab and teaching me, by thorough example, how to be a precision experimentalist. To Cody Storry and Matthew Weel in the positron lab, for taking any positron-related calls for five years and for dropping everything and flying out to CERN in a pinch. Thank you for your work-ethic, Cody. It's infectious.

Thank you to my friends and colleagues in the AD. I never would have imagined working with such talented physicists, and then becoming such good friends. Thanks to Rob McConnell and Steve Kolthammer. I learned so much working alongside you both. Many of the results presented in this thesis were built on foundations you created. Thanks to Phillip Richerme for countless conversations about Penning-trap physics, for trapping antihydrogen, and for being streets ahead. Thanks to Andreas Muellers for being my partner in all things cesium, for 200 mW of 511-nm light, and for introducing me to the world of German candy.

Thank you to Prof. Jerry Gabrielse for creating this collaboration and allowing me to be a part of it. ATRAP is made up of brilliant graduate students and principal

investigators with many years of experience in experimental physics, and I have learned more in the course of my thesis work than I imagined possible.

Thank you to the ATRAP collaborators from Forschungszentrum Jülich, particularly Prof. Walter Oelert and Dieter Grzonka. In addition to keeping the ATRAP detectors running efficiently, your many trips to CERN were much-needed boosts to the moral of the team in some of the darker days of CTRAP construction. Thank you both for your hard work, light hearts, and candid conversations. Thank you to Eric Tardiff and Stephan Malbrunot, the most recent ATRAP postdocs. Thank you for sharing your wealth of experience in other areas of physics and for defining the word clean.

And finally, thank you to Nathan Jones, Christopher Hamley, and Taylor Skinner for carrying the ATRAP torch into the future. I wish you all the best of luck.

Contents

List of Tables

List of Figures

Chapter 1

Introduction

1.1 CPT Symmetry

A CPT transformation is the combination of charge conjugation, parity inversion, and time reversal — each particle in a system is replaced with its antiparticle, and time and space coordinates are reversed. The CPT theorem states that all physical laws must be invariant under CPT transformations, and thus that CPT is an exact symmetry of nature. It has been proven [1] that quantum field theories that are CPT-invariant are also Lorentz invariant and that if CPT symmetry is broken, then experimental results would not be independent of the orientation or velocity of the laboratory — which would be a strange result, indeed. Each individual symmetry (C, P, and T) was at one point thought to be invariant, until experimentally proven otherwise.

Even though each element of CPT symmetry can be broken, it is thought that the three symmetries can break in just the right way to preserve CPT symmetry as a whole. Testing the invariance of CPT symmetry is a prime motivation for this work, as well as other antimatter experiments. Finding that CPT-symmetry is

broken in our universe would challenge one of the strongest pillars of the Standard Model of particle physics.

Many experiments comparing matter and antimatter have been performed to test the CPT theorem. Particle and antiparticle masses, charge-to-mass ratios, lifetimes, and magnetic moments should be identical while atoms and antiatoms should have the same internal structure. A summary of these comparisons [2] is shown in Figure 1.1, alongside the potential precision that a hydrogen-antihydrogen comparison could reach. The hydrogen-antihydrogen comparison could become the secondmost precise test of CPT and the only measurement performed in a mixed lepton-baryon system.

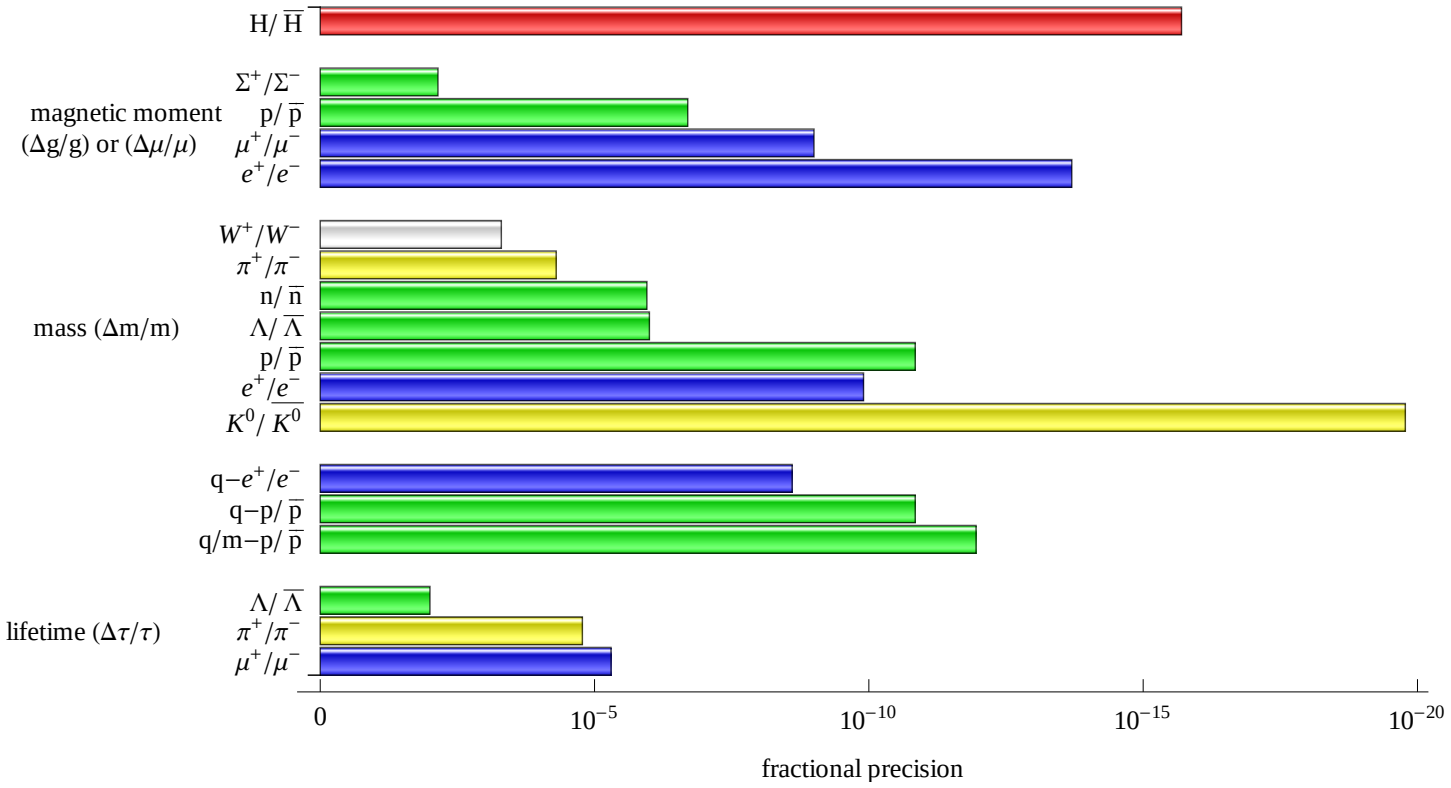

FIGURE 1.1: Precision of CPT-violation measurements [2] in different particle systems: Leptons (blue), mesons (yellow), baryons (green), bosons (white), and the potential antihydrogen measurement (red) which would result if antihydrogen could have its spectroscopy measured to the same precision as hydrogen.

1.2 Antihydrogen

To date, CPT-testing antimatter experiments measure either leptons or baryons, never a system including both. Since there is no indication of where to expect CPT symmetry to be broken, experiments must be performed to compare as many matter-antimatter pairings as possible. Hydrogen (H) and its antimatter counterpart antihydrogen ($\overline{\mathrm{H}}$) — a bound system of a positron (e^+) and antiproton ($\bar{\mathrm{p}}$) — could be compared through measurements of their internal structures. Many decades of work has led to the development of techniques used to create $\overline{\mathrm{H}}$.

1.3 A Brief History of Antimatter

The e^+ (and antimatter in general) was first postulated by Dirac in 1928. In an attempt to unify quantum mechanics, special relativity, and particle spin, Dirac introduced both positive and negative energy solutions to his Dirac equation. It was not until 1931 that Dirac attributed these negative energy states to an undiscovered e^+ particle. Positrons were observed by C. Anderson in 1932 [3], and he won the Nobel prize in 1936 for their discovery. Positrons have been trapped and used in precision experiments in high-vacuum Penning traps since 1981 [4].

Dirac's negative-energy solutions apply to all particles. Therefore, not only the antielectron, but also the antiproton ($\bar{\mathrm{p}}$), should exist. The $\bar{\mathrm{p}}$ was discovered in 1955 at UC Berkeley by Segrè and Chamberlain [5]. The Bevatron, the largest particle accelerator in the world at the time, collided 6-GeV protons with a stationary target to provide just enough energy to create antiprotons. Antiprotons produced via high-energy proton collisions result in high-energy $\bar{\mathrm{p}}$ that are difficult to trap. Overcoming these difficulties, Gabrielse *et al* successfully trapped $\bar{\mathrm{p}}$ in a Penning trap at LEAR (Low Energy Antiproton Ring at CERN) in 1986 [6]. The

3-MeV $\bar{p}$ were decelerated in a beryllium foil and then caught in a 3-keV-deep electrostatic potential well.

The first production [7] and observation of $\overline{H}$ also took place at LEAR in 1995. Nine $\overline{H}$ atoms were produced at nearly the speed of light. This was a milestone in the history of antimatter research and made many future experiments, including the construction of the CERN Antiproton Decelerator (AD), possible, while spurring worldwide interest in antimatter research. With the construction and commissioning of the AD, large numbers of relatively slow $\bar{p}$ became available for $\overline{H}$ production. ATRAP demonstrated large numbers of trapped $\bar{p}$ in 2002 [8] and, along with its competitor ATHENA, demonstrated $\overline{H}$ production in a Penning trap [9] [10].

In 2010 and 2012, ALPHA [11] and ATRAP [12] demonstrated the ability to trap small numbers of $\overline{H}$ at the magnetic field minimum of a magnetic gradient trap. The $\overline{H}$ atoms could be held for hundreds of seconds in the magnetic gradient trap — long enough to allow for possible precision spectroscopy measurements. The first interaction with the internal structure of $\overline{H}$ has been performed by ALPHA using microwaves to flip the e^+ spin [13].

1.4 Motivation for $\overline{H}$ Research

1.4.1 Antigravity

Antihydrogen is electrically neutral, making it a candidate for a direct measurement of the force of gravity on antimatter to test the Weak Equivalence Principle, which states that the trajectory of a particle in a gravitational field depends only on its mass, initial position and velocity, and is independent of its composition and structure.

Indirect measurements of antigravity have already been performed. Neutrinos and antineutrinos originating in a supernova 164,000 light years away arrived within an approximately 10-s time window. The graviationally-induced time delay between a neutrino and antineutrino from this supernova is approximately $\frac{G-\overline{G}}{G} \times 6 \times 10^6$ s, where G is the gravitational constant for matter-matter interactions, and $\overline{G}$ is the constant for matter-antimatter interactions . Since the measured time delay is less than 10 s, the fractional difference between G and $\overline{G}$ is less than 10^{-6} [14], confirming the Weak Equivalence Principle to the stated precision. The neutrino detector used could, however, not reliably distinguish between neutrinos and antineutrinos, leaving some uncertainty in this test. Given the rarity of nearby supernovae, it is unlikely that a measurement like this will be performed again soon.

Another indirect test of the Weak Equivalence Principle uses measurements of p and $\bar{\text{p}}$ cyclotron frequencies in the same Penning trap. If antimatter is affected differently from matter in the gravitational field of the Earth, the $\bar{\text{p}}$ cyclotron frequency would be shifted from that of the p [15] [16]. This would amount to a frequency difference between a clock and its CPT conjugate in the same gravitational field. The p and $\bar{\text{p}}$ cyclotron frequencies are equal to a precision of 9×10^{-11}. Another test of antigravity lies in the comparison of the 1S-2S interval of hydrogen and positronium. The intervals are calculated in zero gravity and compared to experimental results. The calculated ratio of these two intervals agrees with the experimental ratio to within a few parts in 10^{-9} [17], indicating that the gravitational shifts are identical at this level.

Direct measurements of $\bar{\text{g}}$ (the acceleration due to gravity for antimatter) in a Penning trap are not yet very precise, but can put an upper limit on the difference between g and $\bar{\text{g}}$. To this end, ALPHA uses their position-sensitive detector to search for the propensity for $\overline{\text{H}}$ atoms to fall downward when released from a magnetic gradient trap. They can reject scenarios where the absolute value of $\bar{\text{g}}$

is more than 75 times stronger than g [18]. Clearly, these measurements need to be improved if direct measurements of antigravity are going to be useful. Two additional collaborations (AEgIS and GBAR) have begun operation in the CERN AD with the goal of directly measuring the gravitational acceleration of $\overline{\mathrm{H}}$, with the initial goal of a 1% precision measurement.

1.4.2 Spectroscopy

Spectroscopic measurements of $\overline{\mathrm{H}}$, compared with the same measurements of H, have the potential to make one of the most precise tests of CPT symmetry. Hydrogen is the simplest atomic system and its energy levels have been calculated to high precision. Theoretical and experimental advances continue to increase the level of precision possible in H spectroscopy [19]. The energy separation between the 1S and 2S states in H is now known to a precision of 4.2×10^{-15}, as measured in a cold atomic beam [20]. The hyperfine structure of ground-state H is also precisely known (to a relative precision of 7×10^{-13}) using a hydrogen maser [21]. Measurements of ground-state $\overline{\mathrm{H}}$ hyperfine-structure are being performed by the ASACUSA collaboration in the AD. ASACUSA will use cold $\overline{\mathrm{H}}$ that are synthesized in a cusp trap [22] and produce a slow beam of $\overline{\mathrm{H}}$ for spectroscopy. H and $\overline{\mathrm{H}}$ 1S-to-2S energy splittings are predominantly dictated by the electromagnetic interaction and the e^+ mass. Hyperfine structure is caused by the spin-spin interaction of the e^+ and $\bar{\mathrm{p}}$. Thus, the 1S-2S and Hyperfine-structure comparisons that test CPT symmetry involve different interactions.

1.5 The Antiproton Decelerator

The AD was built as a successor to LEAR and began operation in 2000. It is currently the world's only source of cold $\bar{\mathrm{p}}$. The starting point for the AD is

the Proton Synchrotron (PS). A beam of protons from the PS is aimed at an iridium target to produce $\bar{p}$. These $\bar{p}$ are moving at nearly the speed of light and with a wide range of energies. They enter the AD ring with a starting energy of approximately 2.7 GeV. The AD confines the $\bar{p}$ in a magnetic ring while applying stochastic and electron cooling. After 100 s of cooling and bunching, approximately 3.5×10^7 $\bar{p}$ are ejected from this ring with a momentum of 5.3 MeV/c [23].

ATRAP and two other international collaborations (ATHENA and ASACUSA) were the first to take advantage of the slow $\bar{p}$ provided by the AD. Since its founding in 2000, the AD has welcomed many more collaborations (ALPHA, AEgIS, ACE, and BASE) and with ELENA, a planned extension to the AD that will provide even slower $\bar{p}$, a proposal has been accepted for yet another collaboration (GBAR).

1.5.1 ATRAP in the AD

ATRAP has been using the slow $\bar{p}$ from the AD since its commissioning in 2000. The ATRAP installation now consists of two cryogenic Penning traps: A small-diameter trap in a 5-T superconducting solenoid, currently used for precise $\bar{p}$ magnetic moment measurements (located in Zone 1 of Figure 1.2) and a larger-diameter trap in a large-bore, 1-T superconducting solenoid for $\overline{H}$ experiments (located in Zone 2 of Figure 1.2). Additionally, a positron accumulator is in Zone 3.

1.5.2 ATRAP Positrons

ATRAP has changed and improved both its apparatus and its experimental techniques for trapping e^+ over the last decade. The first iteration of ATRAP used a completely-enclosed, small-diameter Penning trap. Positrons were loaded by field

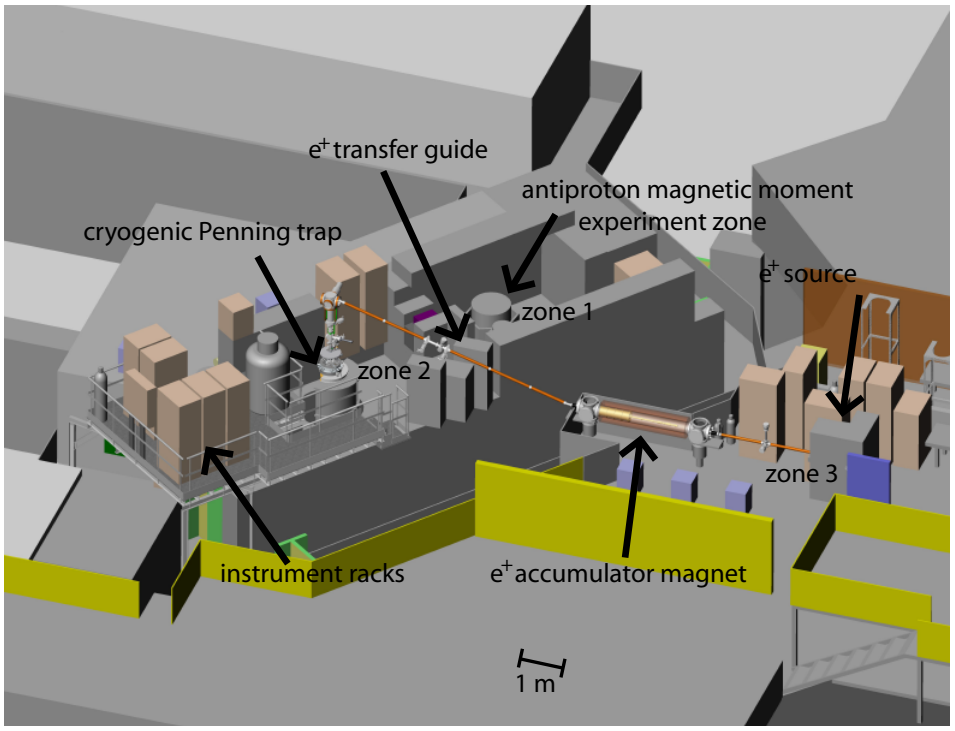

FIGURE 1.2: The three ATRAP zones used for positron production (zone 3), antihydrogen experiments (zone 2), and antiproton magnetic moment measurements (zone 1).

ionization of strongly magnetized Rydberg positronium [24]. Energetic e^+ entered the sealed Penning trap apparatus through a thin foil. The e^+ were slowed in a tungsten crystal, at the exit of which they picked up an e^- to form Rydberg positronium (Ps*). An applied electric field ionized the Ps*, and the resulting e^+ were captured. This method was effective, but slow (e^+ were often loaded overnight), and required the radioactive e^+ source to be moved into place above the cryogenic Penning trap. To improve e^+ load times, ATRAP now uses a Surko-style positron system [25]. Positrons emitted from a ^{22}Na source are slowed in a frozen neon moderator, captured through inelastic collisions with N_2 molecules and accumulated. This process accumulates e^+ 10^4 times faster and allows the radioactive source to remain stationary and well shielded. The new positron accumulator requires a magnetic transfer guide to transport the accumulated e^+ to the orthogonally oriented cryogenic Penning trap. The positron accumulator and e^+ transfer guide are described in Chapters 5 and 6, respectively.

1.6 Overview of this Work

This thesis discusses the production of thousands of $\overline{\mathrm{H}}$ atoms created via two-stage Rydberg charge exchange and the important contributions that the York positron accumulator has made towards this goal and towards the ATRAP physics program as a whole. Chapter 2 introduces the physics of single particles and plasmas in a Penning-Ioffe trap — the apparatus used for $\overline{\mathrm{H}}$ production and trapping. The ATRAP Penning-Ioffe trap is described in Chapter 3. Chapter 4 discusses particle counting techniques and measurements. Chapter 5 describes the York positron accumulator and details improvements in e^+ accumulation efficiency that have led to unprecedentedly large numbers of e^+ for use in $\overline{\mathrm{H}}$ production trials. Chapter 6 discusses the magnetic guide (the e^+ transfer guide) used to transfer e^+ from the York positron accumulator into the extremely-high-vacuum cryogenic Penning trap. Chapter 7 explains our particle loading techniques for e^+, e^- and $\bar{p}$. $\overline{\mathrm{H}}$ production via two-stage charge exchange is discussed in Chapter 8. Concluding remarks are made in Chapter 9.

1.7 Collaborative Nature of this Research

As with any large collaboration, it can be difficult to see the lines between where one individual's work begins and where the work of others ends. Building and operating a cryogenic Penning-Ioffe trap is an enormous task and each member of ATRAP takes part of that responsibility, and so each member takes some ownership of the scientific results. My tenure at ATRAP saw much success, including adiabatic cooling of antiprotons to 3.5 K [26], measurement of the centrifugal separation of $\bar{p}$ and e^- [27], trapping antihydrogen [12], and measurement of the magnetic moment of the antiproton [28]. And though I was an integral part of

the collaboration for this work, much more of the credit belongs to other members of ATRAP. As such, this thesis mainly focuses on work that is entirely, or mostly, my own. Chapter 5 contains a description of the positron accumulator, which was my first responsibility at ATRAP. Section 5.3.3 describes experiments I performed to precisely determine the rate of slow positrons entering the positron accumulation region. Many hours were spent understanding and optimizing the various stages of the positron accumulator, leading to a five-fold increase in the positron accumulation rate. By transferring these large accumulations of e^+ more frequently from the positron accumulator to the cryogenic Penning trap, I reached a e^+ loading rate of 2.2×10^4 e^+/s/mCi (the e^+ rate normalized to the e^+ source strength, in mCi) — the largest rate reported in literature.

The cryogenic Penning trap was built with segmented electrodes for the application of a rotating wall. The electronics and control software of the rotating wall and plasma diagnostic systems were predominantly the work of Dr. William Steven Kolthammer [29]. As Dr. Kolthammer focused on rotating walls to compress e^- and $\bar{p}$ plasmas, I focused on compressing e^+ plasmas to increase $\overline{H}$ production rates (Section 7.1.2). I also used these systems in an attempt to directly measure the temperature of e^+ plasmas in the cryogenic Penning trap, as discussed in Section 4.6.

The fast e^+ loading rate and rotating wall allowed me to trap approximately 4×10^9 e^+ in single potential well in the cryogenic Penning trap (Section 7.4.3) — the most e^+ held in a single Penning trap.

Section 4.4 details experiments I conducted to determine how accurately we count positrons by preparing and comparing identical positron and electron plasmas in the cryogenic Penning trap.

Finally, Section 8.2 discusses $\overline{H}$ production by two-stage Rydberg charge exchange. Much of the credit of this work belongs to Dr. Robert McConnell [30] who built the

charge exchange apparatus and Dr. Andreas Muellers [31] who built and operated the excitation lasers. For my part, I operated the cryogenic Penning trap, which included loading and preparing plasmas of e^-, $\bar{p}$, and e^+ and was in charge of upgrading instrumentation and computer automation.

The work presented in this thesis was accomplished during 2010 and 2011. Most of this work, particulary e^+ plasma temperature measurements in the cryogenic Penning trap (Section 4.6) and trapping $\overline{H}$ made via two-stage charge exchange (Section 8.2), was meant to continue into 2012 and beyond. However, from 2012, the ATRAP collaboration made the decision to focus all efforts on designing, constructing, and testing the next-generation cryogenic Penning-Ioffe trap. The first iteration of this new trap featured a nearly metal-free enclosure for the Ioffe trap. Unfortunately, the glue-joints that held the enclosure together could not withstand the stress of cooling to 4.2 K. After 18 months of construction, testing, and cool-down attempts that proceeded as slowly as 1 degree kelvin per hour, the nearly metal-free enclosure was abandonded in favour of a welded-titanium enclosure. This new titanium enclosure necessitated the production of a new electrode stack and two-stage charge exchange apparatus. Only at the very end of 2014 was the new cryogenic Penning-Ioffe trap assembled and successfully cooled to 4.2 K. I played a central role in cooling the trap, loading e^- into it, and performing a battery of tests to parameterize the new Ioffe trap and its enclosure.

Since my work on this new cryogenic Penning-Ioffe trap has not produced any new physics results, it is not presented in this thesis. I hope that my years of work to construct and test this new cryogenic Penning-Ioffe trap will provide many scientific results that will be presented in the theses of future ATRAP graduate students.

Chapter 2

Penning-Ioffe Traps

2.1 Penning-Ioffe Traps

Penning traps use electrostatic and magnetic fields to confine charged particles. The principle of confinement was invented by Penning in 1936 for use as a vacuum gauge [32]. This confinement principle was used for the purpose of long-term confinement of charged particles by Paul [33] and Dehmelt [34] three decades later. Modern Penning traps are used for a wide variety of precision experiments, including measurements of the e^- and e^+ g-factors and p and $\bar{p}$ magnetic moments [35].

2.1.1 Penning Traps

A basic Penning trap consists of a quadrupole electrostatic field superimposed with a uniform magnetic field. In early Penning trap designs, the electrostatic field was produced by three hyperbolic electrodes: a ring electrode and two endcap electrodes, as in Figure 2.1(a). These electrodes are used to create a potential [36]:

$$U(r,z) = U_0 \frac{z^2 - \frac{x^2+y^2}{2}}{2d^2}, \tag{2.1}$$

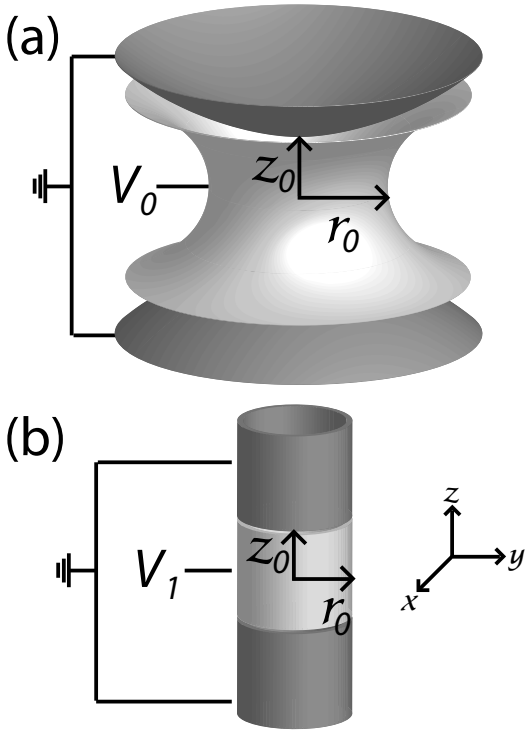

FIGURE 2.1: Hyperbolic (a) and hollow cylindrical (b) electrodes used in Penning traps.

where $d = \frac{1}{2}(z_0^2 + \frac{1}{2}r_0^2)$ is the trap's characteristic length scale, z_0 is the axial half-length, and r_0 is the radius, as shown in Figure 2.1. Hyperbolic electrodes are difficult to machine to a high precision and can get in the way of particle loading and detection.

Fortunately, it is possible to create approximately the same potential using a series of hollow cylindrical electrodes [37], such as in Figure 2.1(b). Cylindrical electrodes are far easier to machine to high precision. Since there is no need for an endcap electrode, loading and interacting with particles and ions is more straight forward, with particle loading, laser admittance, and fluorescence detection all done axially.

The potential near the center axis of such a series of cylindrical electrodes can be written as an expansion of Legendre polynomials [38]

$$U = \frac{1}{2}U_0 \sum_{k=0}^{\infty} D_{2k} \left[\frac{r}{d}\right]^{2k} P_{2k}(\cos\theta), \tag{2.2}$$

where r and θ are spherical coordinates. The symmetry of the apparatus about the $z = 0$ plane removes the odd terms from the expansion. Here, D_2 is the quadrupole coefficient, and all higher order coefficients determine deviations from a perfectly harmonic potential well of equation (2.1). By clever choices of electrode lengths and potentials it is possible to eliminate the D_4 and D_6 coefficients. Higher-order terms are much smaller, and thus cylindrical electrodes can be used to produce potential wells equally suitable for precision measurements as those produced by hyperbolic electrodes.

The cylindrical electrode assembly is also extendable. With a long enough stack of cylindrical electrodes, each independently biased, it is possible to confine ions of opposite charge (e^+ and $\bar{p}$, for example) in nested potential wells.

The axial magnetic field $\vec{B} = B_0\hat{z}$ is produced by a solenoidal electromagnet, often with extra shimming magnets to reach high field uniformity near the central region of the solenoid.

2.1.2 Single Particle in a Penning Trap

A particle with mass m and charge q moving in the combined electrostatic and magnetic fields of the Penning trap experiences a force

$$\vec{F} = m\frac{\mathrm{d}^2\vec{r}}{\mathrm{d}t^2} = -q\nabla\Phi + q(\vec{v}\times\vec{B}), \tag{2.3}$$

where $\Phi = U/q$ is the electrostatic potential, $\vec{v}$ is the velocity of the charged particle, and $\vec{B} = B_0\hat{z}$.

The equations of motion are

$$\frac{\mathrm{d}^2x}{\mathrm{d}t^2} - \omega_c\frac{\mathrm{d}y}{\mathrm{d}t} - \frac{1}{2}\omega_z^2 x = 0, \tag{2.4}$$

$$\frac{\mathrm{d}^2y}{\mathrm{d}t^2} + \omega_c\frac{\mathrm{d}x}{\mathrm{d}t} - \frac{1}{2}\omega_z^2 y = 0, \tag{2.5}$$

$$\text{and} \qquad \frac{\mathrm{d}^2z}{\mathrm{d}t^2}\omega_z^2 z = 0, \tag{2.6}$$

where $\omega_c = qB_0/m$ is the free-particle cyclotron frequency and $\omega_z = \sqrt{2U_0/md^2}$ is the axial frequency that describes a simple harmonic oscillation along the z direction. The motion in the z direction is completely decoupled from motion in the x and y directions. A complex variable $u = x + iy$ can be introduced to simplify the equations of motion in the x and y directions, resulting in

$$\frac{\mathrm{d}^2u}{\mathrm{d}t^2} + i\omega_c\frac{\mathrm{d}u}{\mathrm{d}t} - \frac{1}{2}\omega_z^2 u = 0, \tag{2.7}$$

which has the general solution $u = e^{-i\omega t}$. The radial equation of motion then reduces to

$$\omega^2 - \omega_c\omega + \frac{1}{2}\omega_z^2 = 0, \tag{2.8}$$

which has solutions:

$$\omega_+ = \frac{1}{2}(\omega_c + \sqrt{\omega_c^2 - 2\omega_z^2}) \qquad , \qquad \omega_- = \frac{1}{2}(\omega_c - \sqrt{\omega_c^2 - 2\omega_z^2}), \tag{2.9}$$

where ω_+ is the modified cyclotron frequency, which we will denote by $\bar{\omega}_c$, and ω_- is the magnetron frequency, which we will denote by ω_m. The solutions to equation (2.8) must be real, leading to the requirement:

$$\bar{\omega}_c^2 - 2\omega_z^2 > 0. \tag{2.10}$$

Substituting the frequencies for their values based on the trap parameters leads to the confinement condition:

$$\frac{q}{m}B_0^2 > \frac{4U_0}{d^2} \qquad , \qquad U_0 > 0. \tag{2.11}$$

For reasonable choices of trap parameters, $\omega_c \gg \omega_z \gg \omega_m$, meaning that the modified cyclotron frequency is very close to the natural cyclotron frequency. This frequency hierarchy leads to the total combined motion of a single particle in a Penning trap shown in Figure 2.2.

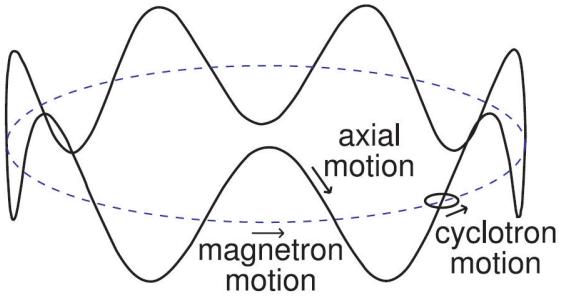

FIGURE 2.2: Single particle motion in a Penning trap.

2.1.3 Synchrotron Cooling

As a result of the motion discussed in the previous section, a charged particle in a Penning trap is constantly accelerating and therefore losing energy to synchrotron radiation. The energy loss is predominantly due to the cyclotron motion since $\omega_c \gg \omega_z \gg \omega_m$. The Larmor formula gives the power radiated by an accelerating charge:

$$\frac{dE}{dt} = -\frac{q^2}{6\pi\epsilon_0 c^3}|\frac{d^2\vec{r}}{dt^2}|^2. \tag{2.12}$$

The Lorentz force is used to solve for the acceleration of the cyclotron motion:

$$\frac{d^2\vec{r}}{dt^2} = \frac{\vec{F}}{m} = \frac{q}{m}\frac{d\vec{r}}{dt} \times \vec{B}. \tag{2.13}$$

The magnetic field of a Penning trap is $\vec{B} = B_0\hat{z}$ and cyclotron motion is in the ϕ direction: $\frac{d\vec{r}}{dt} = v_\phi\hat{\phi}$. Therefore,

$$|\frac{d^2\vec{r}}{dt^2}|^2 = \left(\frac{qB_0}{m}\right)^2 v_\phi^2, \tag{2.14}$$

and the power radiated by the cyclotron motion is

$$\frac{dE_c}{dt} = -\frac{E_c}{\tau_s}, \tag{2.15}$$

where E_c is the cyclotron energy and τ_s is the synchrotron damping time:

$$\tau_s = \frac{3\pi\epsilon_0 m^3 c^3}{q^4 B_0^2}. \tag{2.16}$$

The solution to equation (2.15) is an exponential decay of energy $E_c(t) = E_0 e^{-t/\tau_s}$. The m^3 dependency is very important when using particles of different mass in the same Penning trap. Electrons and e^+ have time constants 6×10^9 times smaller than those of p or $\bar{p}$ ($\tau_s = 500$ years for p or $\bar{p}$ in a 1 T magnetic field, while an e^- or e^+ in the same field has a damping time of $\tau_s = 2.6$ s). The B_0^{-2} dependency indicates that the cooling time of charged particles in a Penning trap is reduced if the B_0 is increased.

2.1.4 Ioffe Traps

The electrostatic and magnetic fields of a Penning trap confine charged particles, but do not confine neutral atoms such as $\overline{\mathrm{H}}$. Neutral atoms can be confined through interactions with their magnetic moment. The energy of an atom with a magnetic moment $\vec{\mu}$ is shifted in the presence of a magnetic field by $\Delta E = -\vec{\mu} \cdot \vec{B}$. In free space, a magnetic field can have a local minimum but no local maximum [39]. Atoms with magnetic moments anti-aligned with the direction of the magnetic field will have lower energies at a magnetic-field minimum and could potentially be trapped. Atoms with magnetic moments aligned with the magnetic field have lower energy in larger magnetic fields and cannot be trapped.

Several variations of magnetic gradient traps could be used to implement a magnetic-field minimum [40]. The trap of choice for $\overline{\mathrm{H}}$ trapping collaborations is the Ioffe trap. The magnetic gradient of the Ioffe trap is produced using a set of electromagnets: race-track coils that produce a radial magnetic field gradient and two short solenoid coils that produce the axial magnetic field gradient (Figure 2.3(a)). The combined magnetic field of this Ioffe trap and the uniform magnetic field $B_0\hat{z}$ of the Penning trap prevents the minimum of the magnetic field gradient from reaching zero, and this prevents Majorana spin-flip transitions [41], which flip the magnetic moment and cause $\overline{\mathrm{H}}$ loss. The race-track coils, shown in Figure 2.3(a), produce a quadrupole field but an octupole field would also produce a suitable field minimum.

The cylindrical symmetry that provides the confinement theorem (2.11) for particles in a Penning trap is broken in a combined Penning-Ioffe trap. Charged particles continue to perform cyclotron motion around magnetic field lines as they do in a Penning trap but the field lines are no longer purely in the z direction, with many field lines intersecting the electrode stack walls, as shown in Figure 2.3(b).

Despite the complicated $\vec{B}$ field, charged particles can be confined in a Penning-Ioffe trap provided that the particles remain in a volume near the center of the trap [42]. In the ATRAP cryogenic Penning-Ioffe trap, for example, charged particles will remain confined in a three-electrode-long potential well as long as they are less than approximately 4 mm from the radial-center of the electrode stack.

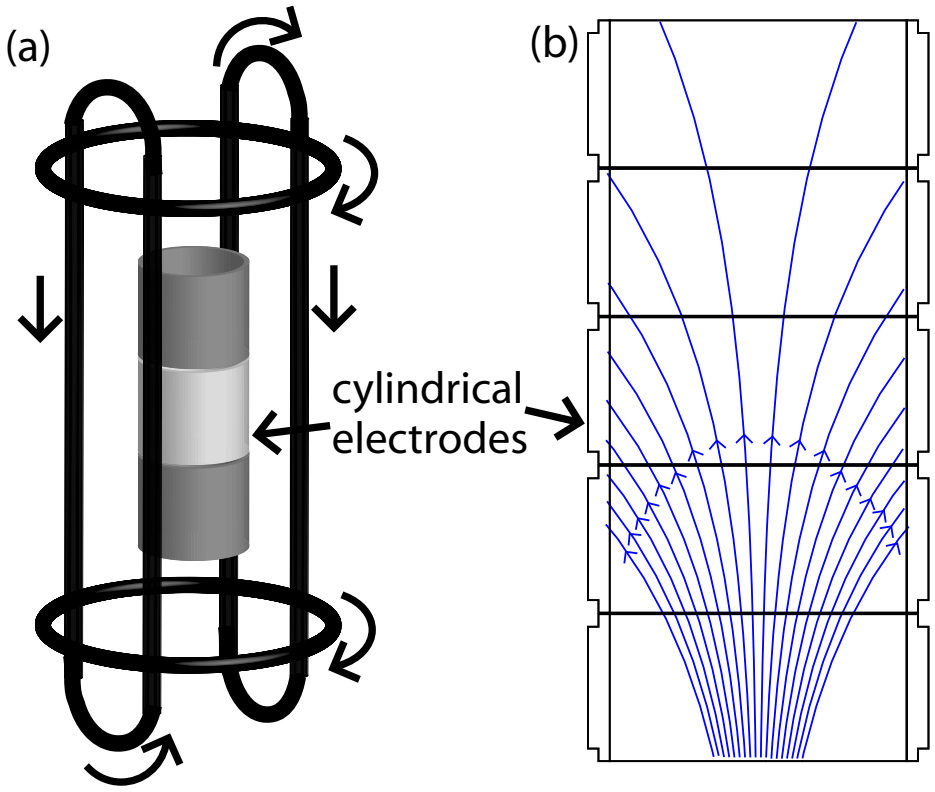

FIGURE 2.3: A schematic representation of electromagnets used to create a Ioffe trap over an electrode stack (a). The combined magnetic field of the Ioffe trap and the uniform magnetic field of the Penning trap (b). The field lines in (b) show the non-uniformity caused by the Ioffe coils for field lines in one plane.

The energy shifts $\Delta E = -\vec{\mu}\cdot\vec{B}$ are very small. As such, Ioffe traps are very shallow, with typical depths (in temperature units $T = E/k_B$) of $T = \mu\Delta B/k_B < 1$ K, where ΔB is the difference of the magnetic field at the center of the Ioffe trap compared to that at the Penning-trap electrodes. The temperature of $\overline{\mathrm{H}}$ is at least as large as the temperature of the $\bar{\mathrm{p}}$ that are used to make them. Antiprotons have been adiabatically cooled to 3.5 K by ATRAP [26] and evaporatively cooled to 9 K by ALPHA [43]. Even if $\overline{\mathrm{H}}$ could be created with these temperatures, most of the

$\overline{\mathrm{H}}$ created would have enough kinetic energy to overcome the Ioffe trap magnetic potential well and be lost on the electrode stack walls. Only the slow tail of the distribution could be confined within the magnetic-field gradient of the Ioffe trap.

2.2 Plasmas in a Penning Trap

ATRAP $\overline{\mathrm{H}}$ production trials typically use between 1×10^6 and 5×10^6 $\bar{\mathrm{p}}$ and between 3×10^7 and 3×10^8 e^+. Large ensembles of charged particles begin to exhibit collective effects, at which point one can refer to the ensemble as a non-neutral plasma. An ensemble of particles can be considered to be a plasma if the Debye length $\lambda_D = \sqrt{\epsilon_0 k_B T/nq^2}$ is small compared to the spatial extent of the plasma itself. In the ATRAP cryogenic Penning trap, our plasmas are typically between a few mm and a few cm in both diameter and length, leading to plasma densities on the order of $n = 10^6 - 10^8$ cm^{-3}, for which the Debye length is $\approx 10 - 100$ μm — much smaller than the plasma itself. The charged particles in a plasma evolve to a state of thermal equilibrium, with a particle density that is constant in the plasma interior and drops to zero at the edge of the plasma over the Debye length. The density for a spheroidal plasma is given by

$$n = \frac{N}{\frac{4}{3}\pi r_p^2 z_p}, \tag{2.17}$$

where N is the number of particles in the plasma, r_p is the plasma radius, and z_p is the plasma axial radius or half-length. The plasma aspect ratio α_p is the ratio of plasma half-length to radius: $\alpha_p = z_p/r_p$.

2.2.1 Plasma Confinement

Plasma confinement is very similar to single-particle confinement — the electric field provides axial confinement while the magnetic field provides radial confinement (Figure 2.4). The electric field is now due to a combination of two effects: the electric field due to the applied trap potential and the electric field due to the charged plasma. The plasma oscillates in the z direction as a harmonic oscillator with frequency ω_z. The outward-pointing radial electric field and the axial magnetic field produce an $\vec{E} \times \vec{B}$ drift motion analogous to the magnetron motion of a single particle in a Penning trap. The Lorentz force due to this motion in the magnetic field provides an inward radial force that opposes the electrostatic force on the plasma and radially confines the plasma. The result is that the entire plasma rotates in the Penning trap at a single frequency ω_r.

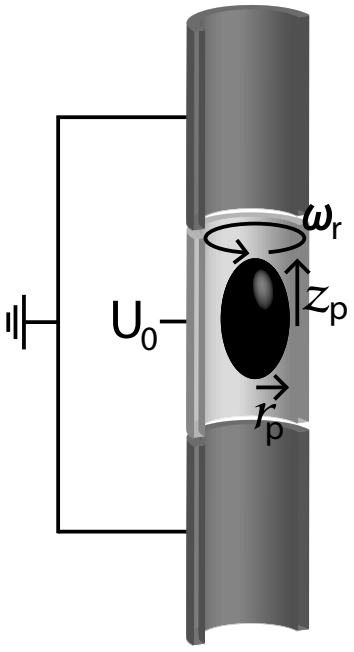

FIGURE 2.4: An example of a non-neutral plasma confined in a cylindrical Penning trap electrode stack.

The theory of plasma confinement in a Penning trap is explored in detail by Dubin and O'Neil [44]. They use thermal equilibrium statistical mechanics to

provide a description which is very useful in that the thermal equilibrium states are determined by constants of motion, making the final plasma state predictable from its initial state, regardless of whatever complicated evolution occurs between those states. An important result of this description is the characterization of the thermal equilibrium states using a Boltzmann distribution. For a plasma where correlations between the particles are weak, the density $n(r,z)$ is given by

$$n(r,z) = n_0 \exp\left(-\frac{q\phi(r,z) + \frac{1}{2}m\omega_r(\omega_c - \omega_r)r^2}{k_B T}\right), \tag{2.18}$$

where $\phi(r,z)$ is the sum of the trap potential and the electrostatic potential due to the charge of the plasma at zero temperature. The density must remain finite, and therefore $q\phi(r,z) + \frac{1}{2}m\omega_r(\omega_c - \omega_r)r^2 = 0$, and the density is constant with value n_0. Substituting equation (2.18) into Poisson's equation $\nabla^2\phi(r,z) = (q/\epsilon_0)n(r,z)$, yields n_0:

$$n_0 = \frac{2\epsilon_0 m\omega_r(\omega_c - \omega_r)}{q^2} \simeq \frac{2\epsilon_0 m\omega_r\omega_c}{q^2}, \tag{2.19}$$

where $\omega_c \gg \omega_r$ provides the approximation. This equation shows a linear relation between the plasma density and plasma rotation frequency, indicating that the plasma density can be increased by applying a torque to increase the plasma rotation frequency.

The motion of the individual charged particles that make up the plasma are governed by the Hamiltonian:

$$H = \sum_{j=1}^{N}\left(\frac{p_{r_j}^2}{2m} + \frac{(p_{\theta_j} - \frac{e}{c}A_\theta(r_j)r_j)^2}{2mr_j^2} + \frac{p_{z_j}^2}{2m}\right) + \sum_{j=1}^{N} e\phi_T(\vec{r}_j) + \frac{1}{2}\sum_{i,j=1}^{N} e^2 G(\vec{r}_i|\vec{r}_j). \tag{2.20}$$

The first sum is the kinetic energy, the second is the electrostatic energy of the charged particles in the trap potential, and the third is the electrostatic interaction energy of the charged particles in the plasma with each other ($G(\vec{r}_i|\vec{r}_j)$ is the Green's function). The Hamiltonian assumes that the plasma is far from the electrode stack walls, so that image charges due to the conducting surfaces of the electrodes are negligible. The Hamiltonian uses the canonical momenta:

$$p_{r_j} = m\frac{\mathrm{d}r_j}{\mathrm{d}t}, \quad p_{\theta_j} = mr_j^2\frac{\mathrm{d}\theta_j}{\mathrm{d}t} + \frac{e}{c}A_\theta(r_j)r_j, \quad \text{and} \quad p_z = m\frac{\mathrm{d}z_j}{\mathrm{d}t}. \tag{2.21}$$

There are two important symmetries to note: First, that the Hamiltonian has no time dependence, and so the Hamiltonian is a constant of motion itself: $H = E$, the total particle energy. Second, due to the cylindrical symmetry of the Penning trap, the Hamiltonian is invariant under translations in θ. Therefore, the total canonical angular momentum $P_\theta = \sum p_{\theta_j} = L$ is conserved. The canonical angular momentum can be written as

$$L = \sum_{j=1}^{N} mv_\theta r_j + \frac{eBr_j^2}{2c} \simeq \sum_{j=1}^{N} \frac{eBr_j^2}{2c}, \tag{2.22}$$

where the approximation comes from neglecting the mechanical part of the angular momentum, which is possible when the second term is much larger due to a large magnetic field. Since L is conserved, the mean square radius ($\sum_{j=1}^{N} r_j^2$) is also conserved in this apparatus, thereby keeping the plasma constrained. This confinement theorem breaks down when any torque — such as would result from a misalignment of the magnetic field and electrode stack — is applied to the plasma. In practice, such apparatus imperfections can be minimized, and plasmas can be held in a well-built Penning trap for days.

2.2.2 Internal Plasma Dynamics

A plasma of N particles has $N-1$ modes of oscillation. These modes are labelled using the integers ℓ and m, with $\ell > 0$ and $|m| < \ell$. All modes with $m \neq 0$ are suppressed in a cylindrically symmetric apparatus, and the frequencies of the $m = 0$ modes are simply labelled ω_ℓ. The axial harmonic oscillation of the plasma with frequency $\omega_\ell = \omega_1$ is the center-of-mass mode, also denoted as ω_z. The next-lowest-order mode, ω_2, is the oscillation of the aspect ratio α_p of the plasma — also called the quadrupole or breathing mode. These modes can be measured [45] and analytic solutions [46] in the limit of $T \to 0$ for the Penning trap potentials give

$$1 - \frac{\omega_p^2}{\omega_\ell^2} = \frac{k_2}{k_1} \frac{P_\ell(k_1) Q'_\ell(k_2)}{P'_\ell(k_1) Q_\ell(k_2)}, \tag{2.23}$$

where the plasma frequency ω_p is defined as

$$\omega_p^2 = 4\pi e^2 n_0 / m, \tag{2.24}$$

and P_ℓ and Q_ℓ are the Legendre functions of the first and second kinds, and P'_ℓ and Q'_ℓ are their derivatives. k_1 and k_2 are

$$k_1 = \frac{\alpha_p}{\sqrt{\alpha_p^2 - 1 + \omega_p^2/\omega_\ell^2}}, \qquad k_2 = \frac{\alpha_p}{\sqrt{\alpha_p^2 - 1}}, \tag{2.25}$$

and, thus, Equation (2.23) provides ω_ℓ in terms of the aspect ratio α_p and the plasma frequency ω_p in the limit of $T \to 0$. The ω_2 mode is calculated (using Equation (2.23)) and shown in Figure 2.5 normalized to $\omega_1 \equiv \omega_z$.

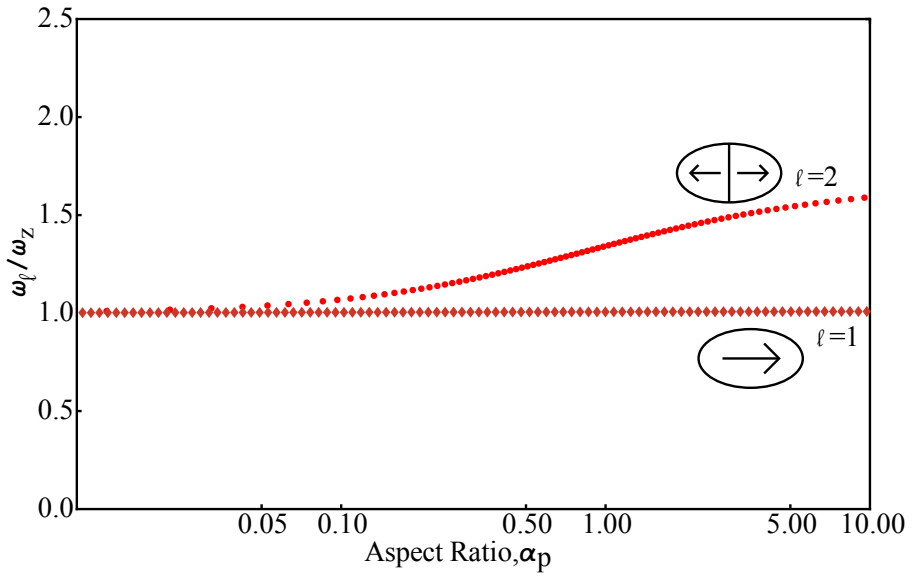

FIGURE 2.5: The ω_2 oscillation frequency of a nonneutral plasma as a function of the plasma aspect ratio α_p, normalized to $\omega_1 \equiv \omega_z$.

An approximate solution exists for ω_2 at finite temperature [47]. These approximate solutions predict a temperature-dependent shift in the quadrupole mode frequency

$$(\omega_2)^2 = (\omega_2^0)^2 + 5\left(3 - \frac{\alpha_p^2}{2}\frac{\omega_p^2}{(\omega_2^0)^2}\frac{\partial^2 A_3}{\partial \alpha_p^2}\right)\frac{k_b T}{m z_p^2}, \tag{2.26}$$

where $A_3 = 2Q_1(k_2)/(\alpha_p^2 - 1)$ and ω_2^0 is the quadrupole frequency at $T = 0$. Changes in plasma temperature can be detected by monitoring changes in ω_2. This principle is used in Section 4.6 in an attempt to measure the temperature of e^+ plasmas in the ATRAP cryogenic Penning trap. If one could measure a higher-order mode with a different temperature dependence than the lower-order modes [48], then an absolute measurement of the plasma temperature would be possible. Attempts to measure an ω_3 mode are also discussed in Section 4.6.

2.2.3 Plasma Simulation

Plasmas in a cylindrical Penning trap can be simulated numerically using a particle-in-cell code called EQUILSOR [49]. The code solves Poisson's equation self-consistently with the Boltzmann equation for the density distribution of the plasma in the trap field. The code takes the Penning-trap parameters, such as electrode lengths, radii and applied voltages and magnetic field strength, and initial values for the plasma dimensions, such as length, radius, plasma density, and particle type. EQUILSOR starts by solving Poisson's equation for the applied potential of the Penning trap, and then the full field, including the contribution from the plasma charge, is included. An iterative process solves for a self-consistent equilibrium potential and density distribution: the density distribution of the plasma is modified to be consistent with the full potential (trap plus plasma charge) and then the potential is solved for including the newly modified density distribution of the plasma. The iterative process continues until a preselected tolerance is met. EQUILSOR is used to simulate plasmas used in e^- cooling of e^+ (Section 7.4.2).

Chapter 3

ATRAP Apparatus

A simple depiction of the ATRAP $\overline{\mathrm{H}}$ apparatus is shown in Figure 3.1, with a more detailed schematic shown in Figure 3.2. Positrons from a ^{22}Na source (discussed in Section 5.2) are slowed in a cryogenic Ne moderator (discussed in Section 5.3) and accumulated in a room-temperature Penning trap (discussed in Section 5.5). Positrons from the positron accumulator are transfered to the cryogenic Penning trap using the e^+ transfer guide, which is discussed in Chapter 6.

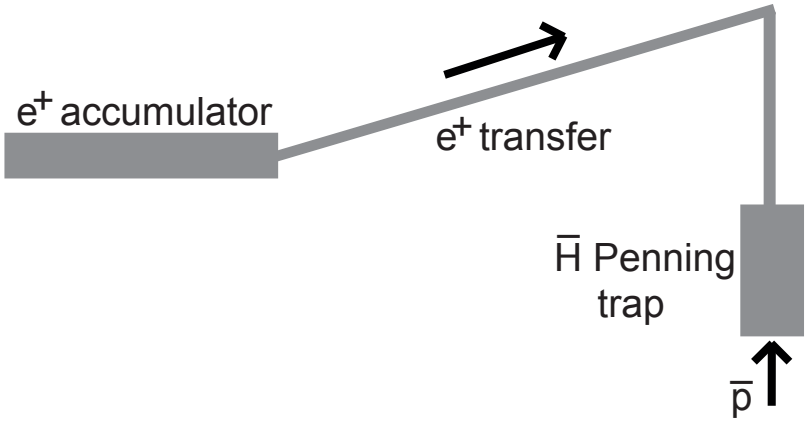

FIGURE 3.1: A simple depiction of the ATRAP $\overline{\mathrm{H}}$ apparatus. Positrons are accumulated and transfered to the cryogenic Penning trap for $\overline{\mathrm{H}}$. Antiprotons enter the cryogenic Penning trap from the AD beamline below the trap.

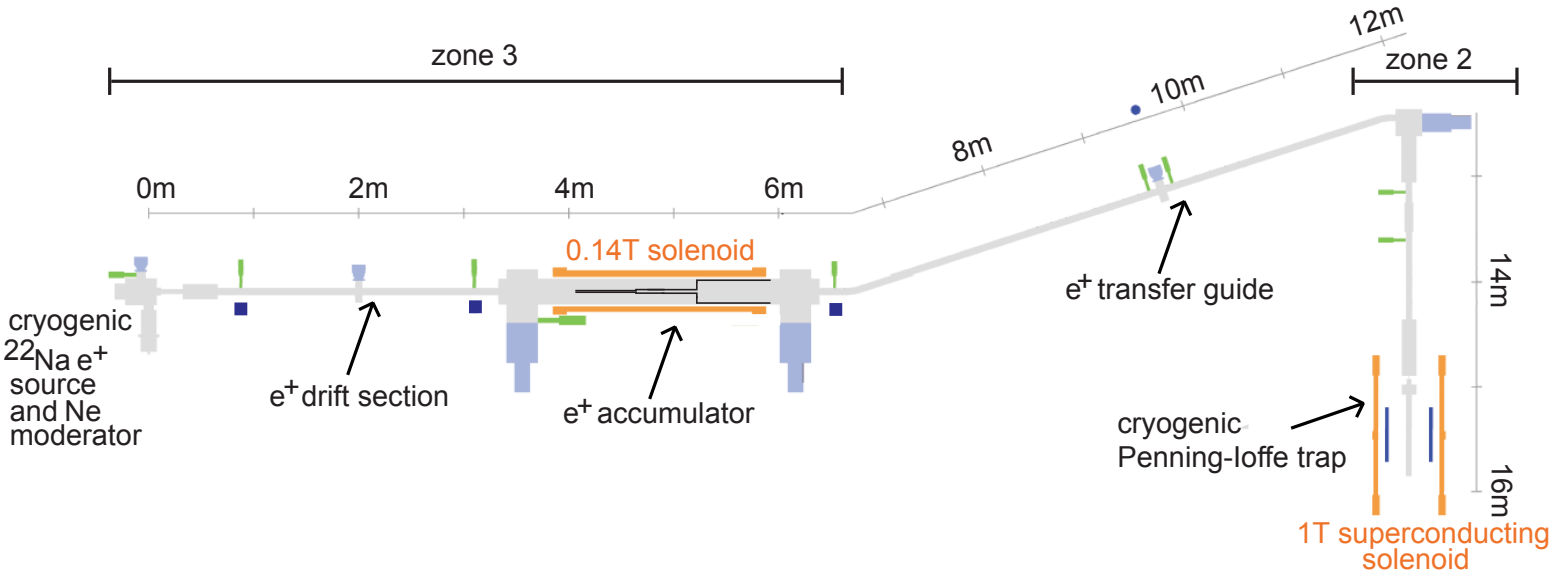

FIGURE 3.2: The entire ATRAP $\bar{H}$ apparatus.

The part of this ATRAP apparatus which is located in zone 2 of Figure 1.2 is shown in Figure 3.3. The cryogenic Penning-trap electrode stack, superconducting magnets, liquid-helium system, XY translatable stage and detector system, shown in this figure, are discussed in the following sections.

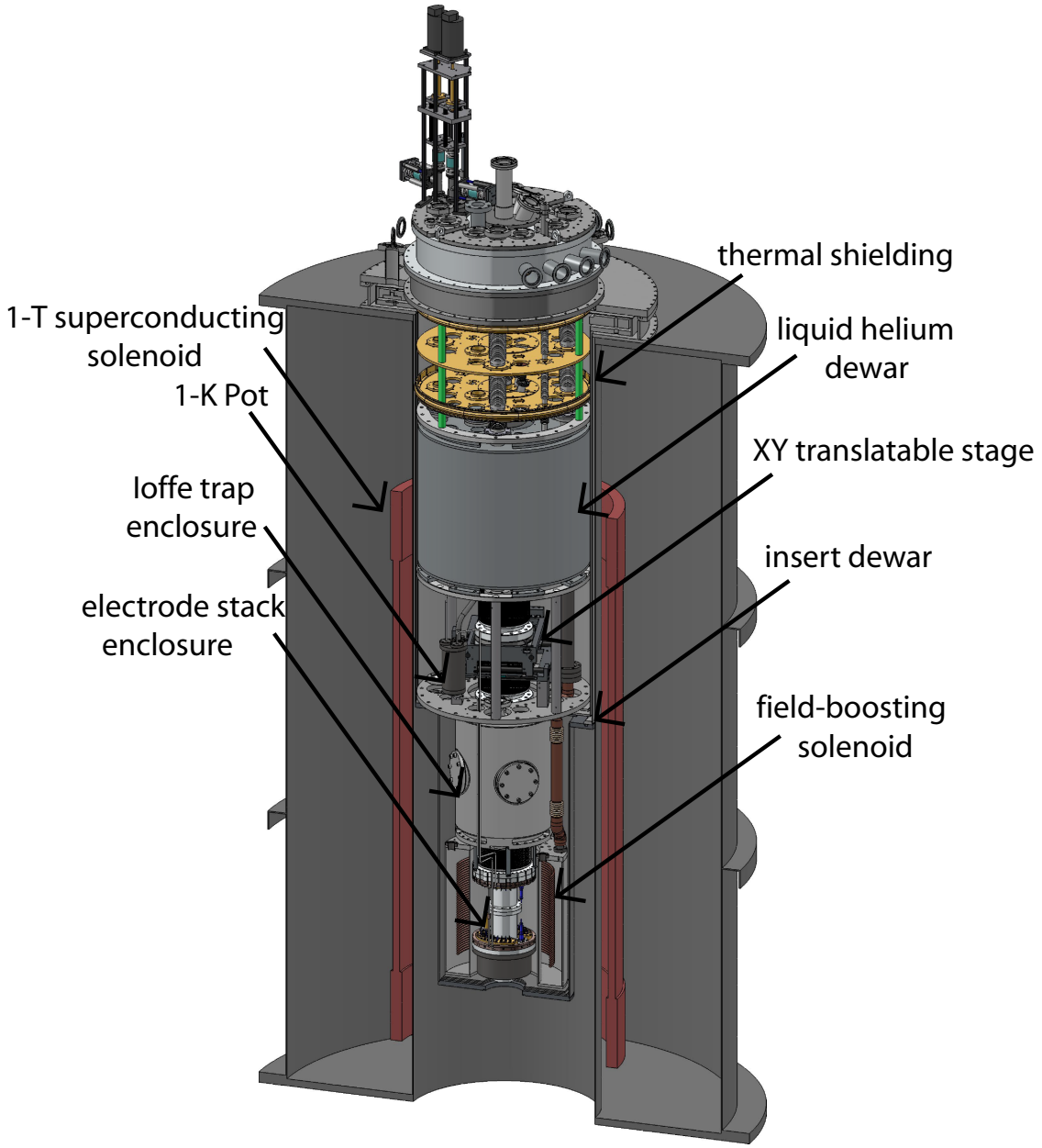

FIGURE 3.3: The ATRAP $\bar{\mathrm{H}}$ apparatus located in Zone 2.

3.1 Cryogenic Penning-Ioffe Trap

3.1.1 ATRAP Electrode Stack

The ATRAP cryogenic Penning-trap electrode stack is shown in Figure 3.4. Thirty-nine gold-plated copper, hollow, cylindrical electrodes are separated by macor spacers that provide electrical isolation to allow each electrode to be individually biased. The electrode stack is separated into two regions: the lower stack, which is used for $\bar{p}$ and e^- loading and the upper stack, where e^+ are loaded and $\overline{H}$ experiments are performed. All electrodes have an inner diameter of 36 mm. Most electrodes in the lower stack are diameter-length electrodes (i.e, a 36-mm height) while most upper-stack electrodes are radius-length (i.e., an 18-mm height).

Each electrode has a DC and AC line connection. DC lines are used to apply constant or slowly-varying voltages. Each DC line has RC and LC filters with 200 ms and 20 μs time constants, respectively, to block rf noise. AC lines (capacitively-coupled micro-coax or twisted pair lines) are used in the application of pulses and rf drives.

3.1.1.1 Lower Stack

Antiprotons enter the electrode stack through the bottom of the lower stack through a beryllium degrader (DEG in Figure 3.4). A voltage of -5 kV is applied to the HV electrode (Figure 3.4) and to the degrader, to create a deep electrostatic potential well for catching incoming $\bar{p}$, as outlined in Section 7.3. Electrode LTRW is segmented into quadrants for application of a rotating electric field, as described in Section 5.5.3.

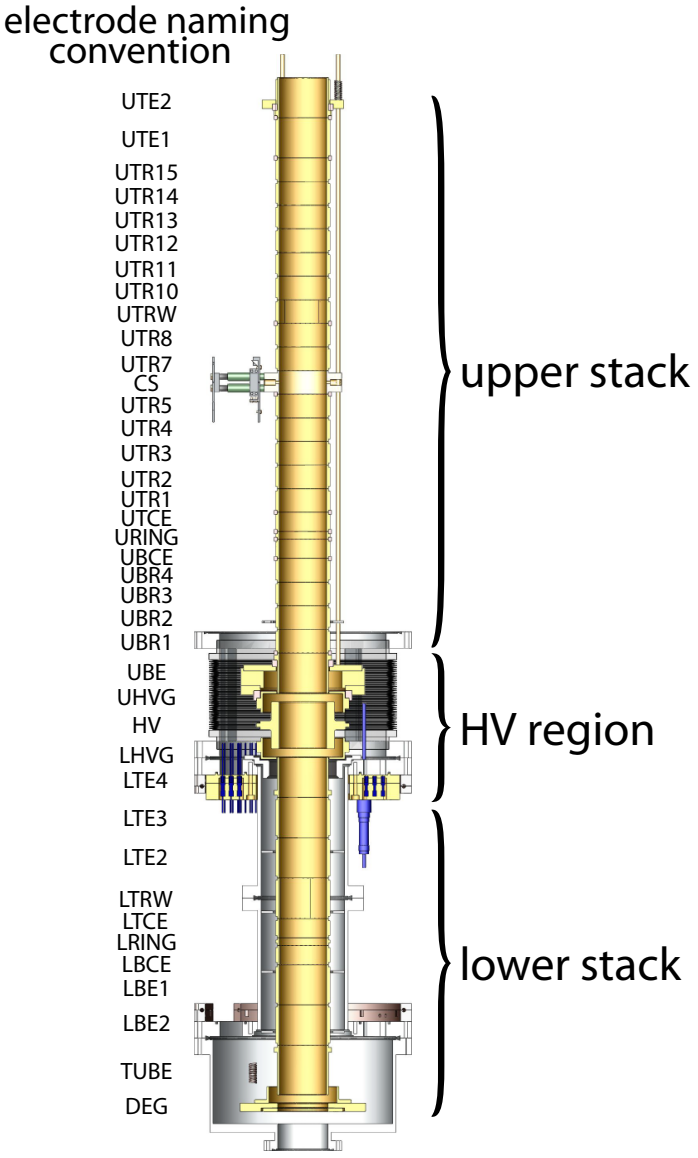

FIGURE 3.4: The ATRAP cryogenic Penning-trap electrode stack, along with the naming convention used for each electrode.

3.1.1.2 Upper Stack

The upper-stack electrodes are nearly all radius length, allowing for the creation of the more complicated nested-well structures necessary for holding e^+ and $\bar{p}$ as closely as possible to one another. Part of the upper stack lies within the magnetic field of the Ioffe trap, and any experiment which produces or studies trapped $\overline{H}$ are performed in this region. The CS electrode (Figure 3.4) has two holes (0.8 mm and 2.5 mm in diameter) on opposite sides of the electrode that allow for

Cs atoms to enter and exit the electrode stack in charge-exchange $\overline{\mathrm{H}}$ production experiments, as discussed in Section 8.2.

3.1.2 ATRAP Superconducting Magnets

The magnetic fields of the Penning-Ioffe trap are generated by the 4.2-K superconducting electromagnets shown in Figure 3.3. The superconducting solenoid generates the 1-T magnetic field of the cryogenic Penning trap. A superconducting solenoid at the bottom of the electrode stack acts as a field-boosting solenoid for $\bar{\mathrm{p}}$ loading (See Figure 3.5). The solenoid is energized with 55 A and boosts the 1-T field up to 3.7 T. This increased field has several beneficial effects for $\bar{\mathrm{p}}$ loading, as discussed in Section 7.3.

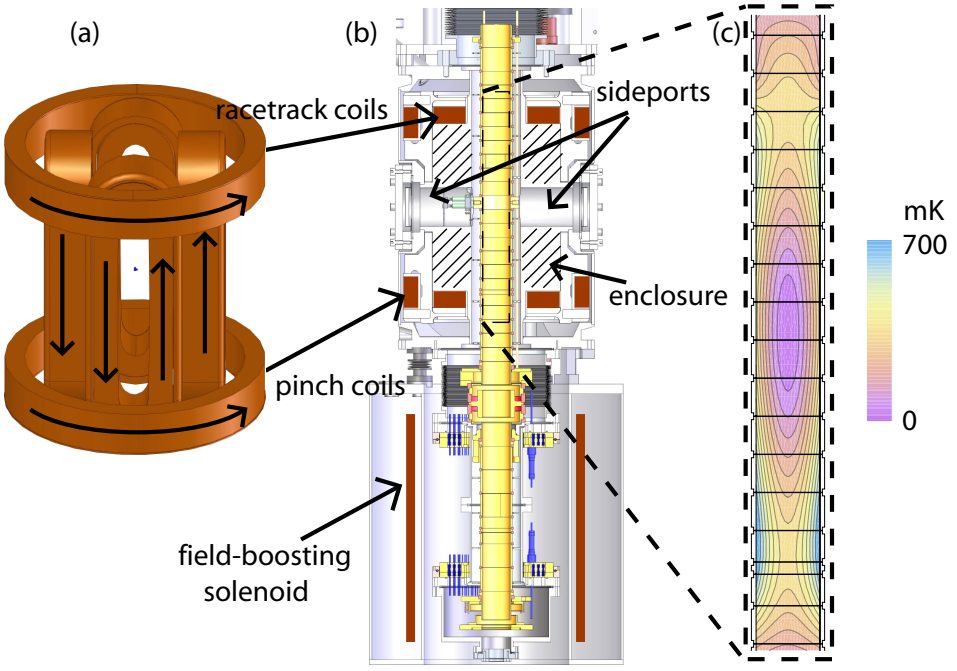

FIGURE 3.5: The ATRAP superconducting Ioffe Trap. The coil geometry and the direction of current when the field is energized (a). The Ioffe-trap enclosure and Penning-trap electrode stack (b). A contour plot (in steps of 0.075 T) showing the depth of the magnetic gradient trap (in units of temperature) produced by energizing the Ioffe trap coils (c).

As shown in Figure 3.5(a), the Ioffe trap consists of six superconducting coils: two hoop coils (called the pinch coils) and four racetrack coils that produce a

quadrupole field in between them. The pinch coils and racetrack coils are energized with 80 A and 69 A, respectively, to create the magnetic field magnitudes shown in Figure 3.5(c). From this figure, one can see a magnetic field difference of 0.54 T between the magnetic field minimum at center of the electrode stack and the magnetic field at the electrode stack walls.

The Ioffe-trap enclosure (Figure 3.5(b)) is made entirely of non-magnetic components to avoid deviations from desired magnetic fields. The enclosure is built with four elliptical side ports that allow access to the center of the electrode stack. The Cs apparatus used for charge-exchange $\overline{\mathrm{H}}$ production is mounted to one of the the sideports, as described in Section 8.2.1. The sideport flanges are custom-machined to include UV and IR windows for possible optical access, and with electrical feedthrus to allow for biasing and power connections.

3.1.3 Cooling for Penning-Trap Electrodes

Several layers of thermal protection are used to ensure that the cryogenic system is maintained at 4.2 K, and to reduce the rate of the liquid-helium boil-off. Three copper plates, each layered with aluminized mylar superinsulation act as the first thermal shielding at the top of the apparatus in Figure 3.3. The insert dewar in Figure 3.3 is cooled to 20 K using a helium compression refrigerator (Cryomech CP970) and three stages of pulse-tube cryocoolers (Cryomech PT405 and PT60), thereby eliminating the heat load due to radiation from the 300-K magnet bore. The insert dewar space is constantly pumped on using a turbo pump (BOC Edwards EXT 255H) to maintain thermal isolation between the trap and the insert dewar. Liquid helium fills the volume of the field-boosting solenoid enclosure, the Ioffe-trap enclosure, and the 40-L liquid-helium dewar.

The pumped helium system [50], called the 1-K Pot, shown in Figure 3.6, is used to maintain the cryogenic Penning-trap electrode stack at 1.2 K. A needle valve

controls the flow of helium into the 1-K pot. A small tube of capillaries from the helium space fills a small reservoir where a vacuum pump (BOC Edwards GVSP30) removes helium vapour to evapouratively cool the helium in the reservoir to 1.2-K superfluid liquid helium. The superfluid helium fills up the reservoir and copper tubes carry the 1.2-K liquid helium to the electrode-stack enclosure.

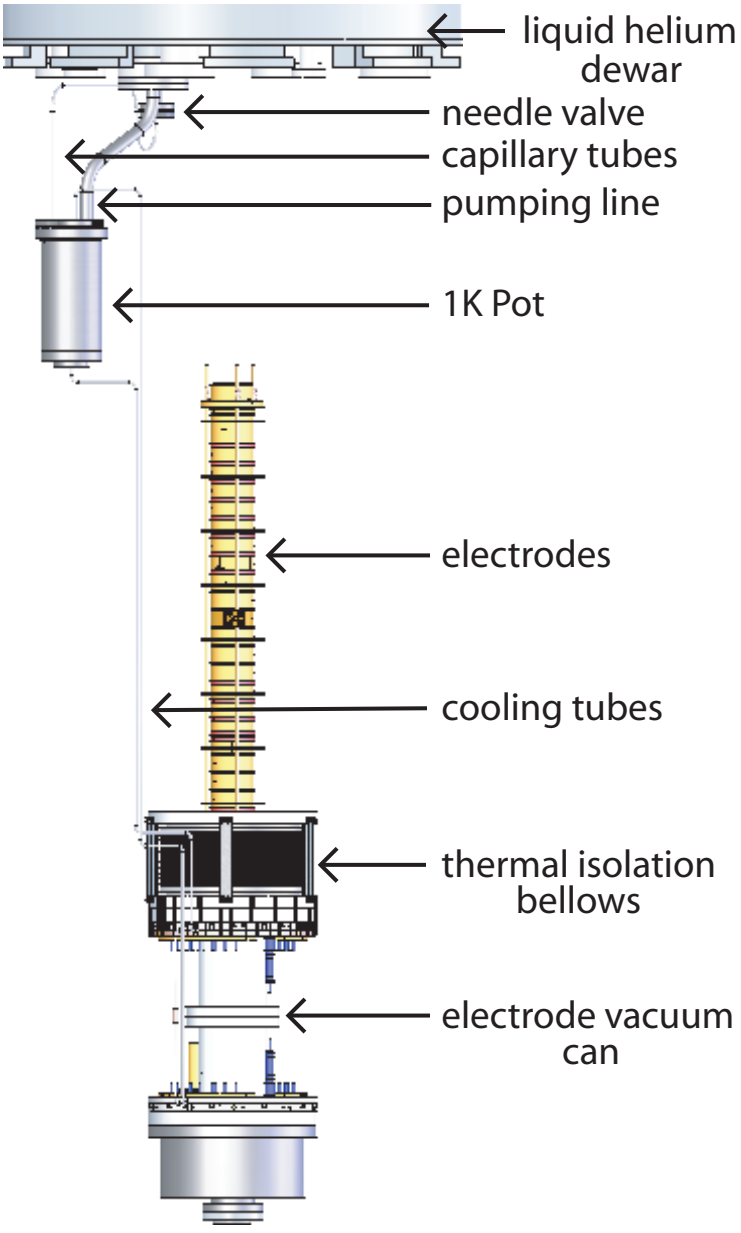

FIGURE 3.6: The pumped helium system (called the 1-K Pot) cools the Penning-trap electrode stack to 1.2 K.

3.1.4 XY Translatable Stage

As shown in Figure 3.3, below the thermal shielding is the first part of the ATRAP apparatus at cryogenic temperatures: the XY translatable stage (See Figure 3.7). The XY translatable stage is a two-axis translatable stage with various windows and holes that can be moved into alignment with the axis of the cryogenic Penning-trap electrode stack. The XY translatable stage is normally positioned with the 4-K, 1.5-mm-diameter, 20-mm-long pumping restriction for e^+ access centered on the electrode stack. This pumping restriction separates the $< 6 \times 10^{-17}$ torr, 1.2-K experiment space from the poorer vacuum above it, while still providing access for e^+ to enter the cryogenic Penning trap. The XY translatable stage is also equipped with a phosphor screen (the intent of which is to image the radial extent of $\bar{p}$, e^+ , or e^- plasmas) and a MgF_2 window to allow for laser beams to access the Penning-Ioffe trap for possible $\overline{H}$ spectroscopy and laser cooling.

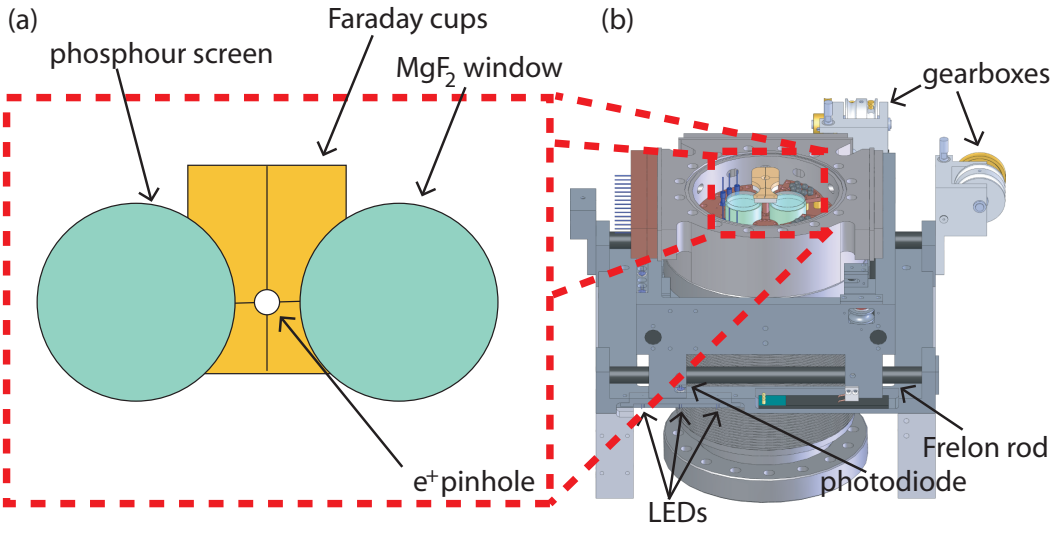

FIGURE 3.7: The translatable XY stage.

The XY translatable stage can be moved along each of two axes using two gearbox and pulley systems. Motion in each axis is controlled with fiberglass driveshafts that extend from outside the vacuum space down to gearboxes connected to copper cables mounted onto the stage. The stage slides along low-friction Frelon rods

while the stage position is monitored by resistance measurements of a potentiometer and by LED-photodiode pairs.

3.1.5 ATRAP Detector System

Antiproton and e^+ annihilations are detected using four layers of scintillating fibers and two layers of scintillating paddles, as shown in Figure 3.8 [51].

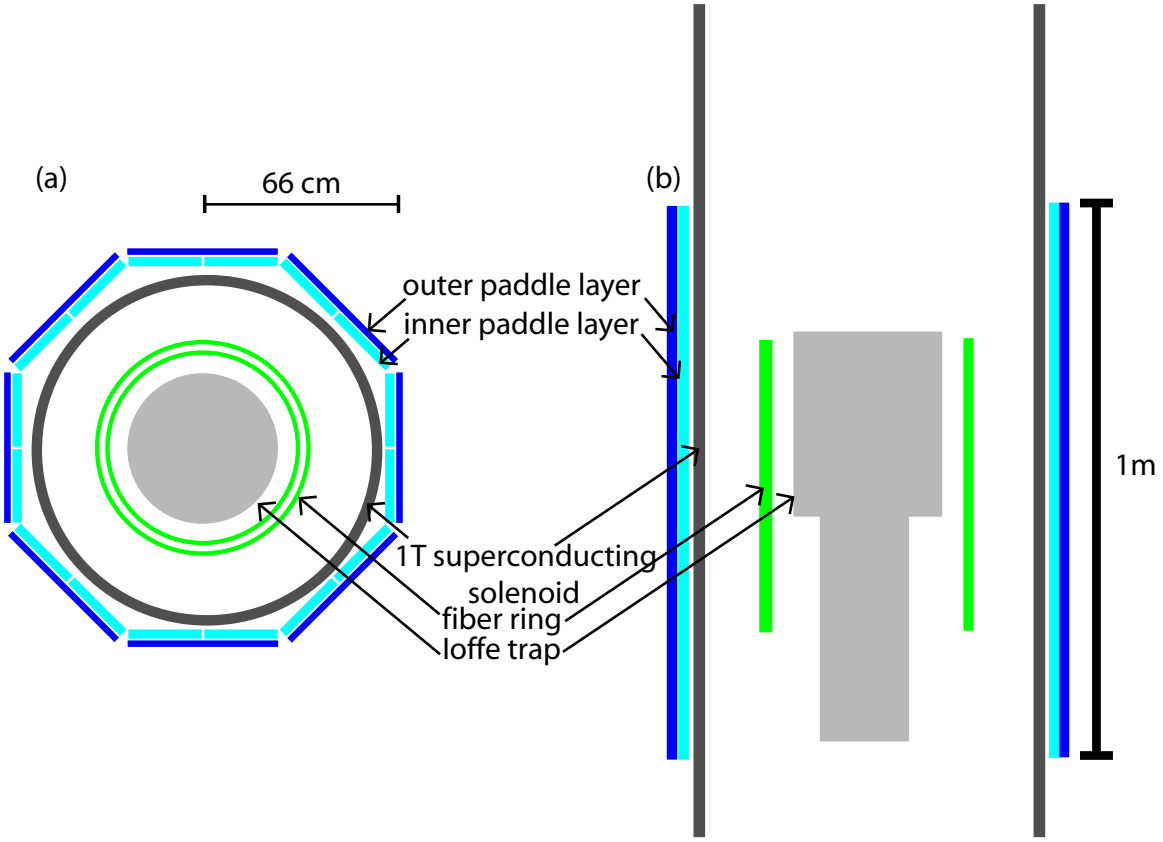

FIGURE 3.8: A top-down view (a) and cross-sectional side view (b) of the scintillating detectors that surround the cryogenic Penning trap.

The four layers of 3.8-mm-diameter BICRON BCF-12 fibers surround the Ioffe trap on a 39-cm radius. Two cylindrical layers of fibers are constructed from 448 straight, vertical fibers. The other two fiber layers (336 fibers in total) are wound helically around the cylinders of straight layers. The windings are overlapping such that all high-energy particles that pass through the cylinder will hit at least one straight fiber and one helical fiber.

The BICRON BC404 scintillating paddle detectors are outside the 1-T superconducting solenoid — 66 cm from the center of the cryogenic Penning-trap electrode stack. The first layer is made of sixteen 13.3-mm-thick paddles paired in the octagonal configuration of Figure 3.8(a). 7 mm behind these paddles is the second layer of eight 6.6-mm-thick paddles that are twice as wide as those in the first layer. Any high-energy particle that passes through the first layer of paddles is nearly guaranteed to pass through the second layer, allowing the paddles to act as coincidence detectors with a 40-ns time window, greatly reducing background signals from electronic noise.

Data is constantly acquired from each fiber and paddle. Paddle events are logged with a time stamp, paddle identifier, and amplitude, while fiber data are logged with a time stamp and fiber identifier. The processing of these signals for $\bar{p}$ and e^+ counting is discussed in Chapter 4.

Chapter 4

Plasma Measurements and Particle Counting

Accurate particle detection techniques are necessary to count and parameterize the large numbers of e^-, e^+, and $\bar{p}$ used in $\overline{H}$ production trials, and to detect the often small numbers of these particles that act as indications of Rydberg positronium and $\overline{H}$ production.

4.1 Non-destructive Plasma Measurements

The excitation and detection of plasma modes provides a non-destructive method of studying plasmas. Section 2.2 gives a discussion of plasma modes. Studies of these plasma modes have been performed by others using non-neutral plasmas of room-temperature ions [52], room temperature e^- and e^+ [53], and e^- and e^+ plasmas contained in cryogenic Penning traps [54][55]. Reference [53] is especially extensive, discussing the frequency dependence of plasma modes on plasma aspect ratio, temperature, and number of particles in the plasma. For the experiments performed by ATRAP, we are mostly concerned with the axial and radial extent

of our plasmas, and in measuring temperature changes in our plasmas. These parameters can be determined from measurements of the center-of-mass (ω_z) and quadrupole (ω_2) plasma frequencies, as discussed in Section 2.2.2.

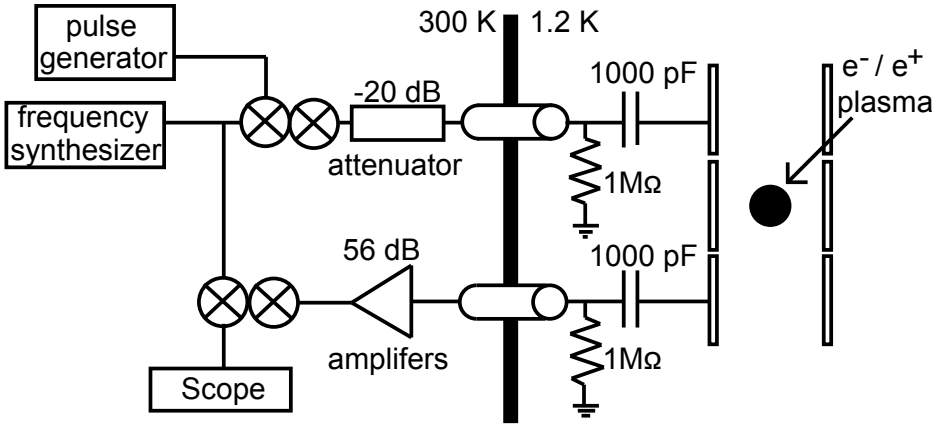

FIGURE 4.1: The apparatus used to measure longitudinal modes in lepton plasmas.

The ω_z and ω_2 modes are excited and measured using a pulsed-drive ring-down-detection measurement technique [29]. The instrumentation is shown in Figure 4.1. The output from a frequency synthesizer (PTS250) is gated using a pair of rf switches (ZYSWA-2-50DR). A pair of switches is used as opposed to a single switch to decrease the turn-on and turn-off time of the pulse. The 1-μs pulse that exits the rf switches is attenuated before entering the trap area to ensure that this excitation pulse is not strong enough to influence the frequency of oscillation of the plasma. The excitation pulse is applied to the electrode directly above the one holding the plasma. The excitation of the plasma motion induces current oscillations on the electrode directly below it. The current oscillations produce voltage oscillations when passing through the 1-MΩ resistor of the electrode filter (shown in Figure 4.1). These voltage oscillations are amplified by room-temperature amplifiers (two Anzac AM-107 and one MITEQ Bipolar amplifier) and mixed with the output of the frequency synthesizer. That heterodyned signal is then measured using an oscilloscope after a 3-μs delay which ensures that the driving frequency will not be picked up. A fast Fourier transform of the scope trace gives the signal

vs frequency, as in Figure 4.2(a) and (b). The driven plasma oscillation mode shows up as a peak in these plots.

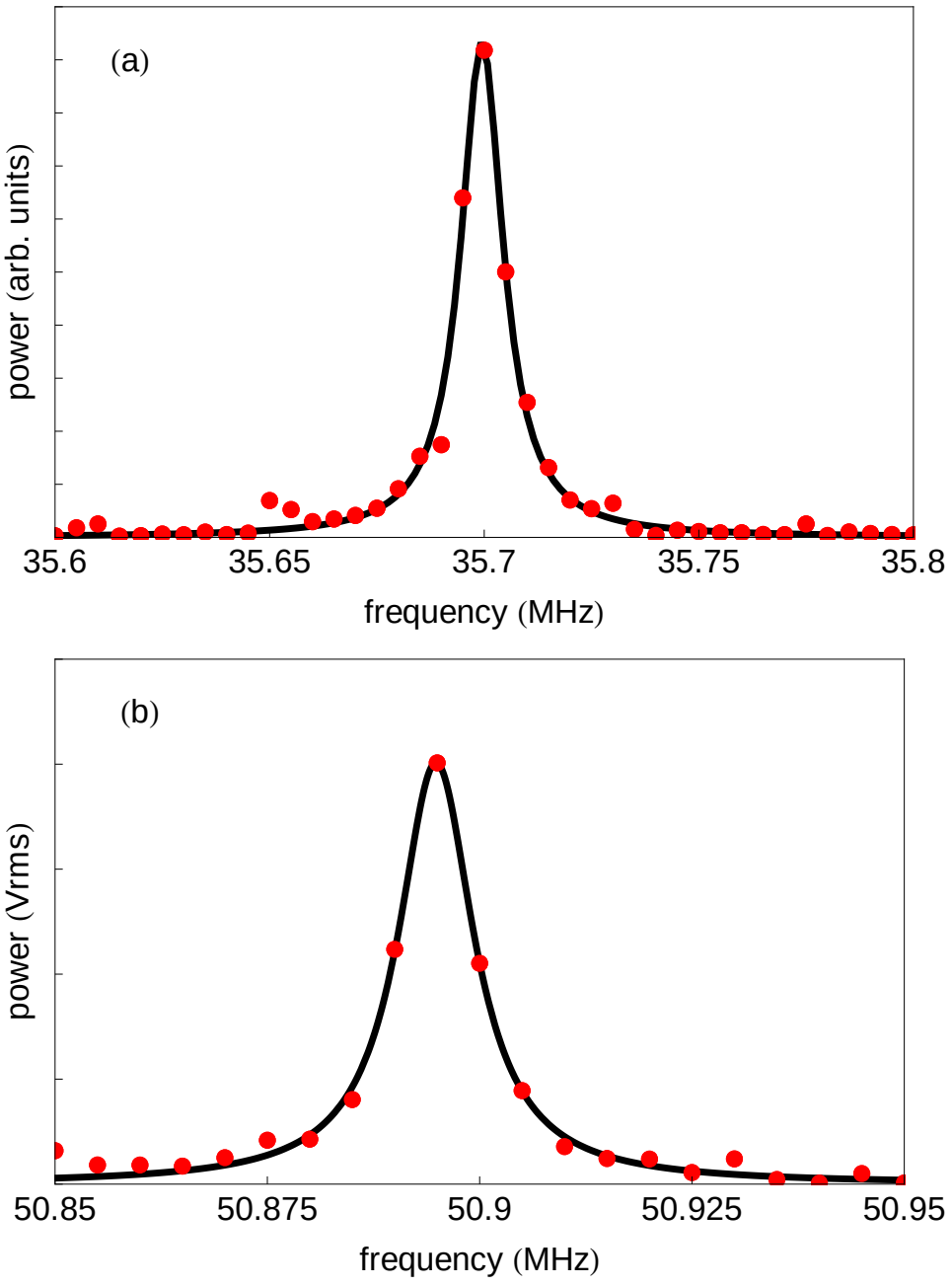

FIGURE 4.2: Measured ring-down spectra of (a) the center-of-mass mode (ω_z) and (b) the quadrupole (ω_2) mode. The mode frequencies are determined by the Lorentzian fit shown in black.

The ring-down-detection technique can determine plasma oscillation frequencies with a precision of a few kHz in a single measurement. Multiple measurements can be averaged to reach a precision of 100 Hz in less than 1 minute.

Precise determination of internal plasma mode frequencies as well as knowledge of the number of particles in the plasma, allows one to compute both the plasma radius and density. For the measurement displayed in Figure 4.2, the measured frequencies are $\omega_z/2\pi = 35.6995 \pm 0.0005$ MHz and $\omega_2/2\pi = 50.8949 \pm 0.001$ MHz. The uncertainty in measured plasma mode frequencies is based on typical trial-to-trial fluctuations. The aspect ratio (α_p) is determined from Equation (2.23) to be 1.771 ± 0.001. The plasma frequency ω_p is calculated by substituting ω_z and α_p into Equation (2.23), resulting in $\omega_p/2\pi = 80.3681 \pm 0.0005$ MHz. The ω_p is related to the plasma density by Equation (2.24), resulting in $n = (8.012 \pm 0.003) \times 10^7$ cm^{-3} in this example.

The particle number N is determined by pulse counting the e^- or e^+ plasma after the plasma mode measurements are made. The uncertainty in the particle number N stems from the uncertainty in the charge-counting technique discussed in Sections 4.3 and 4.2.1. For this plasma, $N = (85 \pm 2) \times 10^6$. The plasma density n and the aspect ratio α_p are used to solve for the plasma radius r_p:

$$N = \frac{4}{3}\pi r_p^3 \alpha_p n. \tag{4.1}$$

The plasma radius is 5.24 ± 0.08 mm, which gives the plasma length $z_p = 9.28 \pm 0.08$ mm, since $\alpha_p = z_p/r_p$. This example demonstrates that all plasma parameters can be determined from measurements of N, ω_z, and ω_2. This measurement process is fast and precise, allowing us to track small changes in the internal dynamics of a plasma.

Plasma-mode measurements can be used to monitor radial plasma expansion over time. This is especially important when designing nested potential wells for Rydberg positronium and $\overline{\text{H}}$ production. Antihydrogen production trials can last for up to 40 minutes. In these cases, slow plasma expansion can slow $\overline{\text{H}}$ production by decreasing the e^+ plasma density. Maintaining a small-radius plasma is also

important in trials using the Ioffe trap wherein particles at large radii can be lost on the electrode stack walls (as discussed in Section 2.1.4). Figure 4.3 shows the ω_z and ω_2 modes over ten minutes. The increasing ω_2 indicates an increasing radius - from 4.67 mm to 5.14 mm in this example.

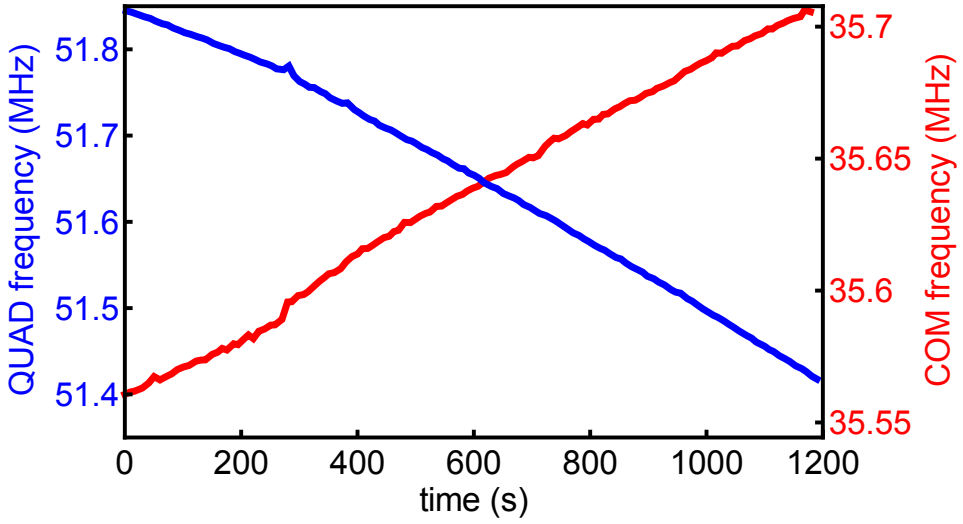

FIGURE 4.3: Plasma modes are monitored over time to determine the radial expansion of plasmas in holding potential wells.

4.2 Positron Counting

Positrons can be counted by charge counting or by counting annihilation signal, as described in the following sections.

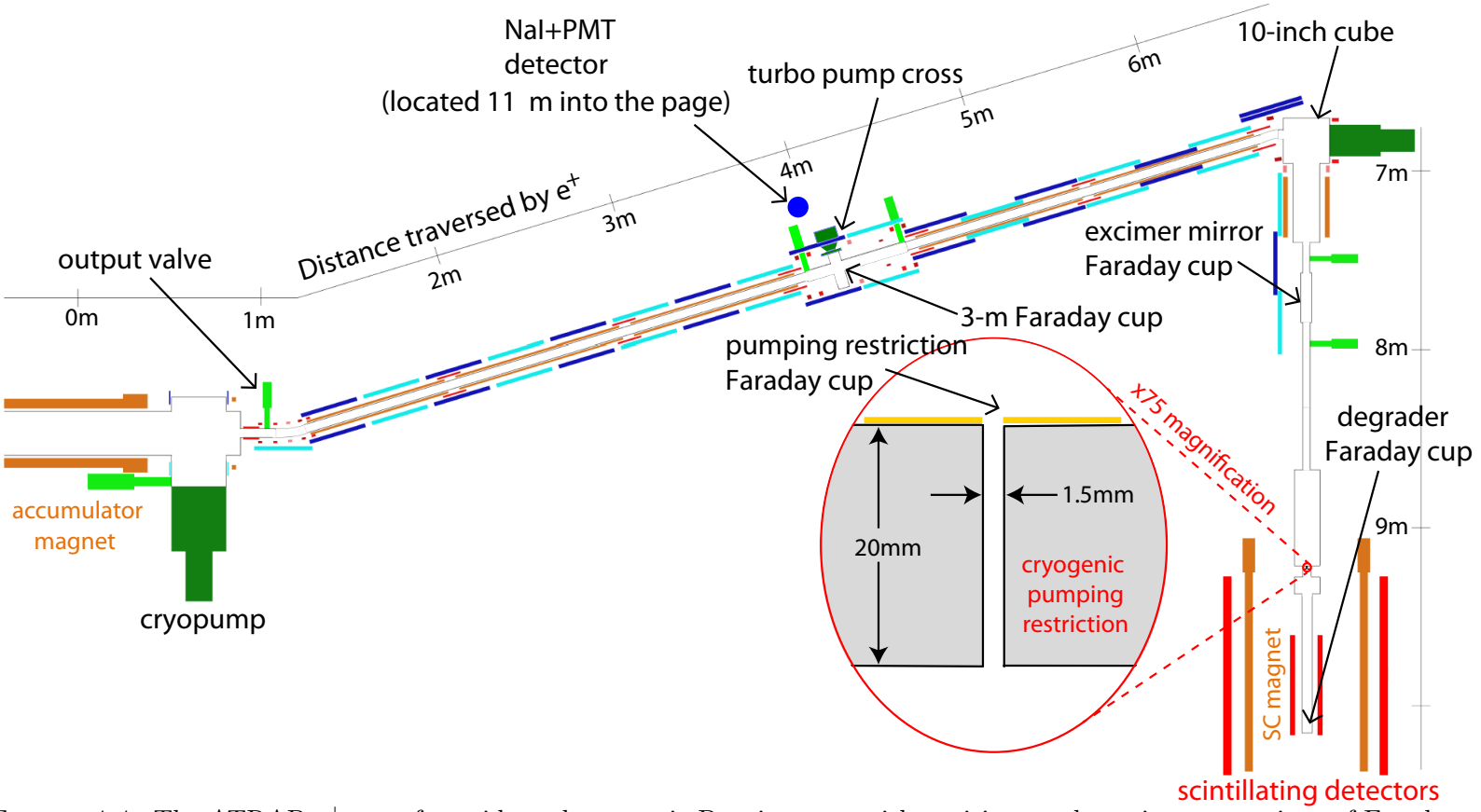

FIGURE 4.4: The ATRAP e^+ transfer guide and cryogenic Penning trap with positions and naming conventions of Faraday cups.

4.2.1 Charge Counting

Quantitative e^+ counting in the e^+ transfer guide and cryogenic Penning trap (Figure 3.2) is done with Faraday cups and charge-sensitive amplifiers. The position of these Faraday cups is shown in Figure 4.4. The number of e^+ can be determined via charge counting on the 3-m Faraday cup (so named because it is located 3 m from the output valve of the accumulator in Figure 4.4), excimer-mirror Faraday cups, pumping-restriction Faraday cups, as well as on the Be degrader used as a Faraday cup.

When a non-neutral plasma of e^+ suddenly impacts the surface of a Faraday cup, the induced charge can be measured to determine the number of e^+ in the plasma. ATRAP uses charge-sensitive amplifiers designed by Dr. Andrew Speck [56].

The charge-sensitive-amplifier circuit is shown in Figure 4.5. It is basically an operational amplifier with a feedback capacitor to give $V_{\text{out}} = \frac{Q_{\text{in}}}{C_{\text{eff}}}$, where the effective capacitance (C_{eff}) takes both the feedback capacitor (C_f) in Figure 4.5, and the capacitance of the cable (C_{cable}) into account. The R=300-MΩ resistor in parallel with C_f causes the charge stored in the capacitor to be drained away with the characteristic time constant of the RC circuit (300 μs for a $C_f = 1$ pF capacitor). A typical charge-sensitive-amplifier output (for an incident cloud of 2.15×10^7 e^+) is shown in Figure 4.6.

The charge-sensitive amplifier for each Faraday cup needs to be individually calibrated due to varying cable lengths, and, thus, each Faraday cup has its own value of C_{eff}. C_{eff} is measured experimentally using a test voltage supplied from a DG535 pulse generator, a calibrated capacitor (C_{cal}), and a 40-dB attenuator, as shown in Figure 4.5. A comparison of the input and measured voltages gives C_{eff} :

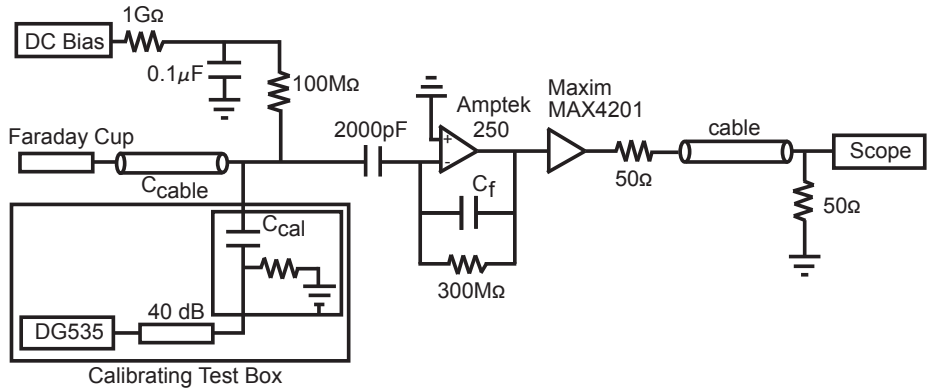

FIGURE 4.5: The charge-sensitive-amplifier circuit that is used to measure the induced voltage from charged particles hitting the surface of a Faraday cup.

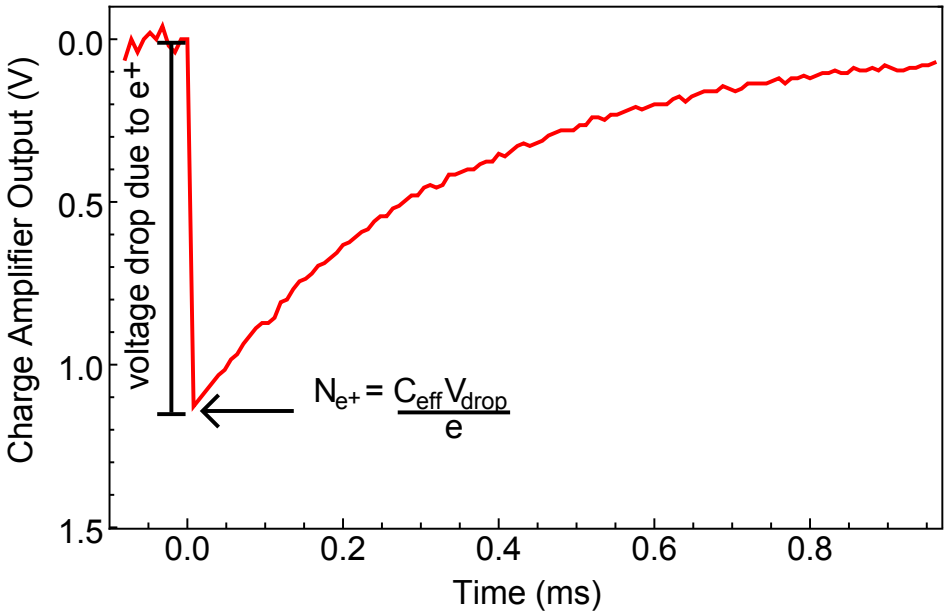

FIGURE 4.6: A typical charge-sensitive-amplifier output for an incident e^+ cloud. The measured voltage drop is proportional to the number of particles incident on the Faraday-cup surface.

$$C_{\text{eff}} = C_{\text{cal}} \left(\frac{V_{\text{in}}}{V_{\text{drop}}} - 1 \right). \tag{4.2}$$

As e^+ collide with the surface of the Faraday cup, there is a chance that they will eject one or more e^- from the surface of the metal before moving deeper into the material and annihilating with an e^-. One ejected e^-, together with the e^+ annihilation of a different e^- deeper in the material, creates a net charge on

the Faraday cup of +2e. Electrons ejected from the Faraday cup surface in this manner are called secondary e^-.

Secondary e^- ejection must be suppressed in order to make an accurate measurement of the number of e^+. Data taken with low-energy beams of e^+ and e^- show that secondary e^- are ejected with only a few eV of energy [57]. The suppression of secondary e^- is accomplished by positively biasing Faraday cups when counting e^+. Figure 4.7 shows the voltage drop measured on a Faraday cup as a function of the bias voltage applied to the Faraday cup (in this case, the 3-m Faraday cup in Figure 4.4). The results show that the voltage drop decreases when even a small positive bias is applied. The measured voltage drop is stable to within ±10% after secondary e^- ejection is suppressed (by +10 V) up until the bias is comparable to the kinetic energy of the e^+, at which point the 60-eV e^+ are repelled from the Faraday cup and the measured voltage quickly drops to zero.

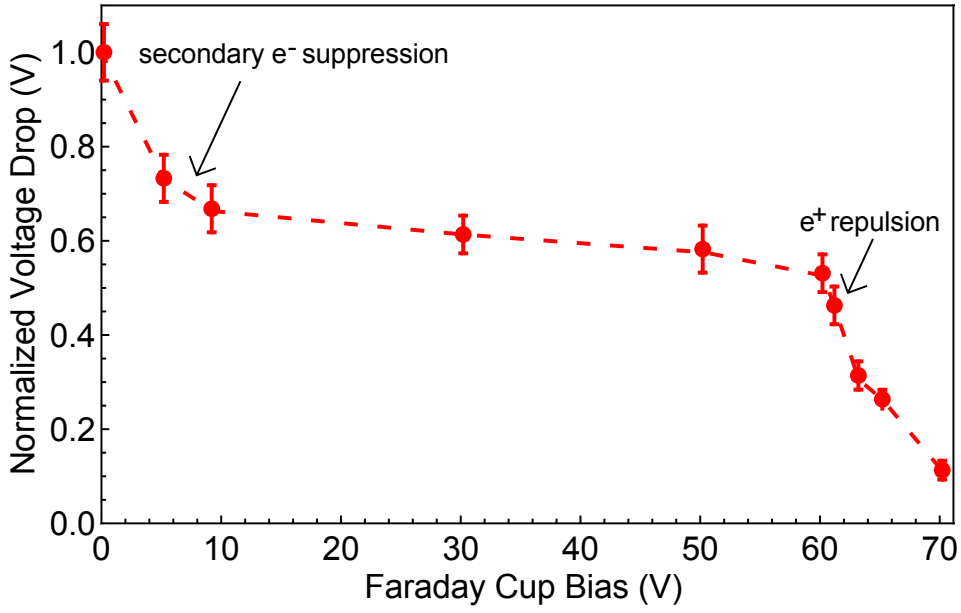

FIGURE 4.7: The voltage drop measured by a charge-sensitive amplifier as a function of the bias applied to the Faraday cup. A 10-V bias suppresses secondary e^- ejection. The 60-eV e^+ are repelled from the Faraday cup for a bias of > 60 V. The dashed line is added to help guide the eye.

A comparison of the charge-sensitive amplifier output with 0-V and 9-V bias is shown in Figure 4.8. The charge-sensitive-amplifier output in the 0-V case displays

a larger voltage drop than the 9-V case, as well as a sharp, downward spike at the moment the e^+ hit the surface of the Faraday cup. The voltage drop in the 0-V case is 50% larger than in the 9-V case due to the ejection of secondary e^-, which is suppressed in the 9-V case. The explanation for the sharp, downward spike is not known; it is not likely the result of secondary e^- ejection, since the ejected e^- is not expected to return to the Faraday cup surface. In any case, the properly-biased measurements (Figure 4.8) are used to measure the number of e^+, and, for these, the feature is absent.

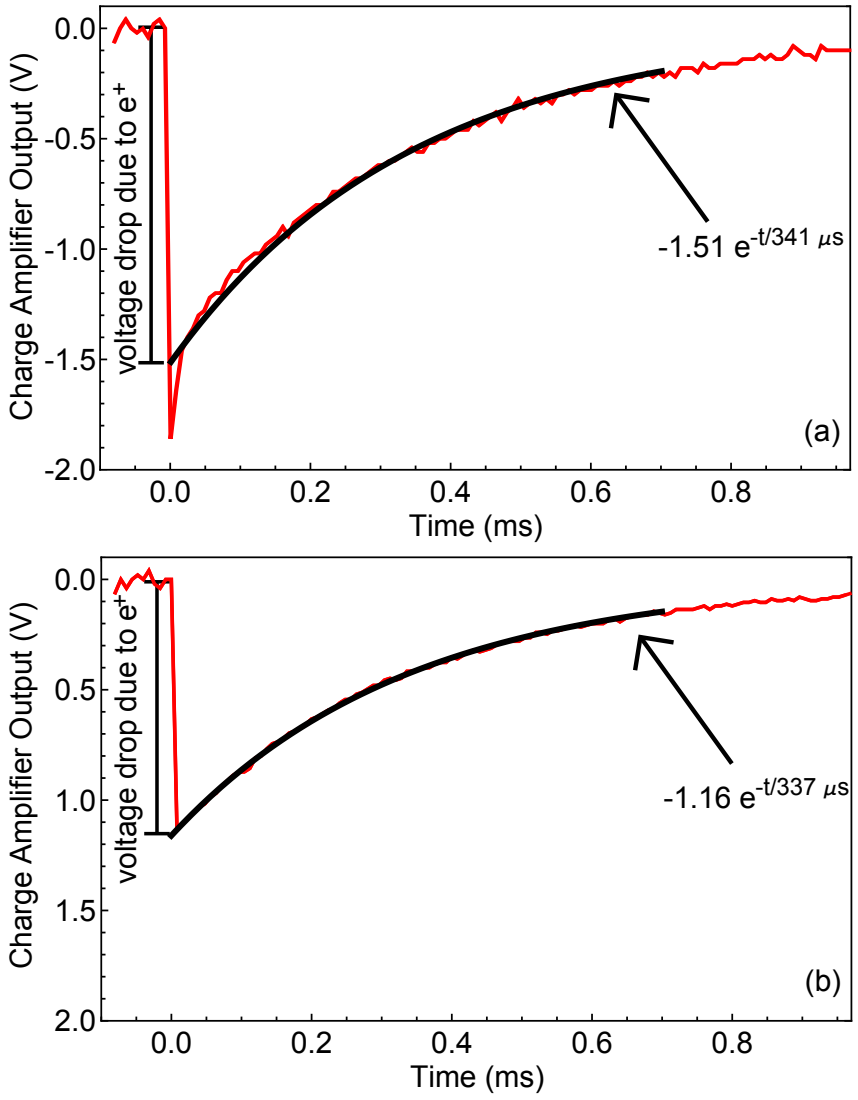

FIGURE 4.8: The voltage drop measured by a charge-sensitive amplifier using 2.15×10^7 e^+ with 0 V (a) and 9 V (b) applied to the Faraday cup. The fitting function demonstrates that the 0-V case is inconsistent with the expected exponential decay.

The degrader charge-sensitive amplifier becomes saturated when the input voltage approaches the value of the gate voltage of the preamplifier op-amp, preventing the counting of very large plasmas of e^+. Plasmas of up to 10^9 e^+ or more can be attained in the cryogenic Penning trap, and these plasmas are counted in increments to avoid saturation of the charge-sensitive amplifier. The electrode stack potentials for e^+ counting are shown in Figure 4.9. The potential well holding the e^+ is pulsed up by 2.5 V. If the potential well is shallow enough, some e^+ will escape the potential well. A positive bias is applied to the electrode directly above the e^+ to force them towards the degrader, and an electric potential gradient is created using the electrodes below the e^+ in order to block secondary e^- ejection from the degrader. The DC well depth is then decreased by 2.5 V, as indicated by the dashed lines in Figure 4.9, and another 2.5 V pulse repeated. This procedure is repeated until the potential well holding the e^+ is inverted. Figure 4.10 shows the results of such an incremental measurement for a plasma of 1.8×10^7 e^+.

4.2.2 Annihilation Counting

The scintillating fibers of the cryogenic Penning trap detector system offer an alternate e^+ counting technique. The scintillating fibers were designed to detect $\bar{p}$, but have some sensitivity to 511-keV γ's. The detection efficiency for e^+ that annihilate on the degrader at the bottom of the cryogenic Penning trap is measured using a calibrated number of e^+. Three e^+ ejections from the positron accumulator are repeatedly trapped, cooled, and charge-counted in the cryogenic Penning trap, resulting in an average of $3.36(10) \times 10^7$ e^+. Another set of three e^+ ejections are loaded into the cryogenic Penning trap and ejected towards the degrader. The annihilation γ's from these e^+ are detected by the scintillating fibers, with an average $1.65(5) \times 10^5$ γ's detected. Therefore, each γ detected by the scintillating fibers indicates the annihilation of 203 (6) e^+. A similar experiment was performed in 2009 to measure the efficiency with which the scintillating fibers detect e^+ that

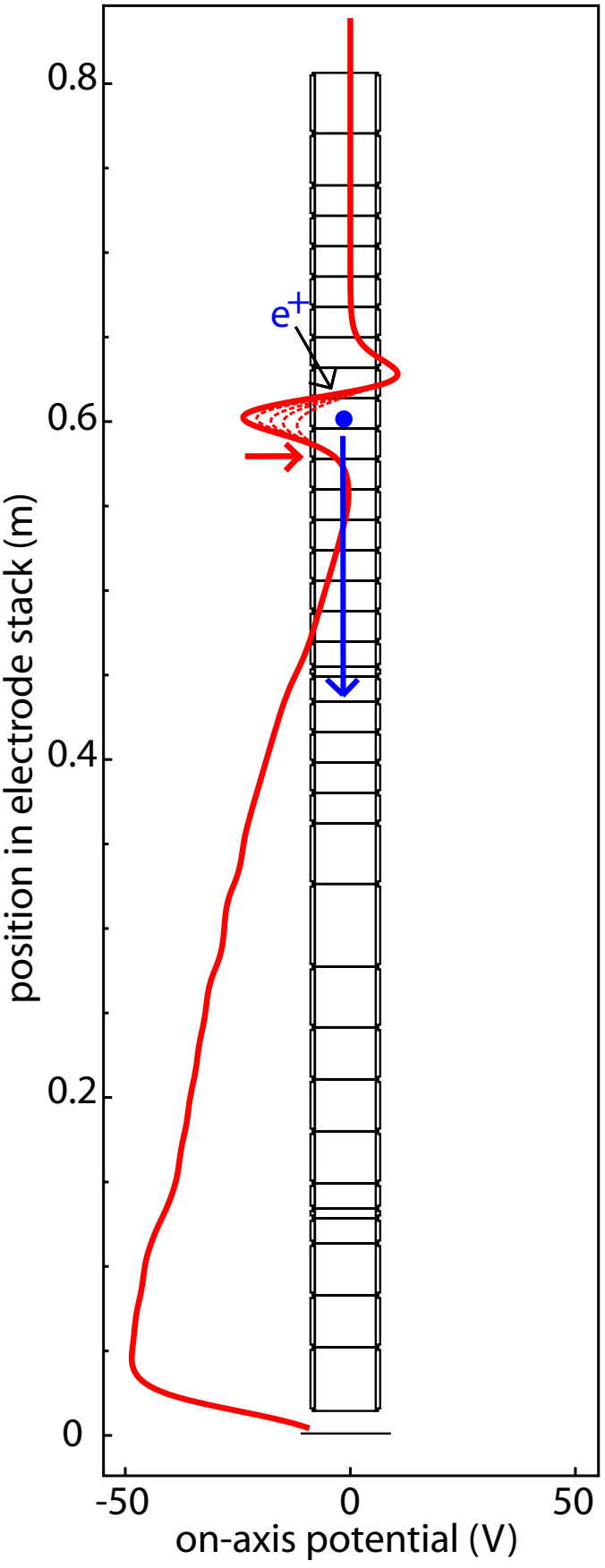

FIGURE 4.9: On-axis potential used to charge-count e^+. Dashed lines show the potential well depth decreasing in 2.5-V steps to eject particles.

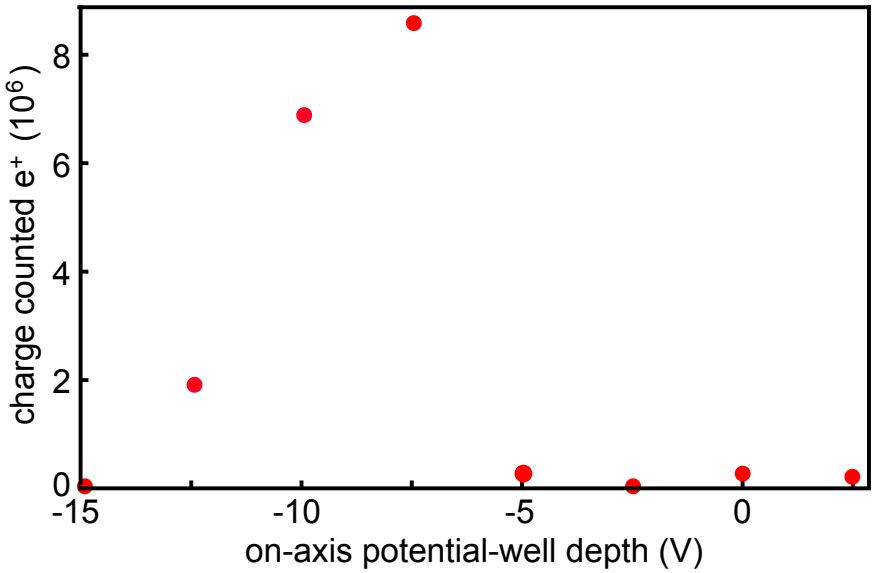

FIGURE 4.10: Positrons are incrementally counted using eight 2.5-V steps using the potential of Figure 4.9 and the degrader as a Faraday cup. The sum of the e^+ from each of the eight steps is the total number of e^+ held in the potential well, which is 1.8×10^7 e^+ in this example.

annihilate in the Ioffe field region. Approximately 2×10^7 e^+ were loaded into the cryogenic Penning trap and confined in an electrostatic potential while the Ioffe field was energized. The depth of the potential well was decreased. Positrons that escaped the potential well followed magnetic field lines into the electrode stack walls. The annihilation γ's from these e^+ were detected by the scintillating fibers. Approximately 2×10^7 e^+ resulted in approximately 1.67×10^5 detected γ's. Therefore, each γ detected by the scintillating fibers indicates the annihilation of approximately 87 e^+. The Ioffe magnet is near the center of the scintillating fiber ring, as shown in Figure 3.8, which explains the higher detection efficiency for e^+ annihilating near the Ioffe trap compared to the efficiency for e^+ annihilating at the bottom of the cryogenic Penning trap.

Figure 4.11 shows a typical example of fiber counts seen as the potential well holding 10^8 e^+ is slowly emptied. The voltage for the potential well holding the e^+ (Figure 4.9) is reduced by a smooth, linear ramp, instead of the voltage steps and pulsing used in charge counting. A multichannel scaler acquires fiber detector

data.

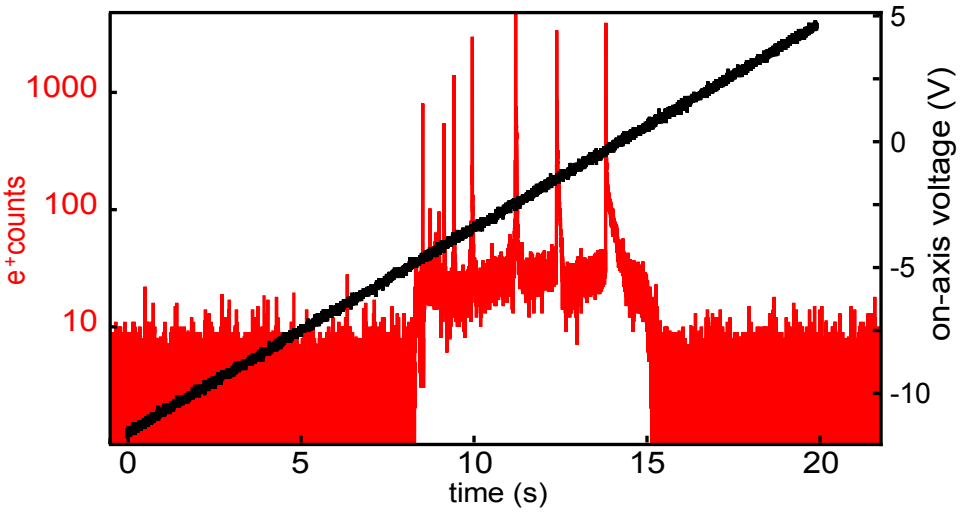

FIGURE 4.11: Positron annihilations (determined by fiber detector counts/203) and potential-well voltage as a function of time.

The cause of the spikes in the data of Figure 4.11 is not well understood. One possible cause could be noise in the voltage sources of the electrodes resulting in sudden changes in the depth of the potential well holding the e^+, and, thus, causing a sudden increase in the number of e^+ that escape the potential well. The total fiber count (including these spikes) integrated over the whole ramp time gives a reliable and reproducible method for determining the total number of e^+ in a plasma.

4.3 Electron Counting

Since e^- do not annihilate upon contact with the walls of the electrode stack, the only option for e^- counting in the cryogenic Penning trap is charge counting using a charge-sensitive amplifier on the degrader (used as a Faraday cup). When a cloud of e^- is pulsed onto a Faraday-cup surface, the induced negative charge can be measured to determine the number of e^- in the cloud. The output is similar to that from e^+ charge counting except that the signal is of the opposite sign.

Figure 4.12 shows the electrode stack settings used to count large e^- plasmas. Electrons are held in a potential well on electrode LTE3. The barrier below this well is pulsed down and e^- are allowed to escape, while a potential barrier above this well prevents e^- from exitting in the upward direction. The depth of the potential well holding the e^- is decreased in steps of 2.5 V, and the barrier below the e^- is again pulsed, releasing the next bunch of e^-. Like e^+, incoming e^- can eject secondary e^- from a metal surface [57]. A potential ramp to the degrader (as shown in Figure 4.12) returns any secondary e^- to the degrader. Figure 4.13 shows results for counting a cloud of approximately 10^8 e^- using this method.

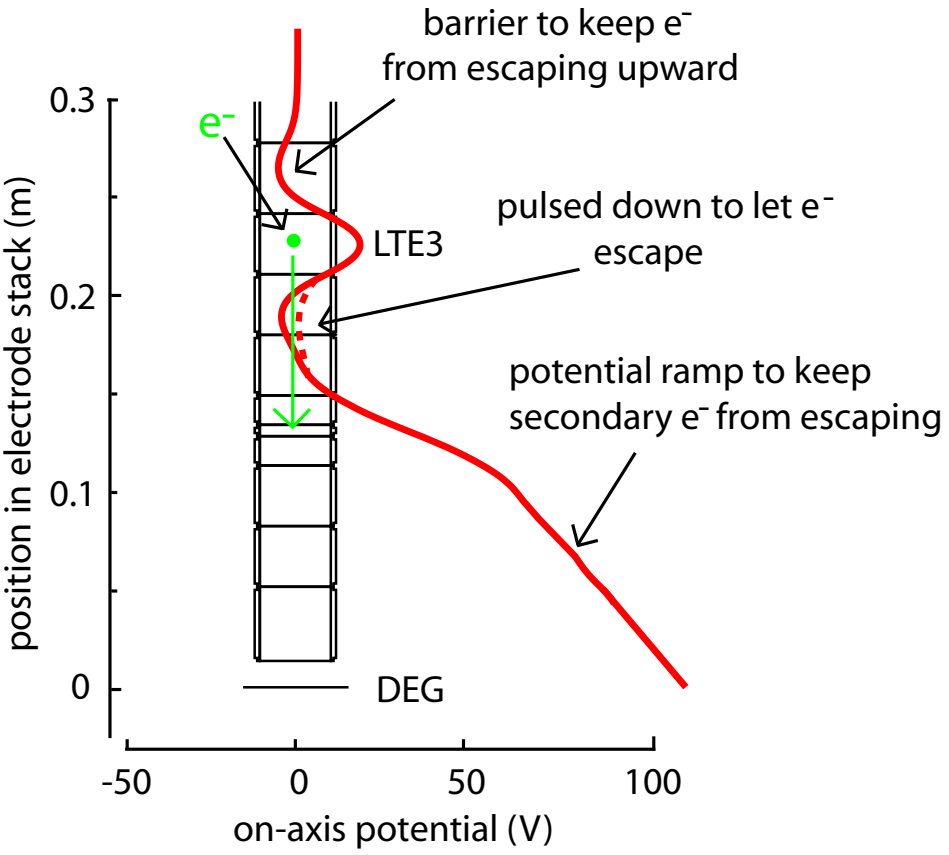

FIGURE 4.12: On-axis potentials used to count e^-. The dashed line shows the changed potential well barrier being pulsed down to eject e^-.

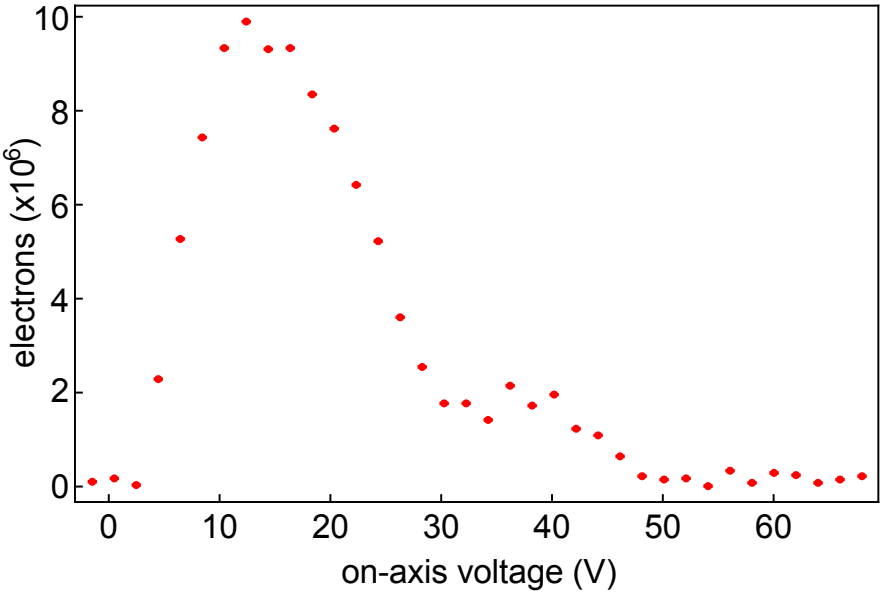

FIGURE 4.13: Electrons are incrementally counted using the degrader as a Faraday cup in the cryogenic Penning trap. The total number of e^- is determined from the sum of the measurements at each voltage step — in this case $9.7(7) \times 10^7$ e^-.

4.4 Lepton Counting Comparison

I performed a detailed comparison of e^+ and e^- charge-counting techniques in the ATRAP cryogenic Penning trap using the degrader Faraday cup (Figure 4.4). The goal of the experiment was to create plasmas with identical numbers of e^+ or e^- and count them using the charge-counting techniques described in Section 4.2.1 and 4.3. If secondary e^- ejection is properly suppressed, and if the 1022 keV from the e^+ annihilation does not eject additional charges from the Faraday cup, then plasmas with identical numbers of e^+ or e^- will induce identical charges on the degrader Faraday cup.

The first step in this comparison is to create e^+ and e^- plasmas with very nearly the same particle number and shape. Approximately 1.5×10^8 e^+ or e^- are loaded into the cryogenic Penning trap. A rotating electric field (so-called rotating wall) is used to control the radial extent of the plasma, as described in Section 7.1.2. The rotating-wall scheme with the 7-electrode-long potential well (the red curve in

Figure 7.2) and 5-MHz, 2-V_{rms} drive is applied for 160 s. Upon completion of the rotating-wall drive, the aspect ratio of the plasma is measured using the modes measuring technique described in Section 4.1. The aspect ratio for these plasmas range between 2.5 and 3.0.

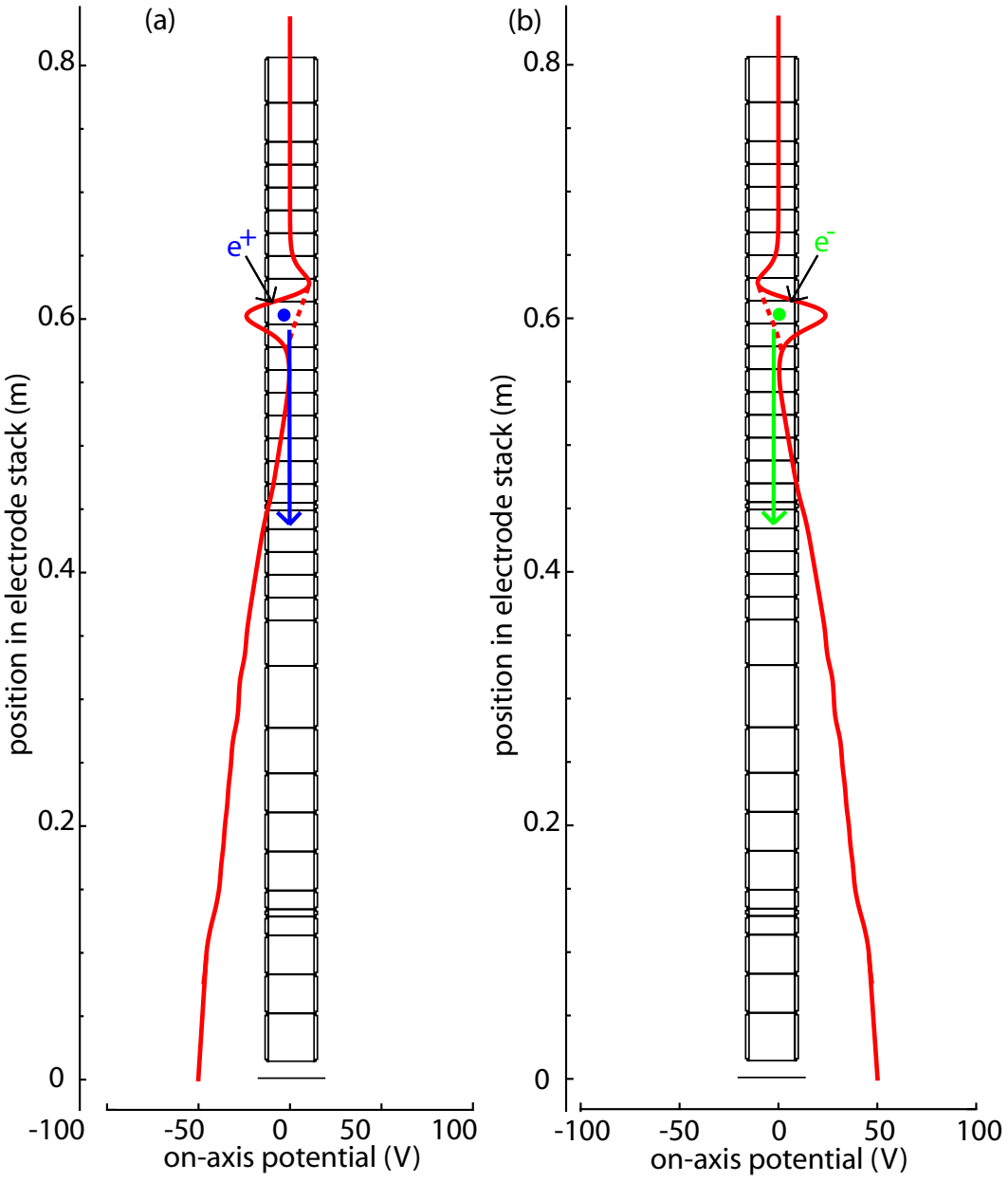

FIGURE 4.14: Electrode stack settings to remove most of the particles in e e^+ plasma (a) and e^- plasma (b).

The next step is to create plasmas with nearly identical numbers of particles. The e^+ or e^- plasma is held in a single-electrode well in the upper part of the electrode

stack, as in Figure 4.14. The depth of the potential well that holds the particles is decreased from 100 V to a selected voltage between 0.76 V and 10.0 V, such that most of the initially loaded particles escape the potential well. By dumping most of the particles out of the well, any strong dependency of the remaining number of particles on the initial shape and number of particles in the plasma is removed. This fact is demonstrated in a separate experiment where large numbers of e^- (1.5, or 2.0 $\times 10^8$) are loaded into the cryogenic Penning trap and compressed to various aspect ratios using the rotating wall (Section 7.1.2). The depth of the potential well holding the e^- is decreased to 5.1 V, as in Figure 4.14(b), such that most of the particles escape, and the remaining e^- are counted, as in Section 4.3. The results, shown in Figure 4.15, demonstrate that, when using large numbers of particles, the number of e^- remaining after the potential well depth is decreased is not very dependent on the initial aspect ratio of the e^- plasma.

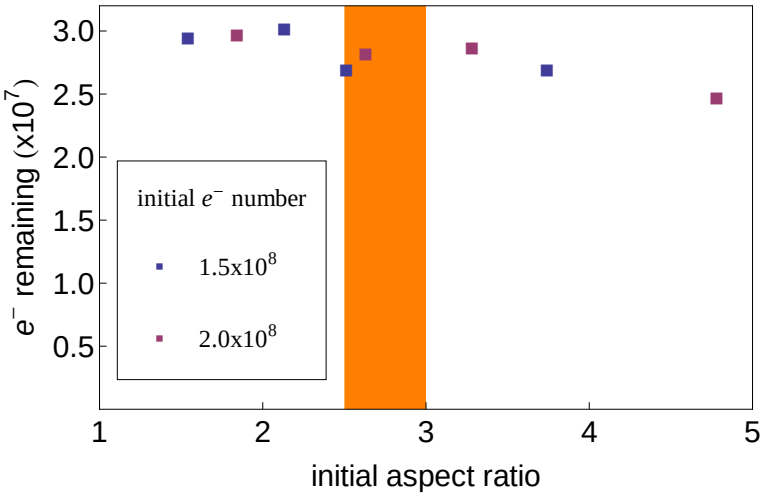

FIGURE 4.15: e^- plasmas are compressed to various aspect ratios before most of the particles are removed by decreasing the depth of the potential well to 5.1 V (Figure 4.14(b)). This experiment demonstrates that the number of e^- remaining is not very dependent of the shape of the plasma for large numbers of initial e^-. The range of aspect ratios used in the charge-counting experiment is shown in orange.

In the final step of the experiment, the particles remaining after the potential well is reduced are counted using the charge-counting techniques discussed in

final on-axis potential (V)	$e^-(\times 10^6)$	$e^+(\times 10^6)$
0.76	3.8 (0.2)	5.6 (0.6)
1.5	8.0 (1.3)	9.8 (0.3)
2.1	12.8 (0.7)	13.8 (0.4)
2.6	15.0 (0.8)	16.9 (0.5)
5.1	31.5 (0.1)	31.9 (0.9)
7.4	45.0 (1.0)	44.6 (0.4)
10.0	61.4 (0.3)	61.0 (0.6)

TABLE 4.1: Results of calibrated-charge counting e^+ and e^-. The first column gives the final on-axis depth of the well used to hold the e^+ or e^- after the voltage has been reduced to let most of the particles escape.

Section 4.2.1 and Section 4.3. The experiment is repeated twice for each final-potential-well depth and particle type (e^- or e^+). The average and standard deviation for each final-well depth and particle type is displayed in Table 4.1.

The data in Table 4.1 are plotted in Figure 4.16. The rms uncertainty (7.5×10^5) is applied to all points in Figure 4.16. The e^+ and e^- counts are in agreement to within approximately this uncertainty. A straight line (forced through the origin) is fit to the combined e^+ and e^- data, resulting in a slope of $6.08(3) \times 10^6$ $e^{+/-}$per V. Even though the processes that produce secondary e^- are very different for e^+ and e^-, the same number of charges is counted when the Faraday cup is appropriately biased. The level of agreement between the e^+ and e^- data in Figure 4.16 indicates the necessity to bias a charge-counting surface in order to obtain accurate counts of charged particles. The agreement also shows that the 1022 keV of energy deposited when the e^+ annihilates in the Faraday cup does not eject any additional charges and, thus, does not affect the charge-counting measurement. This measurement is the most precise test of e^+ charge counting, and was performed because no other such test could be found in the literature.

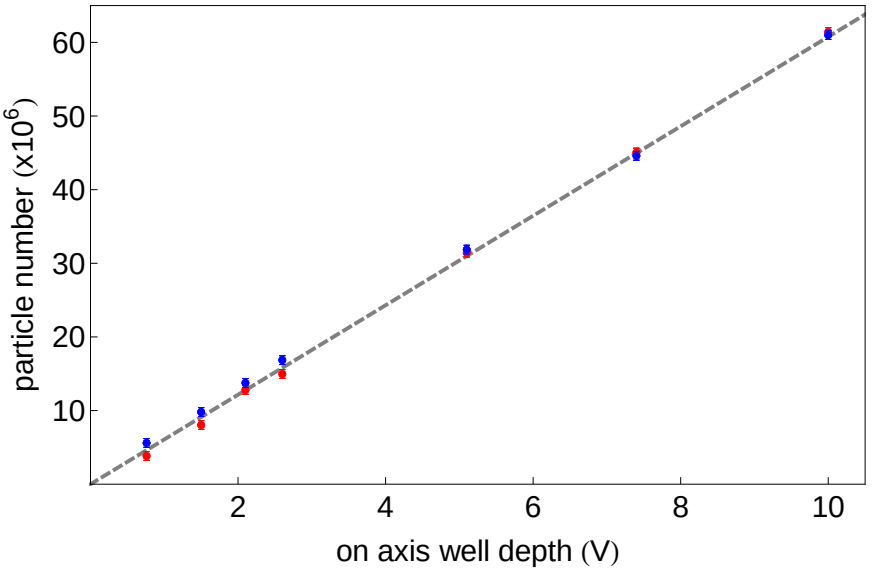

FIGURE 4.16: Lepton charge counting comparison of e^+ (blue) and e^- (red). The number of leptons counted agrees between the two species over a wide range of lepton number. A straight line forced through the origin is fit to the data. The slope of the line is $6.08(3) \times 10^6$ $e^{+/-}$per V.

4.5 Antiprotons

ATRAP uses the charged pions that result when $\bar{p}$ collide with matter to count $\bar{p}$. The $\bar{p}$-p annihilation event results in (on average) three charged pions and (on average) two neutral pions [58].

The charged pions can be detected using the scintillating fibers and paddles of the cryogenic Penning trap detector system detailed in Section 3.1. Pions resulting from $\bar{p}$ annihilation in the Ioffe-trap region pass through the Penning trap electrodes, the Ioffe trap, two layers of fibers, the 1-T superconducting solenoid, and then two layers of paddles. Signals from the fibers and paddles are used to partially reconstruct the paths of the charged particles and decide whether the detected event was more likely due to an $\bar{p}$ annihilation or due to a background high energy particle. Such background high-energy particles are mostly cosmic rays, but could possibly also result from CERN-generated particles. By using only the paddle coincidence counts (i.e., when one large outer paddle and one of its small

inner paddles both have signals in the same 50-ns time bin), an $\bar{p}$ detection efficiency of 75% is achieved, with a background count rate of 450 Hz. To decrease the background count rate, the fiber detectors are also used. A 'trigger-1' count results from at least one of the fiber layers having a signal within the 50-ns time bin of the coincident paddle count. 'Trigger-1' counts are less efficient than paddle counts — detecting 48% of $\bar{p}$ annihilations at the bottom of the electrode stack and 54% of $\bar{p}$ annihilations near the center of the Ioffe trap — but the background count rate decreases to 30 Hz. The lower-background $\bar{p}$ count ('Trigger-2') results when two fiber layers have coincident signals with the pair of paddles (within the 50-ns time window). 16% of $\bar{p}$ annihilations at the bottom of the electrode stack are detected, and 20% of $\bar{p}$ annihilations near the center of the Ioffe trap are detected, but the background count rate decreases to 4 Hz.

The cryogenic Penning trap detector system can be used to continuously monitor $\bar{p}$ losses during particle manipulations or $\overline{H}$ production trials, or to count $\bar{p}$ ejected from a potential well. Counting the number of $\bar{p}$ in a potential well is performed by monitoring the scintillating detectors while slowly decreasing the depth of the potential well (and then inverting it) to dump out all of the $\bar{p}$. The results of dumping approximately 9.5×10^5 $\bar{p}$ towards the degrader are shown in Figure 4.17(a).

Such a dump of $\bar{p}$ can also be used to determine the temperature of the $\bar{p}$ plasma, as in Figure 4.17(b). The rate at which the first thousand $\bar{p}$ leave the potential well is used to determine the temperature of the $\bar{p}$ plasma, using a technique similar to reference [59]. Assuming that the $\bar{p}$ axial energy may be described by the Maxwell-Boltzmann distribution, the number of $\bar{p}$ lost (dN) while the potential-well depth is decreased by increment dW is [60]

$$\frac{dN}{dW} = \frac{N}{\sqrt{\pi W k_B T}} e^{\left(-\frac{W}{k_B T}\right)}. \tag{4.3}$$

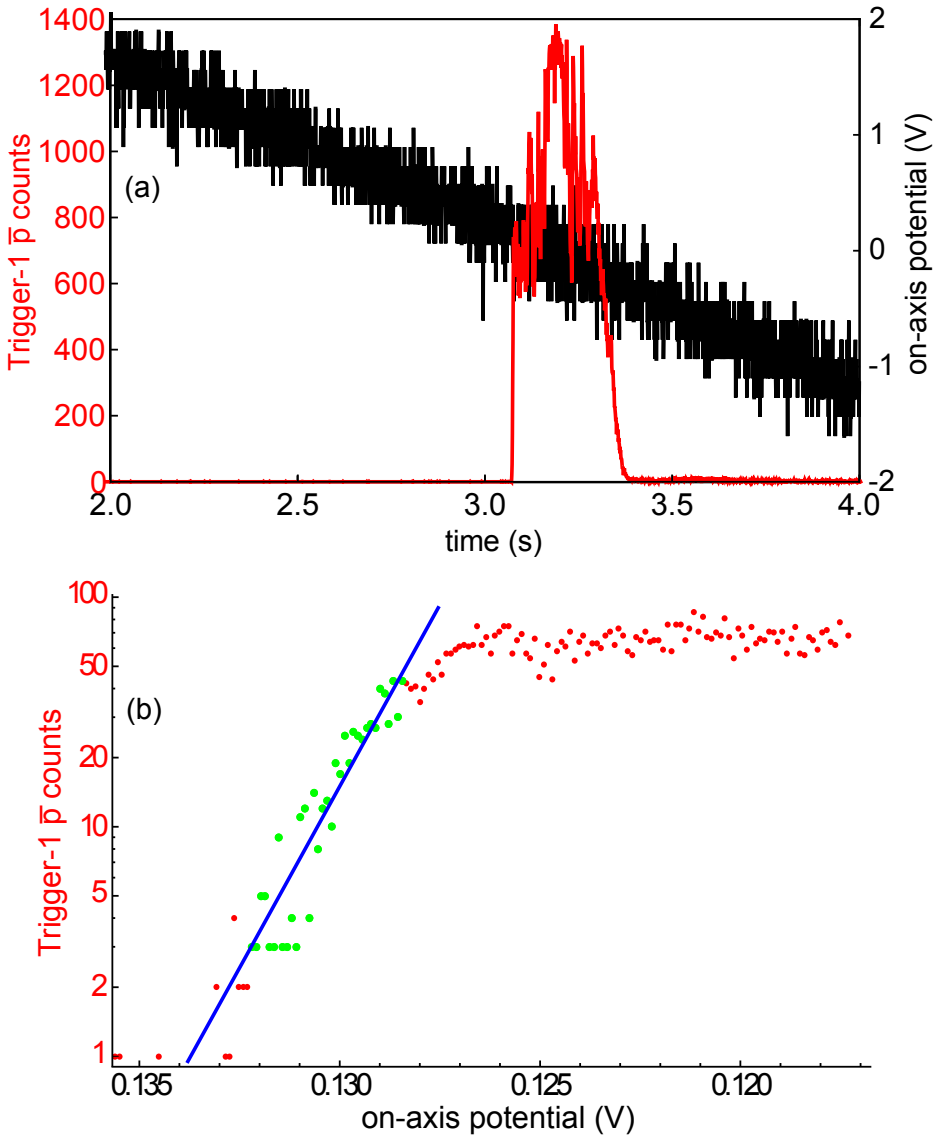

FIGURE 4.17: Annihilation counting of $\bar{p}$ in the cryogenic Penning trap (a). The number of $\bar{p}$ (9.5×10^5) is the sum of the Trigger-1 counts divided by the 0.75 efficiency. The $\bar{p}$ temperature (17 K in this example) is measured from the slope of the first thousand $\bar{p}$ to escape the potential well (b).

Taking the ln of both sides yields an equation for a line with slope $(k_b T)^{-1}$:

$$ln(\frac{dN}{dW}) = -\frac{W}{k_b T} + ln(\frac{N}{\sqrt{\pi k_b T}}) - \frac{1}{2} lnW. \tag{4.4}$$

Therefore, the plasma temperature is determined by fitting a line to the logarithm of dN/dW (the second and third terms are constant during the short time interval

needed to release the first thousand $\bar{p}$). Results of such measurements show that the $\bar{p}$ in our cryogenic Penning trap have a steady-state temperature of 17 K (Figure 4.17(b)). Adiabatic cooling of these $\bar{p}$ has resulted in temperatures of 3.5 K or lower [26].

4.6 Positron Temperature Measurements

The e^+ plasma temperature is a crucial parameter in $\overline{H}$ production trials. Slow e^+ are necessary to maximize the cross-section of Rydberg positronium production using two-stage charge exchange, where the cross section quickly drops if the e^+ have a larger speed than that of the Cs Rydberg e^-, or using three-body recombination (where, in the simplest approximation, the cross section is proportional to $T_{e^+}^{-9/2}$).

In principle, the e^+ temperature could be measured using the same technique used for $\bar{p}$ in Section 4.5. However, low-temperature plasmas have a steep slope of dN/dW — the rate at which particles leave the potential well as its depth is decreased. The low detection efficiency of our scintillating detectors for e^+ annihilations results in only a few points with which to determine dN/dW, leading to a fractional fit uncertainty of approximately 25%. Repeated measurements agree within this 25% uncertainty. High-temperature measurements have a much smaller slope, and, therefore, more data points with which to determine the plasma temperature, resulting in higher precision fits.

An alternate temperature measurement technique involves heating the e^+ plasma using a noise-broadened rf drive. When a plasma is heated, ω_2 will increase while ω_z remains constant [53]. The change in plasma temperature can be calculated based on the change in ω_2, as in Equation (2.26). The shifting plasma mode ω_2 is shown in Figure 4.18 as the heating rf drive is applied. The heating drive is

applied to the e^+ while they are ramped out of the potential well to measure their heated temperature, as in Figure 4.19. The hotter plasma will have a smaller value of dN/dW, making a precise measurement of that slope much easier. The final plasma temperature (T_f) is determined by measuring dN/dW and the change in temperature (ΔT) is measured by monitoring the plasma modes. The initial plasma temperature (T_i) is then calculated from $T_i = T_f - \Delta T$. The challenge in this technique is that the initial lepton temperature, based on $\bar{p}$ temperature measurements, is approximately 17 K, which is comparable to the uncertainty in the temperature of the heated e^+ plasma T_f. In order to make a useful determination of the lepton temperature, the precision in heated e^+ temperature measurements will have to be increased, either through repeated measurements or a more efficient detection scheme.

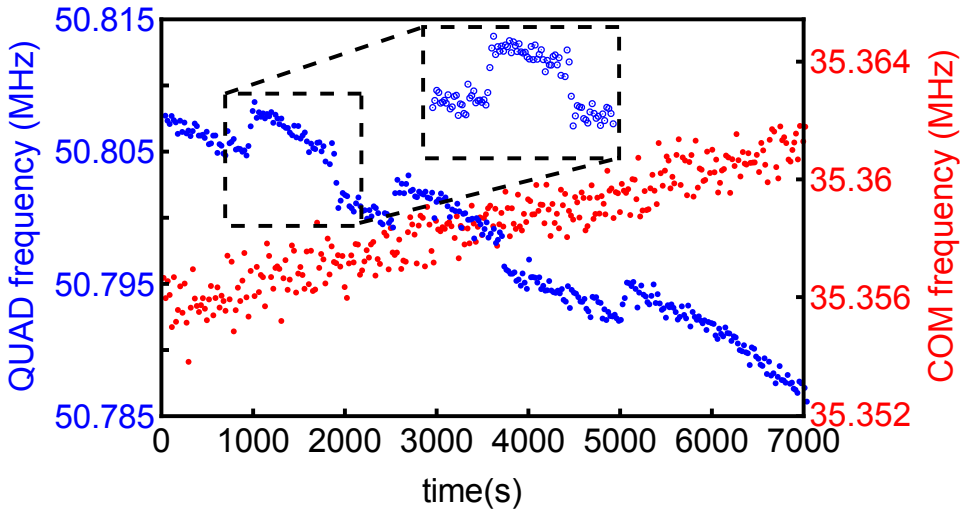

FIGURE 4.18: Lepton plasma modes are monitored as a heating rf drive is periodically applied. The ω_z (red) is unaffected by the drive while ω_2 (blue) has distinct shifts upward when the drive is applied (inset). The slow frequency drift over time is due to radial expansion of the plasma.

Another temperature measurement technique relies on a measurement of the next-higher-mode frequency (ω_3) and Equation 2.25 to determine the absolute value of the plasma temperature. The two mode frequencies would have different temperature dependencies so monitoring the change in both mode frequencies as a heating drive is applied would allow an absolute determination of the initial lepton plasma

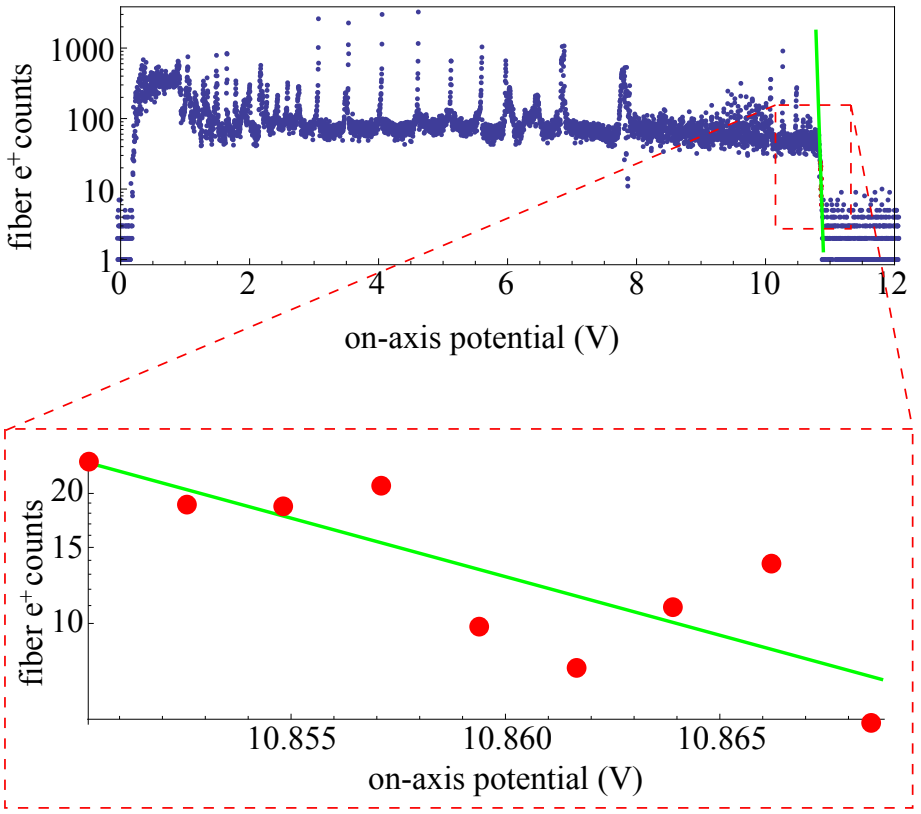

FIGURE 4.19: A heated e^+ plasma is ramped out of a potential well and a measurement of the plasma temperature is made using the first e^+ that leave the well. The slope of the green line indicates a e^+ temperature of approximately 95 (24) K

temperature. The current mode-measuring technique is not sensitive enough to detect this signal despite thorough searches near the predicted frequencies.

Chapter 5

ATRAP Positron Accumulator

5.1 Overview of the ATRAP Positron Accumulator System

The ATRAP positron accumulator (shown in Figure 3.2, with a more detailed version in Figure 5.1) is a buffer-gas accumulator based on the designs of the Surko group at the University of California, San Diego [25], [61], [62], [63]. Fast e^+ are provided by a radioactive ^{22}Na source (as described in Section 5.2) and are slowed in a layer of frozen Ne (as described in Section 5.3). Slow e^+ are magnetically guided (as described in Section 5.4) into the positron accumulator (described in Section 5.5), where they scatter off of N_2 molecules and become trapped. A rotating electric field (described in Section 5.5.3) radially compresses the e^+ plasma while elastic collisions with N_2 and a small amount of SF_6 further cools the e^+.

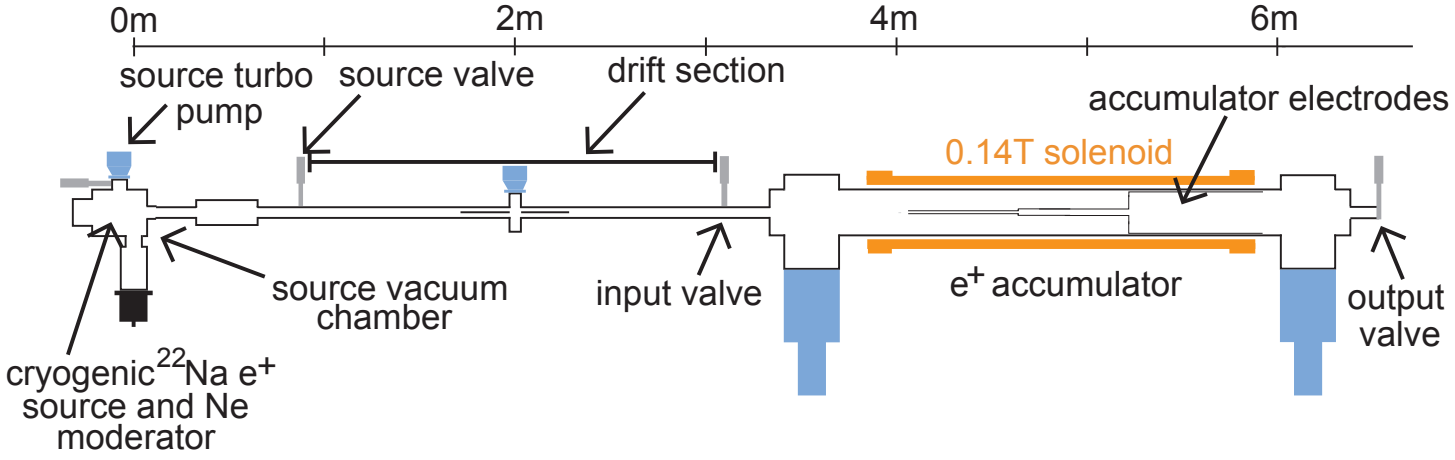

FIGURE 5.1: Schematic of the e^+ source, drift section, and positron accumulator.

5.2 Positron Source

5.2.1 ^{22}Na Source

The source of e^+ is a sealed sample of ^{22}Na. ^{22}Na is an unstable isotope (the decay scheme is shown in Figure 5.2) with a half-life of 2.602 years, decaying in one of two ways: beta decay, resulting in an emitted e^+ (90.57% probability)

$$^{22}_{11}Na \longrightarrow ^{22}_{10} Ne + e^+ + \nu_e, \tag{5.1}$$

and γ's emitted via electron capture (9.43% probability)

$$^{22}_{11}Na + e^- \longrightarrow ^{22}_{10} Ne + \nu_e + \gamma. \tag{5.2}$$

The emitted e^+ and ν_e of Equation (5.1) share 546 keV of kinetic energy [64].

The ^{22}Na is deposited into a source capsule by iThemba labs [65]. Small drops of a solution that contain the radioactive ^{22}Na are deposited onto a tantalum plate. The solution evaporates, leaving a radioactive salt behind. Tantalum is chosen because it is a high-Z metal, making it an efficient reflector of the e^+ that are emitted into the plate [66], [67]. Positrons exit the source capsule through a welded-on 5-μm-thick titanium window.

The source produces e^+ isotropically, with nearly 50% of e^+ emitted towards the titanium window. Of the other 50% that are emitted towards the tantalum backing, half are reflected back towards the window [68] resulting in approximately 75% of the emitted e^+ being directed towards the titanium window. Of these e^+, approximately half are absorbed (and annihilate) inside the source material itself while another 28% [69], are absorbed (and annihilate) in the thin titanium window. Thus, only approximately 27% of the e^+ emitted from the radioactive

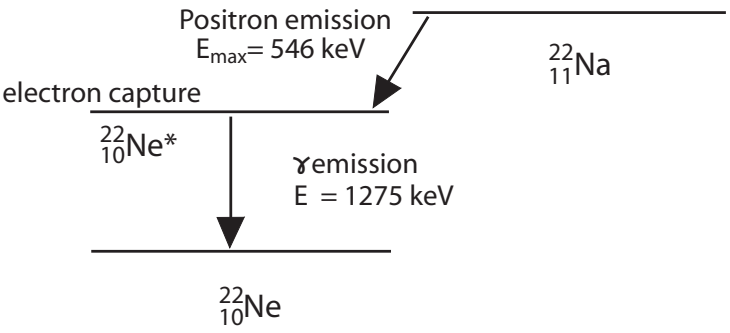

FIGURE 5.2: Decay scheme for ^{22}Na. ^{22}Na can decay via β^+ decay or via electron capture

material exit the Ti foil. The source was initially shipped with a measured activity of 52.5 mCi in October, 2006. As shown in Table 5.1, the source strength was only 21 mCi at the beginning of my thesis work (April 2010) and decreased to 5.4 mCi by the end of this work (April 2015).

5.2.2 Source Mount and Cold Finger

The ^{22}Na source capsule is carefully installed within the source vacuum system (Figure 5.3(a)) using the procedure outlined in the ATRAP source manual, which is shared with the radiation protection group at CERN. The source is placed and clamped into the source mount (Figure 5.3(a)), which is bolted onto a sapphire disk. The disk is mounted on a cold finger, which is cooled to 3 K by a mechanical refrigerator (SHI RDK408). Sapphire serves the competing necessities of high thermal conductivity at low temperatures and high electrical resistivity. High thermal conductivity is necessary to keep the source cold while a high resistivity makes it possible to independently bias the source and control the exit energy of the e^+. The thin titanium window of the source sits flush against a copper cone, as shown in Figure 5.3(a).

date	activity (mCi)	e^+ from ^{22}Na ($\times 10^9$/s)	e^+ exitting capsule ($\times 10^6$/s)
2007/01/01	49.8	1.66	450
2007/07/01	43.6	1.45	395
2008/01/01	38.1	1.27	345
2008/07/01	33.4	1.11	302
2009/01/01	29.2	0.97	264
2009/07/01	25.6	0.85	231
2010/01/01	22.4	0.74	202
2010/05/01	20.5	0.68	185
2010/09/01	18.8	0.62	170
2011/01/01	17.2	0.57	155
2011/05/01	15.7	0.52	142
2011/09/01	14.4	0.48	130
2012/01/01	13.1	0.44	119
2012/05/01	12.0	0.40	109
2012/09/01	11.0	0.37	99.7
2013/01/01	10.1	0.34	91.2
2013/05/01	9.22	0.31	83.5
2013/09/01	8.43	0.28	76.4
2014/01/01	7.72	0.26	69.9
2014/05/01	7.06	0.23	64.0
2014/09/01	6.46	0.21	58.5
2015/01/01	5.91	0.20	53.5
2015/05/01	5.41	0.18	49.0
2015/09/01	4.95	0.16	44.8
2016/01/01	4.53	0.15	41.0
2016/05/01	4.14	0.14	37.5
2016/09/01	3.79	0.13	34.3
2017/01/01	3.47	0.12	31.4
2017/05/01	3.18	0.11	28.8
2017/09/01	2.91	0.10	26.3
2018/01/01	2.66	0.09	24.1
2018/05/01	2.43	0.08	22.0
2018/09/01	2.23	0.07	20.2
2019/01/01	2.04	0.07	18.4
2019/09/01	1.86	0.06	16.9
2020/01/01	1.56	0.05	14.1
2020/07/01	1.37	0.05	12.4
2021/01/01	1.20	0.04	10.8
2021/07/01	1.05	0.03	9.48
2022/01/01	0.92	0.03	8.30

TABLE 5.1: Table of the iThemba source strength and e^+ yield over time.

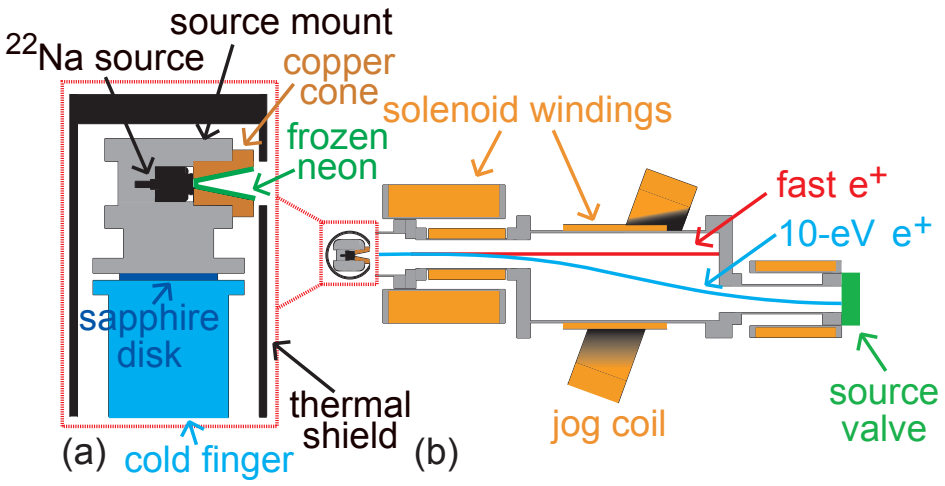

FIGURE 5.3: Schematic of (a) the ^{22}Na e^+ source and copper cone and (b) the solenoids that separate the slow e^+ from the fast (unmoderated) e^+. The 10-eV e^+ trajectory is bent by the jog coil while fast-e^+ trajectories are unchanged.

5.2.3 Source Vacuum Chamber

The source vacuum chamber (shown in Figure 5.1) is pumped on by a 4.5-inch, 80-l/s turbo pump (model ATP 80 by Alcatel). A high-quality vacuum is necessary to protect the frozen Ne moderator from vacuum impurities that could increase the e^+ annihilation rate.

The source vacuum chamber is filled with copper blocks that surround the radioactive source in order to reduce the radioactive dose taken by those working in the area. Additional lead blocks are placed outside of the vacuum chamber. The dose taken in the surrounding area (i.e., outside the lead blocks) is less than 0.5 μSv/hr.

5.3 Positron Moderators

The e^+ exit the source capsule with far too much energy to allow them to be captured via buffer-gas cooling. Therefore, the e^+ are first cooled to a low energy and moderated into a narrow energy width by passing through a solid moderating

material. A e^+ moderator can be made out of many materials; MgO powder [70], carbonized boron [71], carbonized gold [72], and copper with a sulfur layer [73], [74] have all been used with some success. The most efficient room-temperature moderator are those made of tungsten [75], [76], which have been improved upon further by cooling them to cryogenic temperatures [77]. All single-crystal metal moderators work in the same way: incident e^+ are first thermalized in the moderating material while diffusing towards the surface. A fraction of the e^+ that reach the surface are ejected into the vacuum space because the e^+ affinity for the moderating material is negative [78].

An entirely different approach to moderating e^+ is to use a frozen layer of neon (which is the approach we use here). The dynamics of e^+ inside a frozen noble gas is outlined by A.P. Mills in a process he calls the hot e^+ model [79]. Fast e^+ first lose energy in frozen Ne via the production of electron-hole pairs, excitons, and positronium atoms. Once e^+ are cooled to below the energy threshold needed for these processes, the only energy-loss mechanism is through phonon creation, which does not lead to e^+ annihilation. The maximum phonon energy in frozen Ne is very small (5.4 meV [80]). A small phonon energy means that the e^+ are more likely to reach the surface of the frozen Ne and escape before their energy falls below the e^+ work function of frozen Ne, which is positive.

5.3.1 Growing a Ne Moderator

A frozen Ne moderator slowly degrades over time, with a half life of approximately 20 hours. The degradation is caused by the adsorption of background gases onto the frozen Ne layer, thereby increasing the annihilation rate of e^+.

The procedure of growing a new frozen Ne moderator (Figure 5.4) begins with the source cryo-compressor (see Figure 5.1) turning off, thereby warming up the source and evaporating the frozen Ne layer of the previous moderator. A valve in front

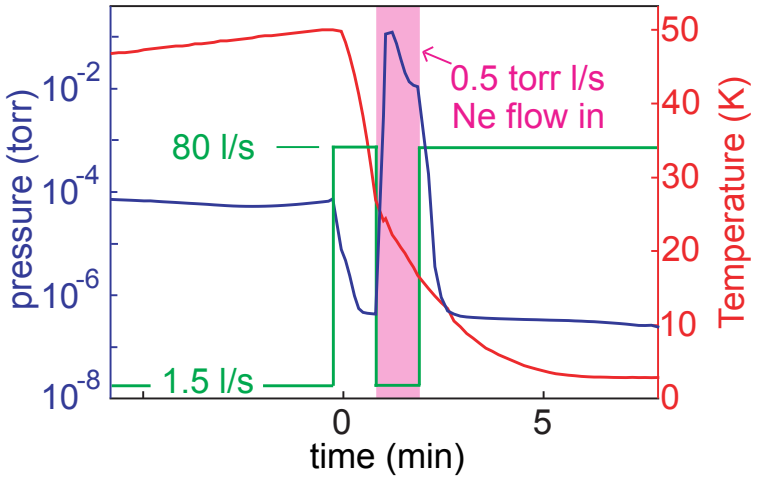

FIGURE 5.4: Parameters used for growing a Ne moderator. The temperature of the ^{22}Na source and Cu cone of Figure 5.3(a) is increased to 50 K to evaporate the previous moderator and then cooled to 3.5 K by cycling the cryogenic cold-head. When the temperature reaches 27 K, 0.5 torr l/s of Ne is admitted for 60 s. The pumping speed (not including the cryopumping onto the cold surfaces) is 1.5 l/s while the temperature increases and while Ne is being admitted, and 80 l/s otherwise. The source vacuum chamber pressure is also shown.

of the source turbopump (See Figure 5.1) is shut while the e^+ source and source mount warms. The source mount (See Figure 5.3) is allowed to warm up to 50 K to be certain that all remnants of the previous moderator are removed. Once at 50 K, the source cryo-compressor is restarted and the source mount is cooled again. The valve in front of the source turbopump is opened and the source vacuum chamber is pumped on while the source mount cools. Once the source reaches 27 K, the valve in front of the source turbo pump is closed, and 0.5 torr l/s of high-purity Ne gas (99.999%) is admitted to the source area as the temperature of the source mount decreases through 24 K — the low-pressure freezing point for Ne. The source chamber is still pumped on through the source valve (see Figure 5.3), but at a highly reduced rate — 1.5 l/s, as opposed to the 80 l/s pumping speed of the source turbo pump. Neon freezes onto the titanium window and surrounding copper cone (of Figure 5.3(a)) as the source mount continues to cool — eventually reaching 3 K. The Ne flow is stopped after 60 s, and full pumping on the source chamber resumes by opening the valve in front of the source turbo pump. Once

the residual Ne gas is pumped out of the chamber, it is possible to measure the rate of slow e^+ leaving the Ne moderator using the detection methods that will be discussed in Section 5.3.3.

5.3.2 Filtering Slow Positrons

Solenoidal electromagnets (Figure 5.3(b)) produce magnetic fields that compress the e^+ beam, as well as guide it to the drift section (Figure 5.1) before the positron accumulator. A short jog section (Figure 5.3(b)) after the source vacuum chamber is used to separate slow e^+ from the fast, unmoderated e^+. High-energy e^+ travel too fast to have their trajectories significantly changed by the magnetic field of this jog section. Slow e^+ follow the central field lines of the jog section and are guided into the drift section of Figure 5.1.

5.3.3 Slow Positron Beam Detection

A Titanium-doped Sodium Iodide crystal and photomultiplier tube (NaI+PMT) (model Crismatec Scintibloc Type: 12 S 20/3X) is positioned 1 m from either the source valve, input valve, or output valve (These valves are shown in Figure 5.1.) to measure the rate of slow e^+ that exit the jog section. The e^+ annihilate on the closed gate valve, creating a pair of 511-keV γ's. Three γ's are possible, but this occurs far less often — with a ratio of approximately 1:370 [81]. The 511-keV γ's that enter the crystal lose energy via Compton scattering, creating scintillation photons inside the crystal. A PMT (with an applied voltage of 1 kV) is fit snuggly behind the crystal. The PMT output is sent to a discriminator, the output of which is fed to a ratemeter. The discriminator sets a threshold below which photon signals are disregarded. The ratemeter determines the rate at which the PMT is detecting γ's from e^+ annihilations. γ's could potentially Compton

accumulation time (s)	accumulated e^+ ($\times 10^5$)	e^+ accumulation rate (e^+/s)
3	3.4 (5)	1.12 (16)
4.5	5.0 (2)	1.11 (10)
6	6.5 (5)	1.09 (29)
8	9.3 (3)	1.16 (24)

TABLE 5.2: e^+ accumulation rate measurements for various e^+ accumulation times. The average e^+ accumulation rate is then 1.12 (3) e^+/s.

scatter off of the metal walls of the vacuum chamber, the valve on which the e^+ annihilate, or anything else in a wide area surrounding the annihilation point and detector. This setup is useful for making relative comparisons of the slow e^+ rate after each moderator is grown.

I performed an experiment to precisely determine the rate at which slow e^+ enter the positron accumulator Penning trap. The first step in the experiment to determine this rate is to repeatedly accumulate e^+ for 3, 4.5, 6, and 8 s, which resulted in accumulations of 3.4 (5), 5.0 (2), 6.5 (5), and 9.3 (3) $\times 10^5$ e^+ (averaged over five accumulations), respectively, as measured precisely with the 3-m Faraday cup (as described in Section 4.2.1). Table 5.2 contains a summary of the e^+ accumulation data. From this data, a e^+ accumulation rate of 1.12 (16), 1.11 (10), 1.09 (29), and 1.16 (24) $\times 10^5$ e^+/s is deduced for 3, 4.5, 6, and 8 s accumulations, respectively. These rates are consistent with each other and their weighted average is 1.12 (3) $\times 10^5$ e^+/s.

The second step of the experiment is to repeatedly accumulate for even shorter times (165 accumulations that are 13-ms long and 143 accumulations that are 21-ms long), to accumulate even smaller numbers of e^+. The very short e^+ accumulations (13 ms and 21 ms) should accumulate 1456 (70) and 2352 (80) e^+, respectively, according to the linear e^+ accumulation rate of 1.12(3) $\times$ 10^5 e^+/s. The uncertainty in these numbers is due to the uncertainty of the e^+ accumulation rate and due to a 0.5-ms uncertainty in the e^+ accumulation time (with both uncertainties contributing approximately equally). These e^+ are ejected out of the

accumulator, and annihilation γ's are observed using the NaI(Ti)+PMT detector 1 m away from the closed output valve (shown in Figure 5.1) of the positron accumulator. The output from the PMT is connected directly to an oscilloscope, bypassing the discriminator and ratemeter.

Very small accumulations of e^+ are used so that the probability that more than one γ could be detected is relatively small.

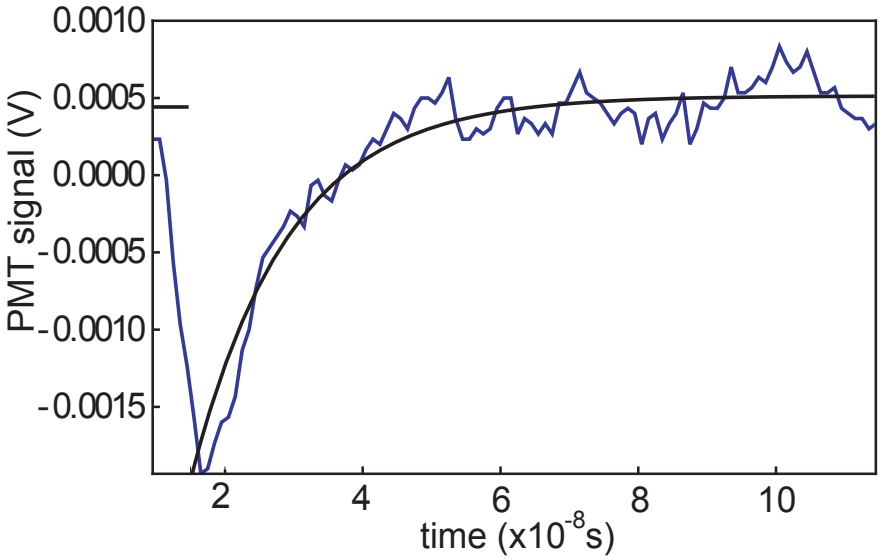

FIGURE 5.5: A single γ detected by the NaI(Ti)+PMT detector (a). The black curve is the expected exponential function $A + Be^{C(t-t_0)}$. Such fits are used in a by-eye analysis of the data to discriminate between e^+ annihilation γ's and background fluctuations.

The oscilloscope is set up to monitor only a small time window when the e^+ are expected to hit the output valve. The time window is 3.5-μs long, which makes this measurement essentially free of background counts due to cosmic rays (this point will be addressed again at the end of this section). A Mathematica program searches through the oscilloscope traces and records the magnitude of the largest voltage drop in the oscilloscope trace (as in Figure 5.5). The part of the oscilloscope trace near the voltage drop is then fit to an expected exponential curve of the form $A + Be^{C(t-t_0)}$. The oscilloscope trace is overlaid with the fit and inspected by eye to ensure that the voltage drop is due to a detected γ and not a voltage spike due to noise. The magnitudes of the voltage drops for each

accumulation time (ms)	13	21
e^+ accumulated	1456 (70)	2352 (80)
number of accumulations	165	143
accumulations with signal detected after cut criteria	71	82
fraction of accumulations with signal detected after cut criteria	0.43	0.57
signals detected (including inferred effect of signals with multiple γ's)	0.56	0.90
e^+ annihilations/inferred number of signals detected	2583 (120)	2600 (90)

TABLE 5.3: Summary of results for very short e^+ accumulations.

oscilloscope trace that is accurately fit by the exponential function are organized into a histogram, as in Figure 5.6. The large bunch at the left of this plot (voltage drop less than 1 mV) could be due to noise and are not counted, while the data to the right in the histogram (voltage drop greater than 1 mV) are assumed to be due to e^+ annihilation γ's. The results of these measurements are shown in Table 5.3. The inferred number of detections per e^+ accumulation is calculated using $-ln(1-f)$ where f is the fraction of accumulations resulting in a γ detection signal. The ln term takes into account multiple detections that could result from a single accumulation.

When accounting for multiple counts, the number of detections per accumulation is 0.56 (4) for 13-ms accumulations and 0.90 (6) for 21-ms accumulations. The reciprocal of this fraction is multiplied by the number of accumulated e^+ for each accumulation time (row 2 of Table 5.3), which gives the number of e^+ annihilations divided by the inferred number of detection signals. This ratio is 2583 (120) for the 13-ms accumulations and 2600 (90) for the 21-ms accumulations, both of which are consistent with their weighted average, which is 2593 (72).

The third step of the experiment is to allow the slow (moderated) e^+ beam to pass through the positron accumulator and annihilate on the output valve (of Figure 5.1) — the same annihilation point that is used for the very short accumulations. Five thousand 200-μs oscilloscope traces (a total of one second) are

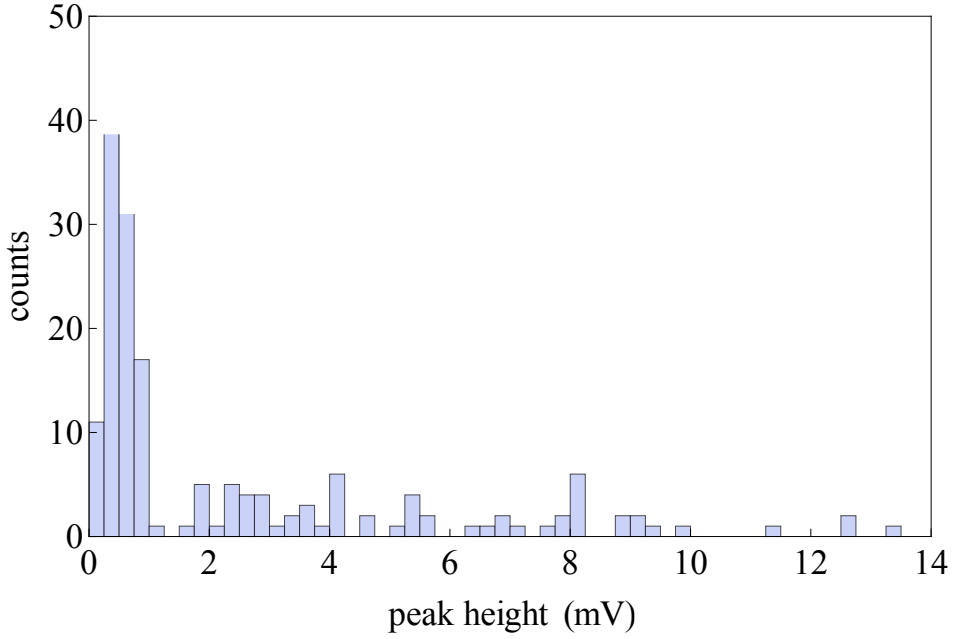

FIGURE 5.6: Histogram of the largest PMT signal in the e^+ annihilation time window for 165 consecutive 13-ms e^+ accumulations. PMT signals of more than 1 mV are attributed to e^+ annihilations.

taken as the slow e^+ beam annihilates on the output valve. A Mathematica program searches through the scope traces for voltage drops caused by e^+ annihilation γ's, using exactly the same technique as was used for the 13-ms and 21-ms accumulations. Again, following the same procedure, the voltage drops are fit to the same exponential function and are inspected by eye to discriminate between voltage drops from PMT signals and noise. Figure 5.5 shows a voltage drop that is consistent with a e^+ annihilation γ detection. Again, voltage drops of 1 mV or less are ignored. A background count rate is measured by applying the same procedure to five thousand 200-μs oscilloscope traces (a total of one second), taken with a negative bias applied to the e^+ source capsule, thereby preventing e^+ from leaving the source. The result (shown in Figure 5.7) is that 1233 detection signals meet the exponential-fit function and voltage-drop criteria when e^+ are exitting the moderator surface, and 166 when the e^+ are prevented from leaving the moderator surface. The inferred background-subtracted detection rate is thus 1067 (37) s^{-1}.

The background detection rate of 166 s^{-1} can now be applied to the time window used in the very short accumulations. The number of background counts that can be expected in a 3.5-μs-long time window is less than a part in 10^3, validating the background-free assumption.

The background-subtracted detection rate of 1067 (37) s^{-1}, along with the ratio 2693 (72) determined above, leads to a measured slow e^+ rate of 2.75 (27)$\times 10^6$ e^+/s. This rate, when normalized to the strength of the e^+ source (which was 12 mCi), gives 2.30(23) $\times$ 10^5 $e^+/s/mCi$. The uncertainty in these slow e^+ rates is larger than the measurement uncertainty because other experimental factors, such as the uncertainty in the 3-m Faraday cup calibration, are taken into account. This is the most precise determination of the slow e^+ rate in the ATRAP positron accumulator.

5.3.4 Moderator Optimization

The time at which the Ne is admitted, Ne flow rate, and Ne flow duration are chosen to optimize the moderator efficiency (i.e., they are chosen to achieve the largest slow e^+ rate). Figure 5.8 and Figure 5.9 show two of the results of experimenting with different Ne flow rates and durations. The optimal moderator growth parameters are found to be a Ne flow of approximately 0.5 torr l/s applied when the source reaches 27 K, for a duration of approximately 1.2 minutes.

Increasing the efficiency with which the frozen Ne moderator converts fast e^+ to slow e^+ increases the normalized slow e^+ rate. With an optimized Ne moderator, the final slow e^+ rate, reported in Table 5.4, is 2.60(26) $\times$ 10^5 $e^+/s/mCi$.

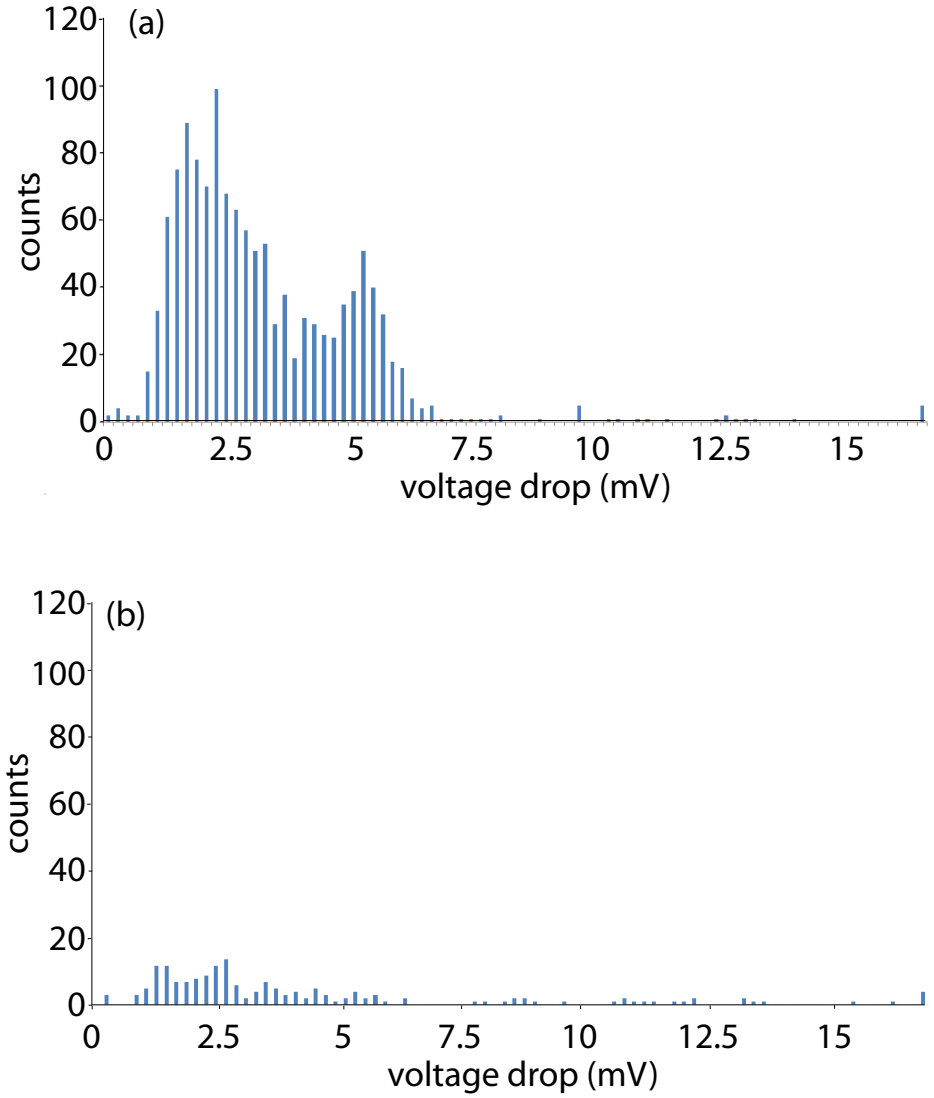

FIGURE 5.7: Histograms of voltage drop measurements when e^+ annihilate on the output valve (a) and when e^+ are prevented from exitting the moderator surface (b). Only voltage drops that are accurately fit by the expected exponential function $A + Be^{C(t-t_0)}$ are shown in these histograms, and, of these, only voltage drops greater than 1 mV are used to calculate the γ detection rate.

5.3.5 Moderated Positron Beam Properties

The efficiency with which a frozen Ne moderator converts fast e^+ into slow e^+ is its most important property. There are two measures that are used when discussing the efficiency of a frozen Ne moderator. The ratio of the number of slow e^+ that exit the moderator surface to the number of high energy e^+ that exit the thin titanium window is called the moderator efficiency. This measure ignores the

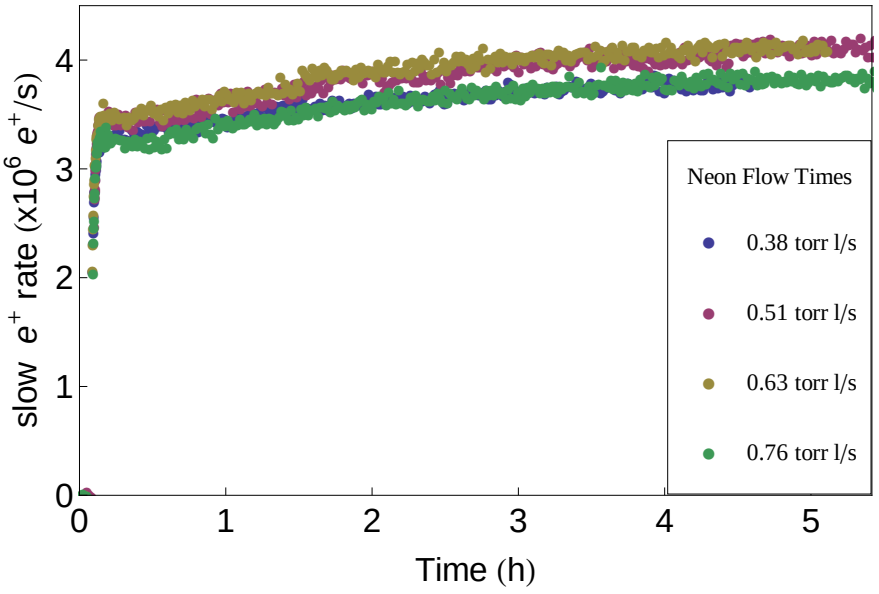

FIGURE 5.8: The observed slow e^+ rate of moderated e^+ versus time after the creation of a new Ne moderator for several Ne flow rates for 1.2 minutes of Ne flow.

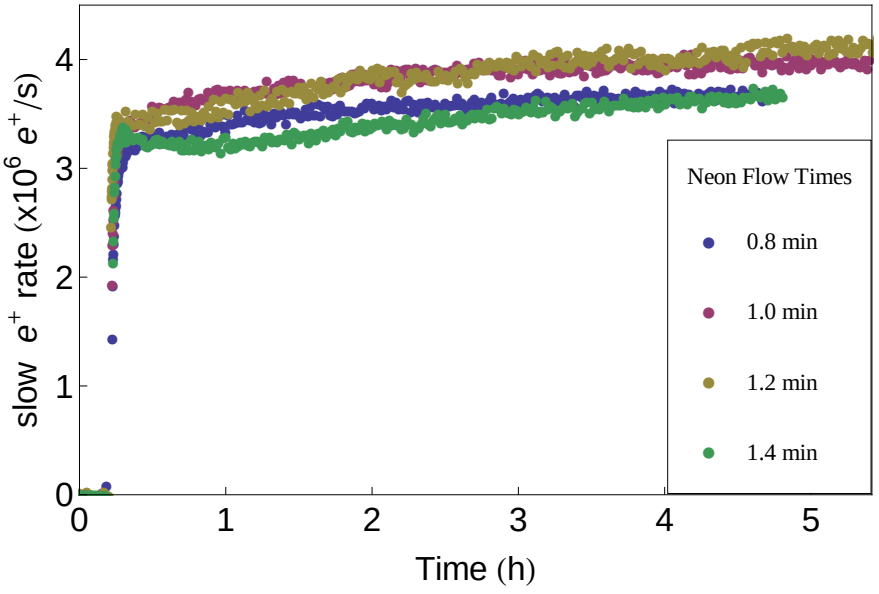

FIGURE 5.9: The observed slow e^+ rate of moderated e^+ versus time after the creation of a new Ne moderator for several Ne flow times for a Ne flow rate of 0.51 torr l/s.

parameter	Ne moderator
e^+ from ^{22}Na	3.35×10^7 e^+/s/mCi
e^+ from source capsule	9.0×10^6 e^+/s/mCi
e^+ from moderator	$2.60(26) \times 10^5$ e^+/s/mCi
efficiency (moderator and source)	0.78 (7)%
efficiency (moderator)	2.9 (3)%
energy width (FWHM)	3.4 eV

TABLE 5.4: ^{22}Na source and frozen Ne moderator parameters

source efficiency. The second measure is the moderated source efficiency, which is the ratio of the moderated e^+ number to the total number of e^+ emitted by the source material. This measure includes the source efficiency. We normally discuss only the moderator efficiency, since we have no control over the structure of the source and titanium enclosure, which determines the source efficiency. The efficiency of our Ne moderator is summarized in Table 5.4.

In addition to efficiently slowing the e^+, an ideal moderator will emit a monoenergtic beam of slow e^+. The energy width of our slow e^+ beam is measured by having the slow e^+ beam pass through the positron accumulator and using the positron accumulator electrodes (of Figure 5.1) to produce a blocking potential. The output valve (Figure 5.1) of the positron accumulator is closed and γ's from e^+ annihilations on this valve are detected. The signal is monitored as the blocking potential is increased and low-energy e^+ are unable to pass (Figure 5.10(a)). The data are fit and the derivative of the fit curve is used to determine the energy width of the e^+ beam (Figure 5.10(b)). Under normal operating conditions, the slow e^+ energy width is 3.4 eV. Operating with a smaller bias applied to the source capsule reduces the energy width to 1.7 eV, but results in fewer slow e^+. 3.4 eV is not as low an energy width as others have achieved with Ne moderators [82], but we choose to optimize for moderator efficiency rather than the energy width.

A slow e^+ beam produced using a metal foil moderator typically has a narrower energy distribution than a e^+ beam produced with a frozen Ne moderator. The

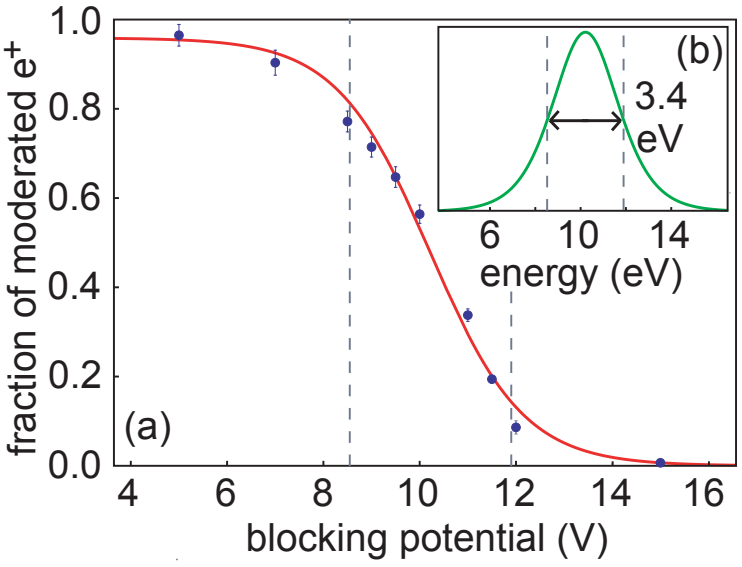

FIGURE 5.10: A 3.4-eV energy width (FWHM) is measured using a blocking potential in the accumulator electrode stack and 11-eV bias voltage at the ^{22}Na source. The derivative of the fit curve is shown in the inset

energy width of e^+ beams produced using a carbonized boron moderator can be as low as 0.15 eV [71]. Even though the e^+ beam from a frozen Ne moderator has a broader energy distribution, the beam itself is much more intense. The most efficient of the metal moderators is the cryogenic tungsten moderator [77] but it is a factor of 20 less efficient than the frozen Ne moderator used in this work.

Frozen Ne, Ar, Kr, and Xe have all been studied as potential moderator materials [82]. It is found that frozen Ne provides the highest efficiency as well as the most narrow e^+ energy width. Our geometry, in which a cone-shaped moderator is included, is found to be the most efficient for frozen Ne moderation of e^+ [83].

5.4 Drift Section

Slow moderated e^+ enter the drift section (shown in Figure 5.1, and, in more detail, in Figure 5.11). The purpose of the drift section is to isolate the pristine vacuum conditions of the source chamber from the high N_2 pressure of the positron

accumulator. The N_2 would badly pollute the frozen Ne moderator if the two sections were not adequately isolated. A polluted moderator emits far fewer e^+, and the higher pressure would annihilate e^+ before they make it to the positron accumulator. The pressure in the accumulator region is as high as 0.01 torr, while the source chamber pressure is typically 1×10^{-8} torr. Isolation between the systems is provided by an 80 l/s turbo pump (ATP80 by Alcatel) with a 20-cm-long, 1.2-cm-diameter pumping restriction on either side, as shown in Figure 5.11. The drift section pressure — measured at the cross in the center of the drift section (Figure 5.11) — increases from 1×10^{-7} torr to 1×10^{-6} torr upon opening the input valve (at the end of the drift section, as shown in Figure 5.1) of the positron accumulator, whereas the source chamber pressure changes by less than 1×10^{-9} torr when both the source valve and input valves of Figure 5.1 are opened. The vacuum isolation provided by the drift section is deemed adequate because no loss in the moderated e^+ rate is seen when these valves are opened.

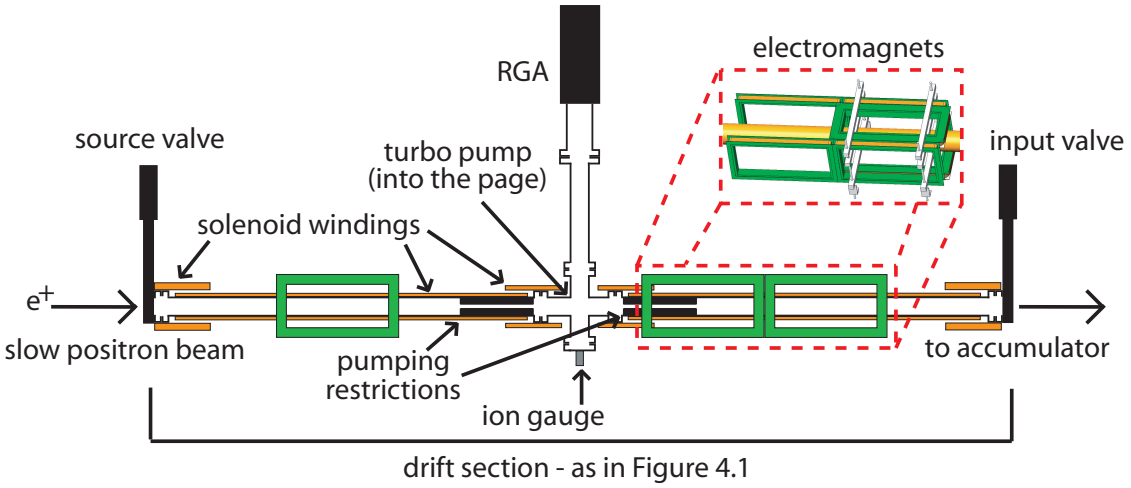

FIGURE 5.11: Schematic of the drift section between the ^{22}Na source and the positron accumulator. An angled close-up of an electromagnet winding is shown.

Solenoidal and rectangular electromagnets are used to magnetically guide e^+ through the drift section (Figure 5.11). Solenoid coils are wound directly onto the vacuum tubes of the drift section to create an axial magnetic field line for the moderated e^+ beam to follow. Pairs of rectangular electromagnets (oriented both horizontally

and vertically, as shown in Figure 5.11) are used to correct for external magnetic fields that are perpendicular to the vacuum-tube axis. These fields arise from the earth's field, from the fringing field from the ATRAP 1-T superconducting magnet, and from other magnets in the AD. Extra coils are placed over the flanges of the cross in the center of Figure 5.11 to keep the moderated e^+ beam compressed as it passes through the center of the cross, where axial solenoid coils cannot be wound. NaI(Ti) + PMT detectors positioned at the source valve and input valve can be used to monitor the moderated e^+ rate, and confirm that there is no detectable e^+ loss in the drift section.

A residual gas analyzer (RGA) is situated near the center of the drift section, as shown in Figure 5.11. The RGA is used to detect vacuum leaks and impurities that could lead to poorer e^+ moderation and accumulation. The cross section for e^+ annihilation on hydrocarbon chains scales as N^4, where N is the number of atoms in the chain [84]. Typical pump oil is made from long hydrocarbon chains of the form C_nH_{2n} with n between 20 and 40. Therefore, trace amounts of pump oil, vacuum grease, or even organic grease from fingerprints, can prohibit e^+ accumulation. Every effort is made to keep the vacuum space oil-free and leak tight.

5.5 Buffer-Gas Accumulator

The positron accumulator (Figure 5.12) consists of a room-temperature Penning trap with N_2 gas introduced to slow the incident e^+. The accumulator consists of a stack of electrodes in 3 stages, as shown in Figure 5.12.

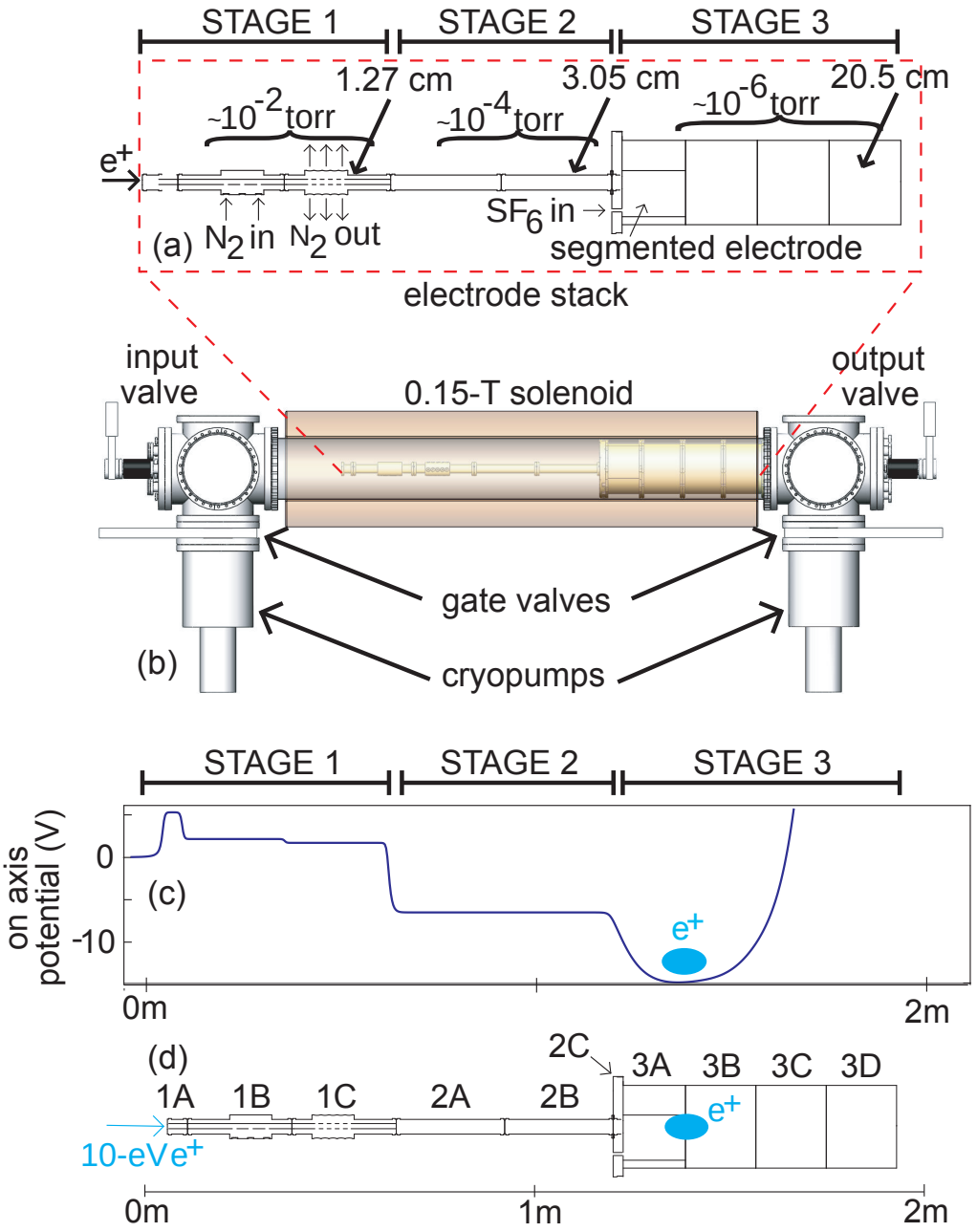

FIGURE 5.12: The Penning trap of the positron accumulator. (a) schematic of the Penning trap showing the gas inlets and outlets and pressures and diameters of the three stages of the Penning trap. (b) the 0.15-T, room temperature solenoid and electrode stack of the positron accumulator. Vacuum is maintained by cryopumps on either side of the Penning trap. (c) The electrode stack potentials used to accumulate e^+ and (d) the electrode stack with naming convention.

5.5.1 Buffer-Gas Accumulator Penning Trap

The Penning trap of the gas buffer accumulator consists of a 2-m-long, 25-cm-bore copper solenoid and 10 gold-plated aluminum electrodes, as shown in Figure 5.12(a). Instead of thick wire, the solenoid windings are made of square copper tube to allow efficient water cooling of the solenoid. Cooling water flows through the tube to dissipate the 15 kW of heat produced when the solenoid is operated at 400 A. The copper solenoid provides a highly uniform, axial magnetic field. Five power supplies (TCR 5-kW supplies from EMI) are used in series to provide 400 A (requiring 38 V) to produce a field of 0.15 T. The solenoid was designed by Dr. Matthew George and built by New England Technicoil. The axial field is specified to vary by less than 0.0015% over the central 1.5 m of the solenoid.

The electrode stack provides the axial confinement of e^+. The on-axis potential used to accumulate e^+ is shown in Figure 5.12(c). Each stage (stage 1-3) has a successively deeper potential well for e^+ trapping. The potential for each electrode is provided by a calibrated biasdac and 'SuperElvis' pair. The biasdac is a precise, programmable voltage source and the 'SuperElvis' is a highly filtered amplifier specially designed and built for this purpose by the Harvard electronics shop. An electric potential can be applied to each electrode individually, with a precision of approximately 0.1% within the range of voltages used to accumulate e^+.

N_2 is admitted to the first stage of the accumulator (which consists of hollow cylindrical electrodes that have a 1.27-cm inner diameter) through holes drilled through electrode 1B, as shown in Figure 5.12(a). A convectron gauge monitors the pressure directly at that electrode. The N_2 is pumped out through the open ends of the electrode stack, as well as through 20 holes drilled into electrode 1C of Figure 5.12(a). The N_2 pressure in the first stage is approximately 10^{-2} torr. The inner diameter of the second-stage electrodes is 3.05 cm. The N_2 pressure inside of these electrodes is approximately 10^{-4} torr. The inner diameter of the third

stage is 20.5 cm — the largest possible diameter within our solenoid — creating the best possible vacuum. This stage is effectively pumped by one of the two SHI Marathon CP12 large vacuum croypumps (See Figure 5.12(b)) and has an N_2 pressure of approximately 10^{-6} torr.

5.5.2 N_2 as a Buffer Gas

The incoming moderated e^+ require some mechanism through which to lose energy and become trapped in the potential well of the electrode stack. N_2 is chosen as a buffer gas to be this energy-loss mechanism, since collisions with N_2 molecules cause electronic excitations of the N_2, and, for a range of e^+ energies, the electronic excitation cross section is far greater than that of positronium formation [85]. This range for electronic excitation, centered at approximately 11 eV, is wide enough [63] to make the 3.4-eV energy width of the e^+ acceptable.

With the moderator bias voltage set to approximately +10 V, 10-eV e^+ are created, and these efficiently excite the N_2 in the high-pressure region (stage 1) of the electrode stack (Figure 5.1), losing 9 eV of kinetic energy per interaction [61]. Most e^+ that inelastically scatter off of a N_2 molecule lose enough energy on a round trip pass through the accumulator to become trapped between the potential barriers on electrodes 1A and 3C in Figure 5.12(c) (stages 1, 2, and 3). As the e^+ travel back and forth through the length of the electrode stack, they will scatter off of another N_2 molecule and lose another 9 eV, trapping the e^+ between electrode 2A and 3C (stage 2), where the N_2 pressure is lower (see Figure 5.12(c)). A third N_2 collision traps the e^+ in the potential well created on electrodes 3A and 3B in Figure 5.12(c) (stage 3), where the pressure is approximately 10^{-6} torr. This lower pressure is necessary to avoid e^+ annihilation while the e^+ accumulate in this stage of the positron accumulator.

5.5.3 Rotating Electric Field

As e^+ are accumulated in stage 3 of the positron accumulator, the growing e^+ plasma is subject to many sources of radial expansion. Elastic scattering from N_2 molecules can cause radial walk-off, and small misalignments between the electrode stack and the solenoid can apply an effective torque on the plasma, breaking the angular momentum conservation, and allowing the mean radius of the plasma to increase.

A rotating electric field is used to decrease the mean radius of a plasma, allowing for increased total number of accumulated e^+ and more efficient transport of the plasma to the cryogenic Penning trap. The rotating electric field, often called a rotating wall, was first demonstrated to work on e^- through the excitation of Trivelpiece-Gould (TG) modes that rotate faster than the plasma [86]. That work was done in a 4-T magnet, so the plasma heating caused by the rotating-wall drive was counteracted by the strong cyclotron cooling. Positron accumulators typically use much smaller magnetic fields — well below the threshold for useful cyclotron cooling. Surko *et al* demonstrated that elastic collisions with a neutral buffer gas could cool the e^+ plasma without large annihilations [62]. SF_6 — typically 3×10^{-8} torr — is admitted through a small hole in electrode 2C (Figure 5.12(a)).

The positron accumulator has electrode 3A (See Figure 5.12(a)) azimuthally segmented into quadrants for the application of the rotating electric field, as in Figure 5.13. A custom-built multichannel synthesizer produces the voltage $V = V_0\cos(\omega_{RW}t - \frac{\pi}{2}k)$ which is applied to the k^{th} segment ($k = 1, 2, 3, 4$). The applied voltages are shown in Figure 5.13. The rotating-wall drive in the positron accumulator is applied with a typical drive frequency 750 kHz and a typical drive amplitude of 7 V peak-to-peak.

Figure 5.14(a) shows the accumulated e^+ count as a function of rotating-wall frequency. The total number of accumulated e^+ peaks at 750 kHz, then decreases

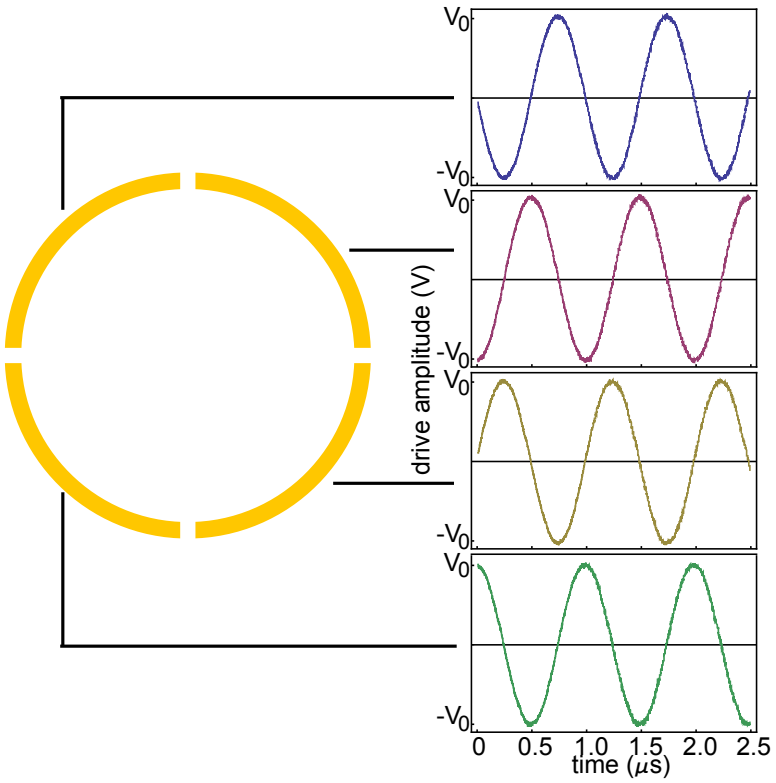

FIGURE 5.13: Sinusoidal voltages which are $\pi/4$ out of phase are applied to four segments of a segmented electrode to produce a rotating electric field that can change the radius of a non-neutral plasma.

when higher drive frequencies are used. A decrease at higher frequencies has been seen by the Surko group and has been attributed to transmission-line effects in the rotating-wall circuit that lead to an unbalanced drive in the segmented electrodes, which causes increased plasma heating [87]. It is unclear if this same problem affects the ATRAP positron accumulator and causes the drop-off at higher frequencies in Figure 5.14(a).

Figure 5.14(b) shows the accumulated e^+ count as a function of rotating-wall amplitude. The e^+ accumulation rate increases as the rotating-wall amplitude increases, then levels off before a very steep drop when using a 9 V peak-to-peak drive. Large-amplitude drives apply more torque to the plasma and thus, more heat. For large drive amplitudes, the SF_6 does not provide sufficient cooling.

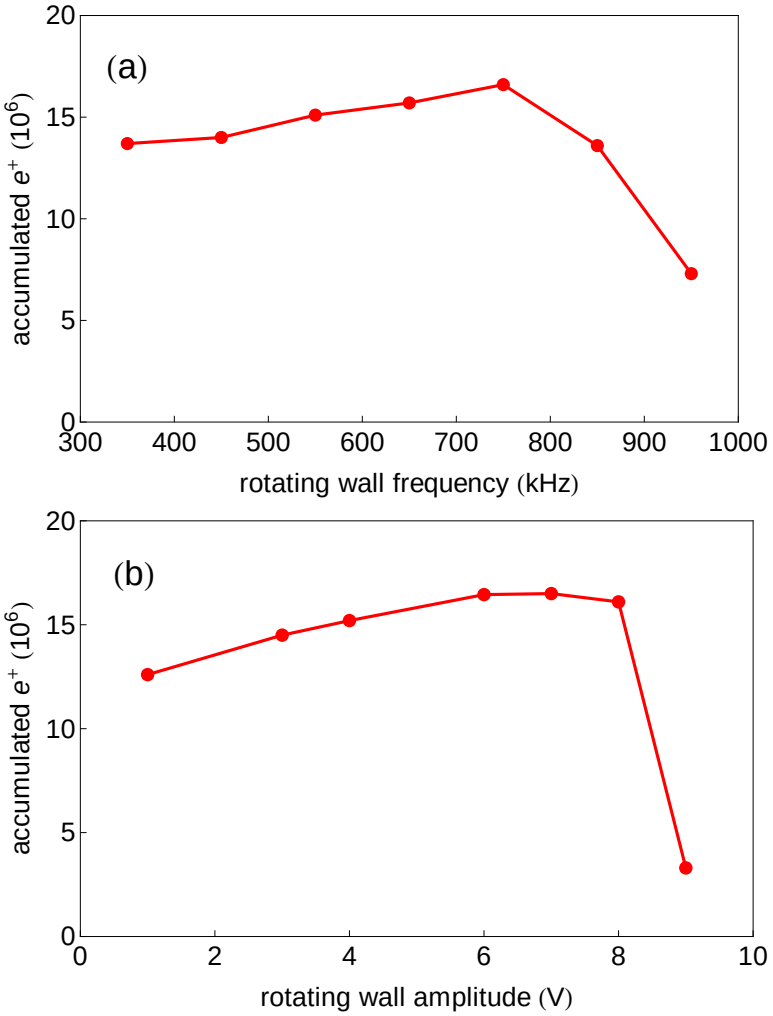

FIGURE 5.14: (a) Number of e^+ accumulated as a function of rotating-wall frequency, with the amplitude held constant at 7 V. (b) e^+ accumulation as a function of rotating wall amplitude, with the frequency held constant at 750 kHz.

5.5.4 Positron Accumulation

A Faraday cup is used to charge-count the ejected e^+, as described in Section 4.2.1. Figure 5.15 shows the number of e^+ accumulated as a function of accumulation time. The figure shows that e^+ accumulation depends linearly on the accumulation time, up until accumulation times of approximately 20 s, after which the accumulation rate decreases. The potential well that holds the accumulating e^+ (Figure 5.12(c)) is large enough to hold hundreds of millions of e^+, indicating that

annihilation or radial loss mechanisms are to blame for the end to linear e^+ accumulation. Positrons can be lost due to radial migration to larger radii in the room-temperature Penning trap, which results from off-axis components of the magnetic field. The large-bore superconducting solenoid of the cryogenic Penning trap and the time-varying components from AD Ring magnets are the main sources of transverse magnetic field gradients. Radial migration also results from momentum-changing collisions between the trapped e^+ and residual gas atoms. The required N_2 gas makes this process unavoidable.

Positron accumulation efficiency is not the only factor to consider when choosing the duration of positron accumulation. The ambient magnetic field in the AD changes with the cycling of the AD magnets. Because of these large AD magnetic fields, e^+ cannot be efficiently transferred from the positron accumulator to the 1-T ATRAP cryogenic Penning trap during the first 30 s of the AD cycle. Thus, the first e^+ transfer can take place about 30 s after the start of the AD cycle, which is typically 90 s long. Three 30-s accumulations are transferred to the ATRAP cryogenic Penning trap during each AD cycle.

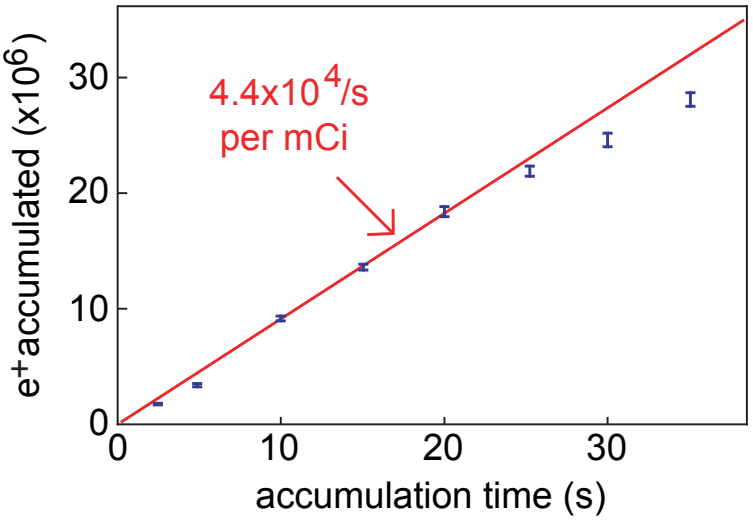

FIGURE 5.15: Positron accumulation with a linear fit of the data between 10 s and 20 s. A rate of 4.4×10^4 e^+/s/mCi is achieved.

As shown in Figure 5.15, a peak loading rate for the positron accumulator is 4.4×10^4 e^+/s/mCi, corresponding to approximately 17% of the moderated e^+.

Once the 30-s accumulation time is over, the moderated e^+ beam is blocked by making a potential wall at electrode 1A (Figure 5.12(c)) and the potential well containing the accumulated e^+ is shifted (Figure 5.16) to prepare the e^+ for ejection into the e^+ transfer guide. During this process, the e^+ are gently shifted (Figure 5.16(c) to (h)) away from electrode 3A and towards electrode 3C (Figure 5.12(d)), which is equipped with an Avtec saturated switch. The e^+ well is raised (Figure 5.16(i) to (j)) to give the soon-to-be-ejected e^+ the desired energy. At the final step (Figure 5.16(j)), the saturated switch is triggered by a DG535 pulse generator and a 20-V pulse ejects the e^+ from the accumulator by suddenly raising the potential, as indicated by the dashed line in Figure 5.16(j).

5.5.5 Positron Ejection Energy Distribution

The energy spread of a room-temperature plasma corresponds to $\frac{1}{2}k_BT$ per degree of freedom, which would lead to an axial energy spread of 0.025 eV. In reality, radial variation in the potential well depth across the plasma width during e^+ ejection, collective plasma effects, and electrical noise on the electrodes increase this energy width [88]. The energy width of the e^+ ejection from the positron accumulator is measured using a blocking voltage applied to electrodes in the upper half of the cryogenic Penning trap electrode stack (Figure 5.17). This is the same technique used to measure the energy width of the moderated e^+ beam as it enters the positron accumulator (Section 5.3). The e^+ ejection from the positron accumulator has an energy width of 6.6 eV FWHM.

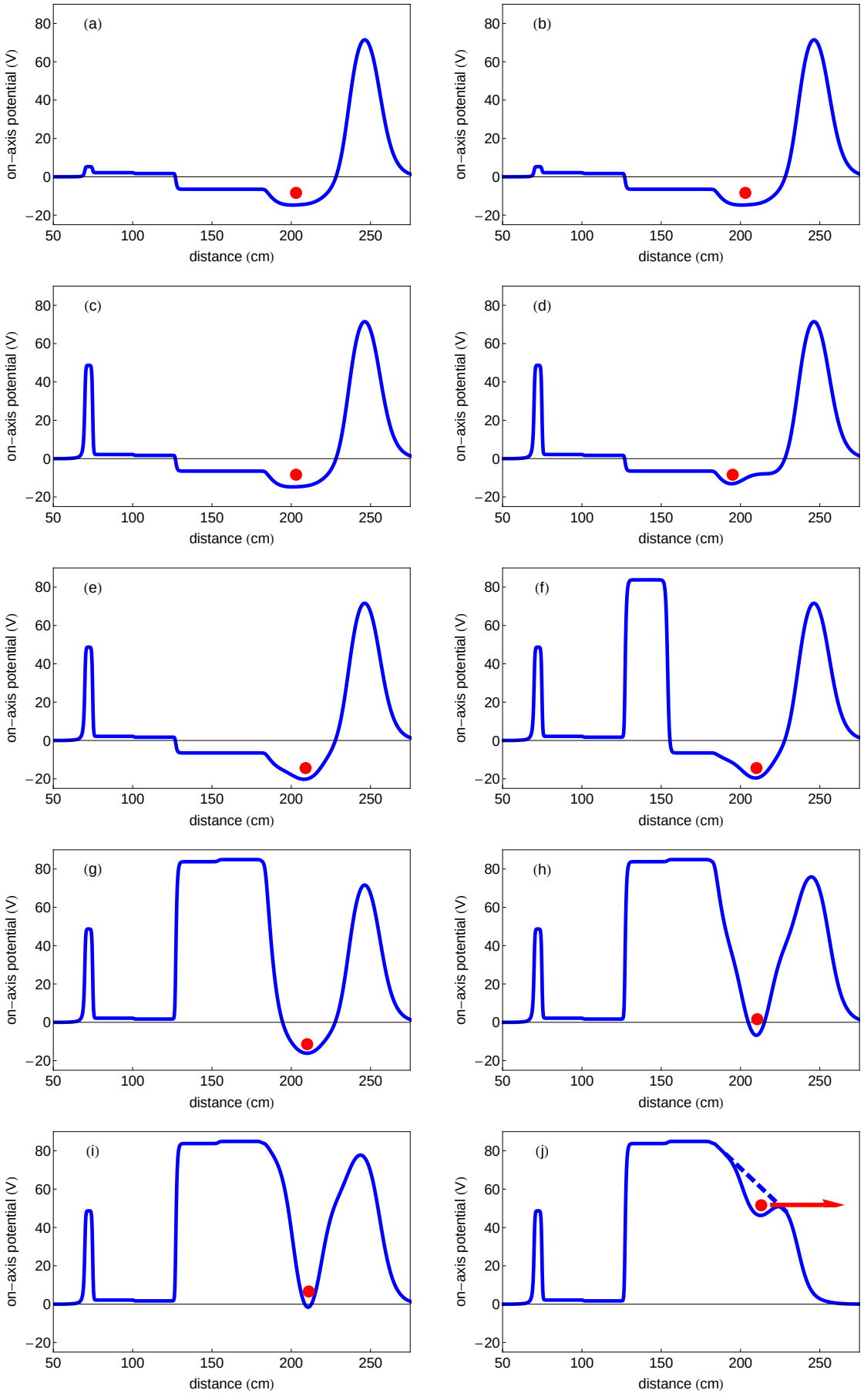

FIGURE 5.16: The on-axis potentials used to accumulate and eject e^+ clouds (marked as red disks). The Avtec pulser is triggered during a 1-s wait on step (j). The distance scale of the x-axis corresponds to the scale of Figure 5.1. Details are given in the text.

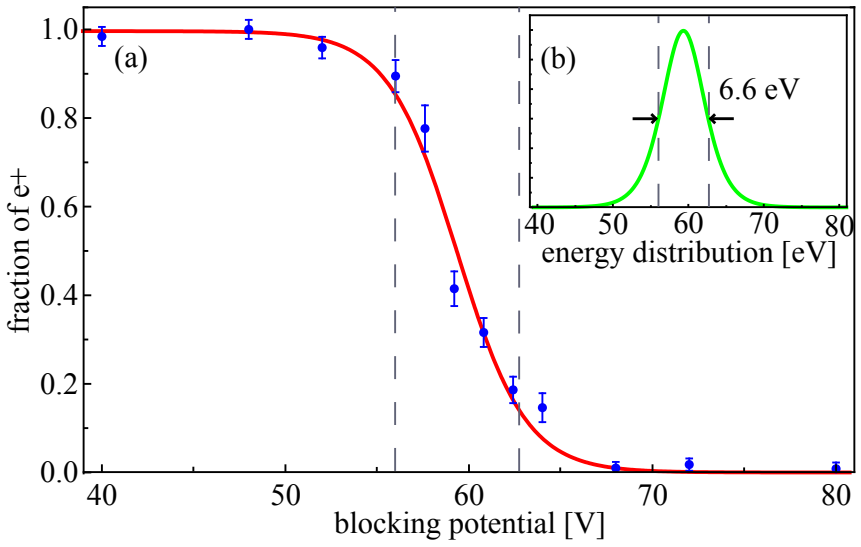

FIGURE 5.17: The fraction of e^+ from the positron accumulator that overcome a potential barrier in the cryogenic Penning trap (a). The inset shows the derivative of the fit curve and a measurement of the e^+ energy width (b).

Chapter 6

Magnetic Positron Transfer Guide

Ideally, the positron accumulator and cryogenic Penning trap for $\overline{\mathrm{H}}$ studies would be co-axial. This is not the case for ATRAP, as shown in Figure 6.1. The cryogenic Penning trap is, by necessity, oriented vertically above the AD $\bar{\mathrm{p}}$ ejection line. The positron accumulator (including the source vacuum chamber, drift section, and Penning trap) is more than 6 m in length, which would have it extending into the roof of the AD Hall if ATRAP attempted a co-axial alignment. Instead, the positron accumulator is positioned horizontally. It is located as near as possible to the cryogenic Penning trap but still far enough away from the 1-T superconducting solenoid so that the fringing field is not strong enough to detrimentally affect e^+ accumulation.

The e^+ transfer guide (Figure 6.1) [89] is used to move the e^+ over the 8-m distance between the positron accumulator and the cryogenic Penning trap. The e^+ transfer guide uses a series of 70 electromagnets to connect the axial magnetic field lines of the positron accumulator horizontal solenoid to the central fringing field lines of the vertical 1-T superconducting solenoid of the cryogenic Penning trap.

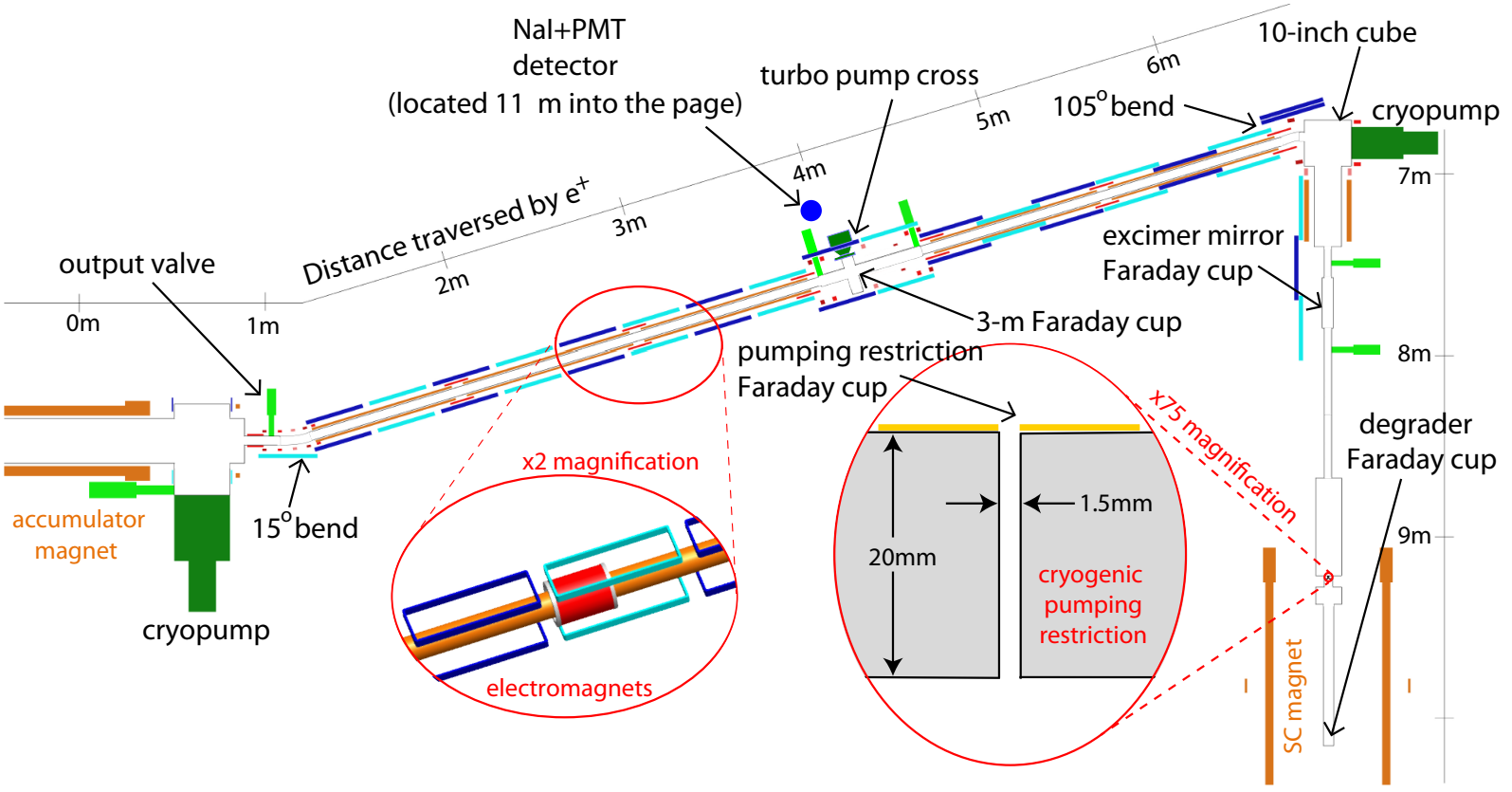

FIGURE 6.1: The ATRAP e^+ transfer guide. 70 electromagnets guide e^+ from the positron accumulator to the cryogenic pumping restriction. Positrons then follow the central field lines of the 1-T superconducting solenoid into the cryogenic Penning trap.

The e^+ transfer guide also acts as a pumping restriction to prevent the high pressure of the positron accumulator (10^{-2} torr of N_2) from contaminating the extremely-high-vacuum of the cryogenic Penning trap experiment space ($< 2 \times 10^{-16}$ torr).

6.1 Magnetic Field in the Positron Transfer Guide

Figure 6.2 shows the amplitude of the axial field in the e^+ transfer guide of Figure 6.1. Positrons leave the 0.15-T field of the accumulator (0.25 m in Figures 6.1 and 6.2) and enter the 0.02-T field of the e^+ transfer guide. The magnetic field of the e^+ transfer guide is not perfectly homogenous. Discontinuities occur at the ends of the 1-m vacuum tubes (e.g., at 2.1 m in Figures 6.1 and 6.2), where extra solenoids are placed over the flanges. The large inhomogeneous area just after the 4-m mark is due to the cross with gate valves on either side that connects to the e^+ transfer guide turbo pump and houses the 3-m Faraday cup. Another inhomogeneous area follows at the 7-m mark of Figure 6.1 where the e^+ make a 105° bend inside of a 10-inch cube vacuum chamber. Just before the 8-m mark, the field steadily increases as the e^+ enter the central field of the 1-T superconducting solenoid.

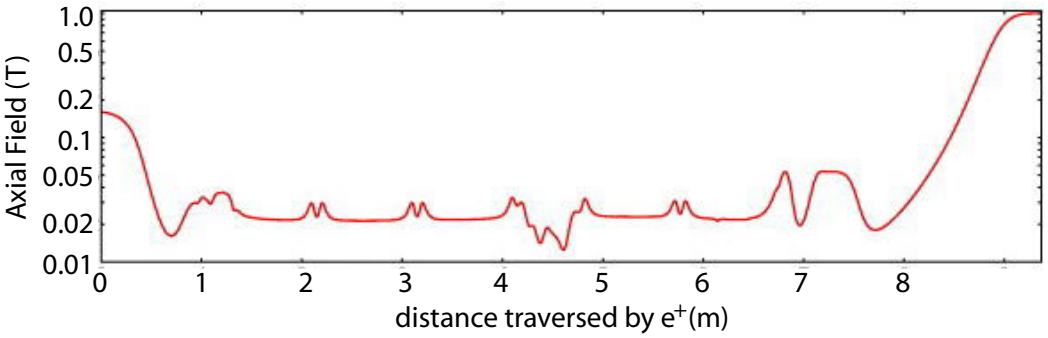

FIGURE 6.2: Modelled axial magnetic field inside the e^+ transfer guide. Figure from [89]. The distance scale of the x-axis corresponds to the scale of Figure 6.1.

The modeled field of Figure 6.2 includes the magnetic fields from the positron accumulator, e^+ transfer guide elements, and the 1-T superconducting solenoid, but does not take into account smaller fringing fields emanating from the superconducting solenoids of other groups in the AD Hall or time-dependent fringing fields from components of the AD Ring.

6.2 Detectors in the Guide

An array of detectors is used to ensure that e^+ are accumulating as efficiently as possible and that these e^+ are transferred to the cryogenic Penning trap without losses in the e^+ transfer guide. Positions of the various detectors are shown in Figure 6.1

6.2.1 Scintillating Detectors

When the magnetic fields of the e^+ transfer guide are not set properly, e^+ follow magnetic field lines into the vacuum-chamber walls and annihilate. A scintillating detector (NaI(Ti)+PMT detector (Crismatec Scintibloc Type: 12 S 20/3X)) is the principal diagnostic tool used to ensure that e^+ efficiently traverse the e^+ transfer guide. This scintillating detector is positioned 11 m away from the e^+ transfer guide (shown in Figure 6.1), at a position which allows the entire e^+ transfer guide to be approximately equidistant from the detector. Because the e^+ are ejected suddenly from the positron accumulator, and are all travelling at approximately the same speed, and because the e^+ travel much more slowly than the annihilation γ's that are detected, the timing of the signal from the scintillating detector can be used to determine where in the e^+ transfer guide the e^+ are annihilating. If e^+ annihilations are seen at some point in the e^+ transfer guide, the magnetic field near this annihilation point can then be adjusted, allowing e^+ to be steered

further down the e^+ transfer guide. Figure 6.3 shows such annihilation signals at the output valve at the 1-m mark of Figure 6.1, 3-m Faraday cup (4-m mark of Figure 6.1), and excimer-mirror Faraday cup (7.7-m mark of Figure 6.1). Positrons are ejected from the positron accumulator with an energy of approximately 60 eV, which corresponds to a speed of 4.6×10^6 m/s. One would expect to see annihilation signals at 0.22, 0.87, and 1.65 μs for the three annihilation positions chosen. The measurements in Figure 6.3 agree to within 10% of these expected values.

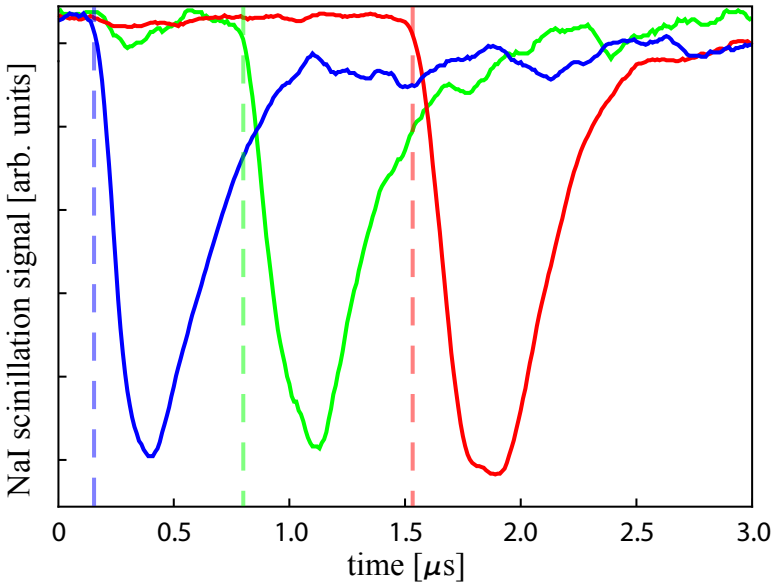

FIGURE 6.3: NaI+PMT detector signals from 2×10^7 e^+ annihilating at the 1-m (blue), 4-m (green) and 7.7-m (red) marks in Figure 6.1.

6.2.2 Faraday Cups

Quantitative studies of e^+ clouds are done using retractable Faraday cups positioned throughout the e^+ transfer guide (Figure 6.1). When a cloud of e^+ is pulsed onto a Faraday-cup surface, the induced positive charge can be measured using the charge-sensitive preamplifiers discussed in detail in Section 4.2.

Positrons are easily transferred between the positron accumulator and the 3-m Faraday cup in Figure 6.1 with very nearly 100% efficiency, and so this Faraday cup is used to measure the efficiency of the accumulating process. The next retractable

Faraday cup (the excimer-mirror Faraday cup in Figure 6.1) is used to count e^+ after the 105° bend. The excimer-mirror Faraday cup is segmented into four quadrants that surround a central 5-mm-diameter Faraday cup. The magnetic field at the end of the e^+ transfer guide can be set such that very nearly the entire e^+ cloud annihilates on the central Faraday cup, putting an upper limit of 5 mm on the e^+ cloud diameter. Measurements at the excimer-mirror Faraday cup, along with the scintillating detector signals, are used to ensure that nearly 100% of the e^+ are transferred around the 105° bend.

A concern when entering the magnetic field of the 1-T superconducting solenoid is that the larger field can act as a magnetic mirror and repel e^+ from the cryogenic Penning trap. The total energy of the e^+ and magnetic moment of the cyclotron motion ($\mu = mv_\perp^2/2B$) remain constant as the e^+ enter the 1-T superconducting solenoid. To conserve μ, as the field amplitude B increases, the perpendicular velocity component ($v_\perp$) also increases. As a result, the velocity component parallel to the magnetic field ($v_\parallel$) decreases, since the total energy is conserved. If $v_\parallel$ is reduced to zero through this process, the e^+ is repelled from entering the 1-T field. A Faraday cup split into four segments surrounds the 1.5-mm-diameter cryogenic pumping restriction in Figure 6.1 within the 1-T field of the 1-T superconducting solenoid. Signals from this Faraday-cup assembly are used to center the translatable XY stage (Section 3.1.4) and steer e^+ through the cryogenic pumping restriction. The number of e^+ measured at these Faraday cups (with the e^+ steered away from the 1.5-mm hole) matches the number of e^+ measured at the excimer-mirror and 3-m Faraday cups, indicating that nearly 100% of the accumulated e^+ enter the field of the 1-T superconducting solenoid — indicating that magnetic mirroring is not an issue for our e^+.

At the bottom of the cryogenic Penning trap electrode stack, the degrader (DEG in Figure 3.4) is connected to a charge-sensitive amplifier and can also be used as a Faraday cup (degrader Faraday cup in Figure 6.1) to measure the number of

e^+ that reach the cryogenic Penning trap. The signal measured at the degrader is typically 60% of what is measured on the earlier Faraday cups, indicating that annihilation in the 1.5-mm-diameter cryogenic pumping restriction is the dominant loss mechanism. This problem would be easily solved by increasing the diameter of the pumping restriction, but at the possible cost of increasing the number of background gas atoms and molecules in the experiment space of the cryogenic Penning trap.

6.3 Vacuum

A pristine vacuum in the cryogenic Penning trap is critical for achieving long hold times for antimatter particles and atoms. Background gas in the cryogenic Penning trap can collide with the trapped antimatter and result in annihilation or antimatter plasma instability through elastic collisions.

Figure 6.1 shows the location of vacuum pumps in the e^+ transfer guide. The bulk of the N_2 and SF_6 in the positron accumulator is removed by the 3600-l/s cryopumps in the accumulator region, bringing the pressure at the final stage of the positron accumulator to approximately 10^{-6} torr. An 80-l/s turbo pump is located at the 4-m mark of the e^+ transfer guide in Figure 6.1. An ion gauge measures the pressure at this location. The vacuum pressure when the output valve of the accumulator (Figure 6.1) is closed is 1.2×10^{-7} torr, which increases by only 4×10^{-8} torr when the output valve of the accumulator is opened. A 1500 l/s cryopump is mounted on the 10-inch cube vacuum chamber at the 7-m mark in Figure 6.1, directly over the 1-T superconducting magnet. An ion gauge mounted on the 10-inch cube vacuum chamber shows no change in vacuum pressure when the output valve of the accumulator is opened, indicating that the vacuum pressure increases by less than 10^{-9} torr. The final layer of vacuum protection is a 4.2-K, 1.5-mm-diameter, 20-mm-long cryogenic pumping restriction just after the

9-m mark of Figure 6.1. Background gas atoms and molecules incident on this pumping restriction freeze onto its cryogenic surfaces, with only the small fraction with straight-line ballistic trajectories that do not hit these surfaces entering the cryogenic Penning trap.

The vacuum pressure within the cryogenic Penning trap is too low to be measured by conventional instruments. The best method for determining this vacuum pressure is to use the stored antimatter itself. A calibrated number of $\bar{p}$ is loaded into the Penning trap and held for 15.3 h. No losses are observed beyond the 3% uncertainty in the number of loaded $\bar{p}$. The $\bar{p}$ lifetime is thus deduced to be more than 200 hours [89].

Chapter 7

Particle Loading and Manipulation

7.1 Plasma Manipulation

7.1.1 Plasma Transportation

Non-neutral plasmas are moved within the cryogenic Penning trap through gradual changes to individual electrode voltages (Figure 7.1). A series of 50 steps, each 40 ms long, smoothly translate the central position of the potential well from one electrode to the next [60]. Some of these steps are shown in Figure 7.1. These steps transport $\bar{p}$ from the bottom of the electrode stack and into the Ioffe trap region for $\overline{H}$ production and trapping experiments. Antiproton and e^+ are routinely transported throughout the electrode stack with negligible loss. The process is adiabatic and does not result in measurable plasma temperature increases after the translations.

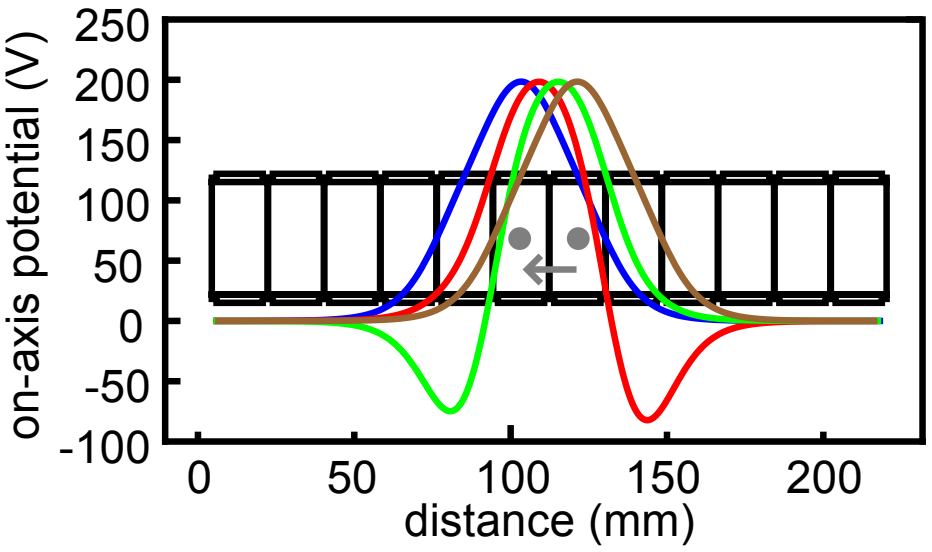

FIGURE 7.1: Non-neutral plasmas are moved from one electrode to the next using 50 steps. Four of the steps are shown. The plasma is moved from right to left, starting with the brown potential.

7.1.2 Rotating Wall

As discussed in Section 3.1.2, the field lines of the Ioffe trap will guide charged particles into the electrode stack walls unless they are less than 4 mm from the center of the Ioffe trap. Therefore, e^+ plasmas must be radially compressed in order to be useful for $\bar{H}$ trapping experiments. The cryogenic Penning trap is equipped with a segmented electrode in the upper part of the electrode stack (UTRW in Figure 7.2). A rotating-wall drive, as described in Section 5.5.3, is applied to the segmented electrode. This rotating-wall drive is typically used to compress e^+ plasmas, but can also be used for e^- plasma compression.

Two rotating-wall potential wells (See Figure 7.2) have been used to compress leptons in the upper part of the cryogenic Penning trap electrode stack. To maximally compress the lepton plasma, the single-electrode well holding the lepton plasma is slowly turned into a 5-electrode-long, 100-V-deep potential well shown in blue in Figure 7.2. A 1.5-MHz, 2-V_{rms} drive is applied to the segmented electrode for up to 800 s. The result is a e^+ plasma with a 2-mm radius. This compressed plasma

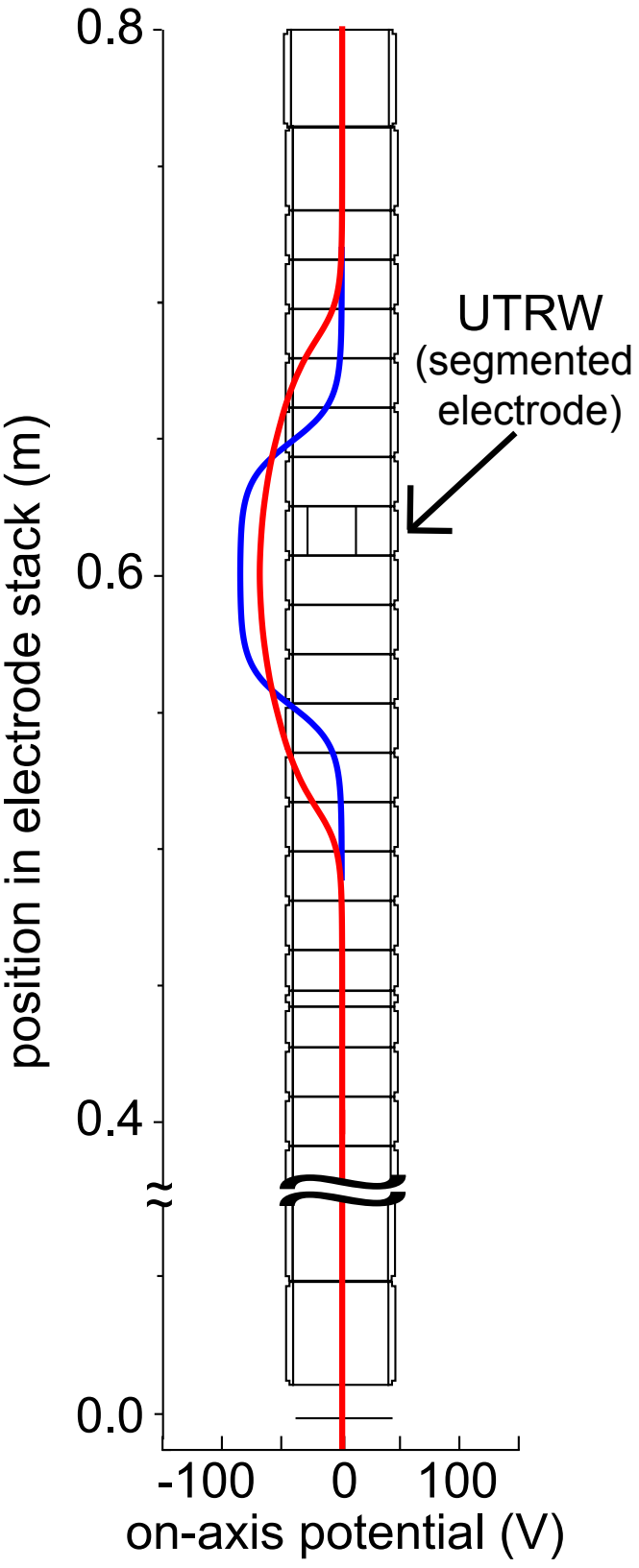

FIGURE 7.2: Two potentials used in the application of the upper-stack rotating wall. The long flat well (blue) provides a maximally compressed plasma with a 2-mm radius. The long harmonic well (red) can create plasmas with a 4-mm radius but does so without losing particles.

comes at the cost of losing approximately 50% of the e^+ upon starting the drive after the blue potential well of Figure 7.2 is formed.

An alternate rotating-wall setup is a 7-electrode-long, harmonic potential well shown in red in Figure 7.2 with a 5-MHz, 2-V_{rms} drive. The drive is applied for up to 1000 s, creating a plasma with a 4-mm radius. Though 4 mm is not as small of a radius as we can achieve with the long, flat potential well, this rotating-wall scheme does not result in e^+ loss upon forming the potential well or starting the rotating-wall drive.

The performance of the upper-stack rotating wall as a function of the duration of the rotating-wall drive is shown in Figure 7.3. The 5-electrode-long, flat well shown in Figure 7.2 in blue with a 1.5-MHz, 2-V_{rms} drive is used. Upon completion of the rotating-wall drive, a single-electrode potential well is recreated and the plasma radius is measured using the technique outlined in Section 4.1. Positrons and e^- are compressed to 2 mm after a 780-s application of the rotating wall.

7.2 Electron Loading

Electron cooling of $\bar{p}$ and e^+ is crucial for efficient loading of the $\overline{H}$ constituent particles. Electrons are loaded via the photoelectric effect by aiming an intense UV laser beam at the beryllium degrader (DEG in Figure 3.4) at the bottom of the cryogenic Penning trap.

The room-temperature components of the e^- loading apparatus are shown in Figure 7.4. The UV laser used is a KrF excimer laser (GAM Lasers Ex5) that produces 248-nm light pulses with up to 18 mJ of energy and 2 MW of peak power. The laser is fired with a reptiton rate of 1 Hz. The work function of beryllium is 3.6 eV [90], which is lower than the energy of the UV photons $E = h/\nu = 5$ eV, allowing e^- to be liberated from the degrader. The laser is located out of vacuum, away from

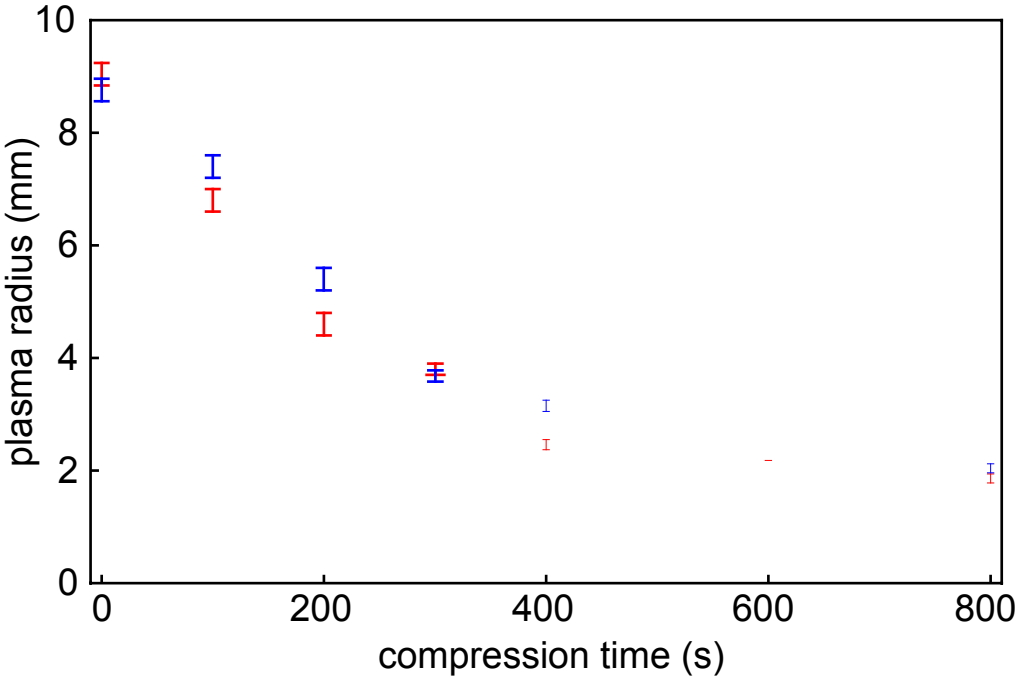

FIGURE 7.3: e^+ (red) and e^- (blue) are both radially compressed to 2 mm using the five electrode long flat well (the blue curve in Figure 7.2) and the upper-stack rotating-wall drive.

the large fringing field of the 1-T superconducting solenoid. The laser light enters the vacuum space through a sapphire window, as shown in Figure 7.4. A mirror at a 45° angle is mounted on a retractable stage in the vacuum space. To load e^-, the excimer mirror is positioned in the center of the vacuum space above the cryogenic Penning trap. The excimer laser is pulsed and the laser light is reflected down through the 20-mm-long, 1.5-mm-diameter pumping restriction (Figure 6.1) and into the cryogenic Penning trap. The excimer mirror is retractable to allow for e^+ to pass through the same pumping restriction when the stage is retracted.

The electrode-stack potentials used to load e^- is shown in Figure 7.5. The barrier applied to electrode LBE1 is pulsed down (dashed line in Figure 7.5) with each firing of the excimer laser to allow e^- to enter and become trapped in the potential well on electrode LTE3. Due to the fast cyclotron motion, the e^- are constantly

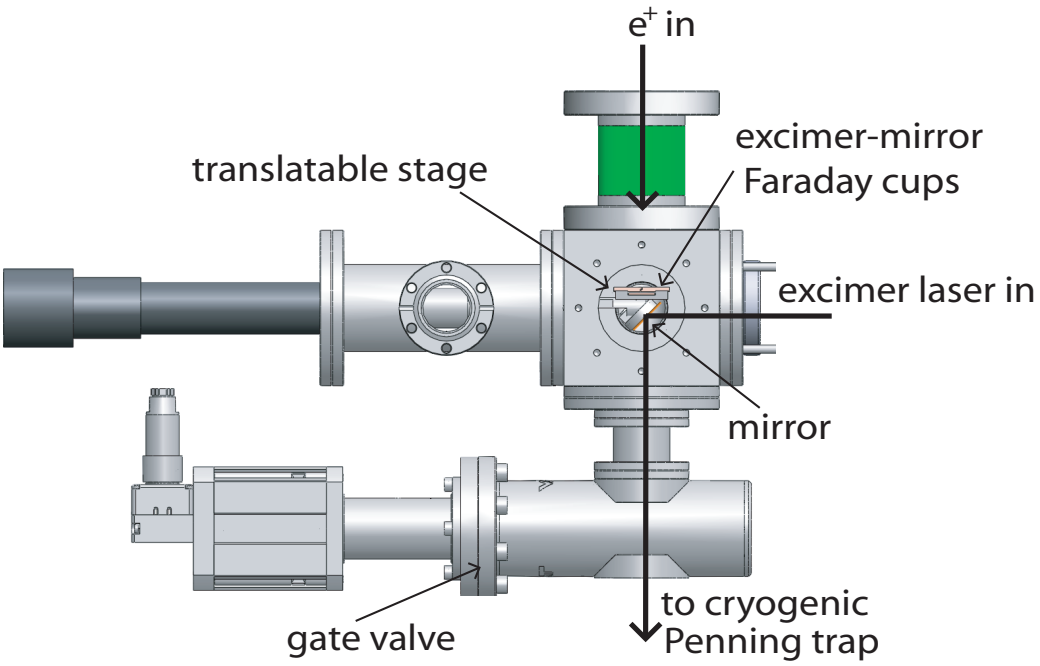

FIGURE 7.4: The retractable mirror used to reflect UV laser pulses down the central axis of the cryogenic Penning trap.

radiating away synchrotron energy and quickly cool into electrode LTE3 of Figure 7.5. The magnetic field at electrode LTE3 in Figure 7.5 is 3.7 T, which is produced by the combined 1-T solenoid and the field-boosting solenoid used for $\bar{p}$ loading, as described in Section 3.1.2. The cooling time constant τ_s (Equation (2.16)) for e^- in a 3.7-T magnetic field is 0.19 s. This time constant allows the e^- to be cooled sufficiently within 1 s, allowing for UV laser pulses at a repetition rate of 1 Hz. Approximately 10^7 e^- are collected with every excimer pulse. The depth of the potential well on LTE3 is increased by 1 V every second to accommodate the growing number of e^-.

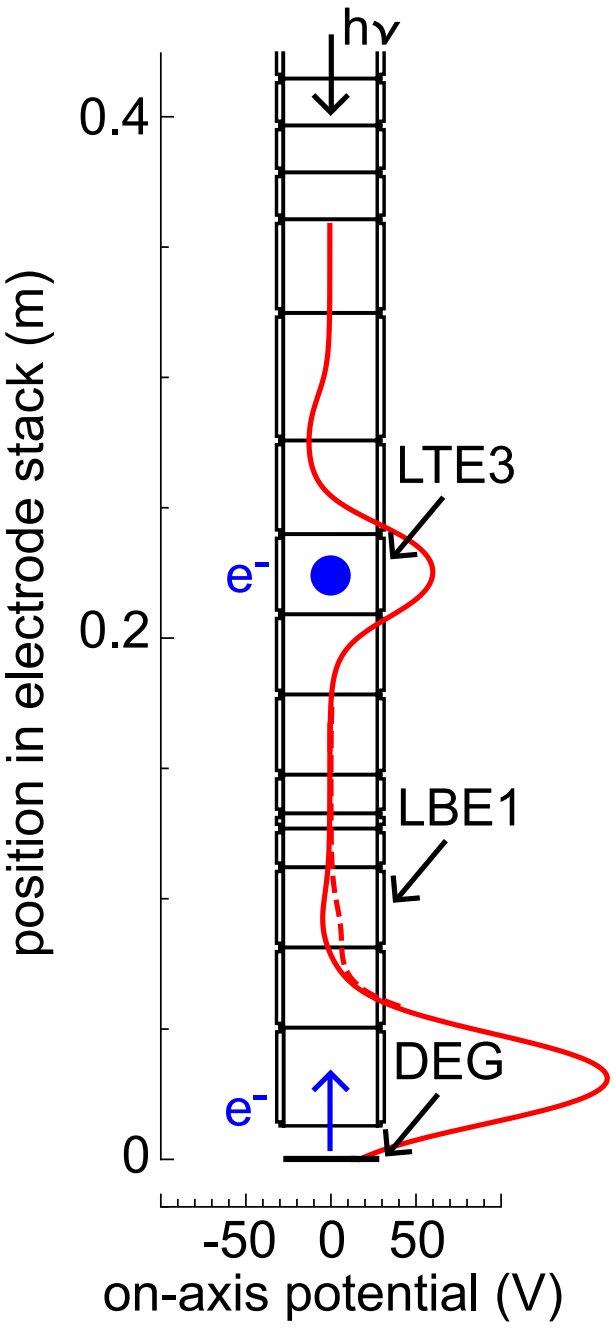

FIGURE 7.5: On-axis potentials used for e^- loading. The potential barrier applied to electrode LBE1 is pulsed down (dashed line) when the excimer laser is fired. See Figure 3.4 for full labelling of electrodes.

7.3 Antiproton Loading

7.3.1 Antiproton Slowing and Trapping

Trapping the $\bar{p}$ ejections from the AD in the cryogenic Penning trap requires them to be cooled by three orders of magnitude — from a 5-MeV/c bunch circulating in the AD to a 5-keV/c bunch that can be trapped in an electrostatic potential well.

The first energy-losing collisions happen within a mixture (at atmospheric pressure) of He and SF_6 in a 1-cm-long energy-tuning cell. Adjusting the fraction of SF_6 in the gas mixture adjusts the stopping power of the energy-tuning cell, allowing for some dynamic control over the $\bar{p}$ energy [91]. The full dynamic range of 0% SF_6 to 100% SF_6 corresponds to a $\bar{p}$ energy-tuning range of approximately 500 keV.

Most of the $\bar{p}$ energy is lost in the 100-μm-thick beryllium degrader. Approximately 0.5% of the $\bar{p}$ exit the beryllium degrader with less than 5 keV of energy.

The slowed $\bar{p}$ are caught in a 5-kV electrostatic potential well, which also contains 10^8 pre-loaded e^- in a nested potential well, as shown in Figure 7.6. The bottom barrier of the nested potential (applied to the DEG) is controlled using a custom-built high-voltage switch. The DEG is set to +0.6 kV before the $\bar{p}$ enter the cryogenic Penning trap. The large positive bias prevents secondary e^- from entering the cryogenic Penning trap along with the $\bar{p}$. Once the $\bar{p}$ have entered the trap, the bias to the DEG is set to -5 kV, capturing the $\bar{p}$.

The field-boosting solenoid (shown in Figure 3.5 and described in Section 3.1.2) increases the magnetic field at the bottom of the cryogenic Penning trap from 1 T to 3.7 T. The increased magnetic field more tightly constrains the transverse motion ($v_\perp$) created as the $\bar{p}$ pass through the beryllium foil [92]. Approximately

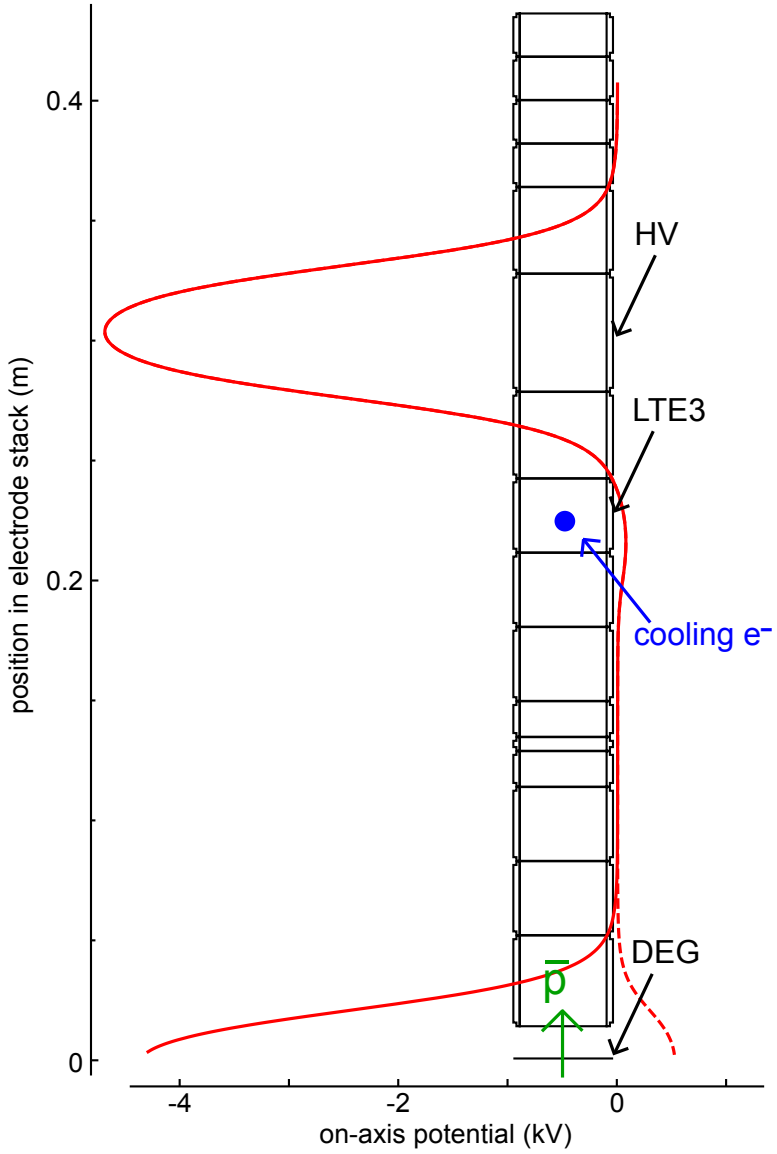

FIGURE 7.6: On-axis potentials used to catch and cool $\bar{p}$ via e^- cooling. A +100-V potential well that holds the cooling e^- is nested within the -5-kV potential well for $\bar{p}$ catching. The bottom barrier (DEG) is pulsed down after 60 s of e^- cooling to allow any remaining hot $\bar{p}$ to escape.

10^5 $\bar{p}$ are caught per bunch from the AD, an order of magnitude improvement over $\bar{p}$ catching in the 1-T field.

The synchrotron damping time (τ_s), given by Equation (2.16), is 0.19 s for e^- in a 3.7 T field, while τ_s is 37 years for $\bar{p}$ (due to the m^3 term). Collisions between the e^- and $\bar{p}$ transfer energy to the e^-, and the e^- quickly radiate away the energy. The time constant for thermal equilibrium is given by [93]

$$\tau_c = \frac{3(4\pi\epsilon_0)^2 m_{\bar{p}} m_e c^3}{8(2\pi)^{1/2} n_e e^4 \ln\Lambda} \left(\frac{kT_p}{m_p c^2} + \frac{kT_e}{m_e c^2} \right)^{3/2}, \tag{7.1}$$

where Λ is the Coulomb logarithm with a value of between 10 and 20. The cooling time is less than 60 s for an e^- plasma with $n_e = 10^7 \mathrm{cm}^{-3}$.

Collisions between the hot $\bar{p}$ and cold e^- cool the $\bar{p}$ for 60 s, after which most of the $\bar{p}$ are cooled into the e^- well (LTE3 of Figure 7.6), and the bottom barrier of the nested potential well (DEG in Figure 7.6) reverts to +0.6 kV, allowing the uncooled $\bar{p}$ to escape before the next $\bar{p}$ ejection from the AD. Repeated $\bar{p}$ ejections from the AD are caught in this fashion until the desired number of $\bar{p}$ are trapped in the cryogenic Penning trap. Stacking up to 10^7 $\bar{p}$ [26] has been demonstrated.

7.3.2 Rotating Electric Field

The combined e^--$\bar{p}$ plasma is compressed using a rotating electric field applied to a segmented electrode (LTE3 in Figure 7.7). The e^--$\bar{p}$ cloud is moved from LTE3 to LTE2 and the single-electrode well is slowly shifted to a 3-electrode-long well with the segmented electrode (LTRW in Figure 7.7) at one end. Only a small number of $\bar{p}$ are lost when adjusting the potential well, and very few are lost due to the rotating wall. A 9-V peak-to-peak, 1-MHz drive is applied to LTRW for 800 s to very slowly compress the e^--$\bar{p}$ plasma to approximately 4 mm in diameter. A long compression time is necessary to avoid excessive heating of the $\bar{p}$ plasma, which would result in losses. After compression, the single-electrode well is reformed and the e^--$\bar{p}$ plasma cools for an addition 30 s to dissipate any heat introduced by the rotating-wall drive. The field-boosting solenoid is then slowly turned off, and the e^--$\bar{p}$ cloud expands in the decreasing magnetic field. An interesting side effect is that, because the $\bar{p}$ and e^- have very different masses, they centrifugally separate

in the rotating electric field [27]. The e^-, being the lighter of the two, occupy the central region, while the $\bar{p}$ migrate further from the trap axis.

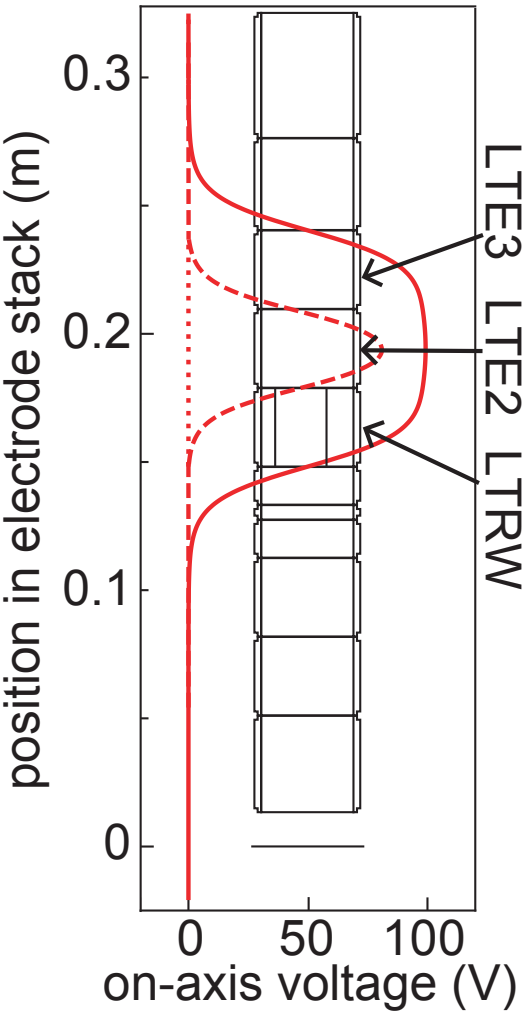

FIGURE 7.7: The single-electrode well used to hold $\bar{p}$ (dashed line) and three-electrode-long, flat potential well used to radially compress $\bar{p}$ with the rotating wall (solid line), and pulsed potential (dotted line) used to eject e^-.

7.3.3 Electron Ejection

After the field-boosting solenoid is turned off, the e^- are ejected. The axial center-of-mass frequency ($\omega_z/2\pi$) of the e^- is much higher than that of the $\bar{p}$, with axial periods in an 80-V potential well of 28 ns for the e^- and 1.2 μs for the $\bar{p}$. The potential well that holds the e^--$\bar{p}$ plasma is pulsed to 0 V (dotted line in Figure 7.7) for 75 ns — long enough for the e^- to leave, while short enough that almost all of

the $\bar{p}$ remain trapped. Four such pulses are typically used, removing all but a few hundred e^-. The small number of e^- that remain continue to cool the $\bar{p}$ cloud for an additional 10 minutes, reversing any $\bar{p}$ heating induced by pulsing the potential well.

7.4 Positron Loading

7.4.1 Nested Well for Positron Catching

The nested potential well used to catch e^+ ejections from the positron accumulator and cool them with e^- is shown in Figure 7.8. Since the e^+ are ejected from the positron accumulator with an energy of approximately 60 eV, a potential offset of approximately 60 V is applied inside the long potential well (between UTE2 and UBR4 in Figure 7.8) to slow the e^+ once they enter this well. Barriers at the top and bottom of the long well are on UTE2 and UBR4 in Figure 7.8, respectively. The positron accumulator sends a trigger signal with each e^+ ejection. After a delay of approximately 0.9 μs — the time of flight of the e^+ through the e^+ transfer guide — the top barrier is pulsed down (dashed line in Figure 7.8). The top barrier is lowered for long enough that the e^+ enter the nested well but the barrier is reinstated before the e^+ can reflect off of the bottom barrier and return to UTE2.

The e^+ catching efficiency is optimized by varying three parameters — the voltage offset, the time at which the top barrier is lowered, and the length of time the top barrier remains lowered. The optimal settings are found to be a 63-V potential-well offset, 0.90-μs delay between e^+ ejection and lowering the top barrier, and 460-ns wait before the top barrier is raised again. These parameters depend on the velocity of the e^+, which is dictated by the potential well that holds the e^+ just before they are ejected from the positron accumulator (Figure 5.16(j)).

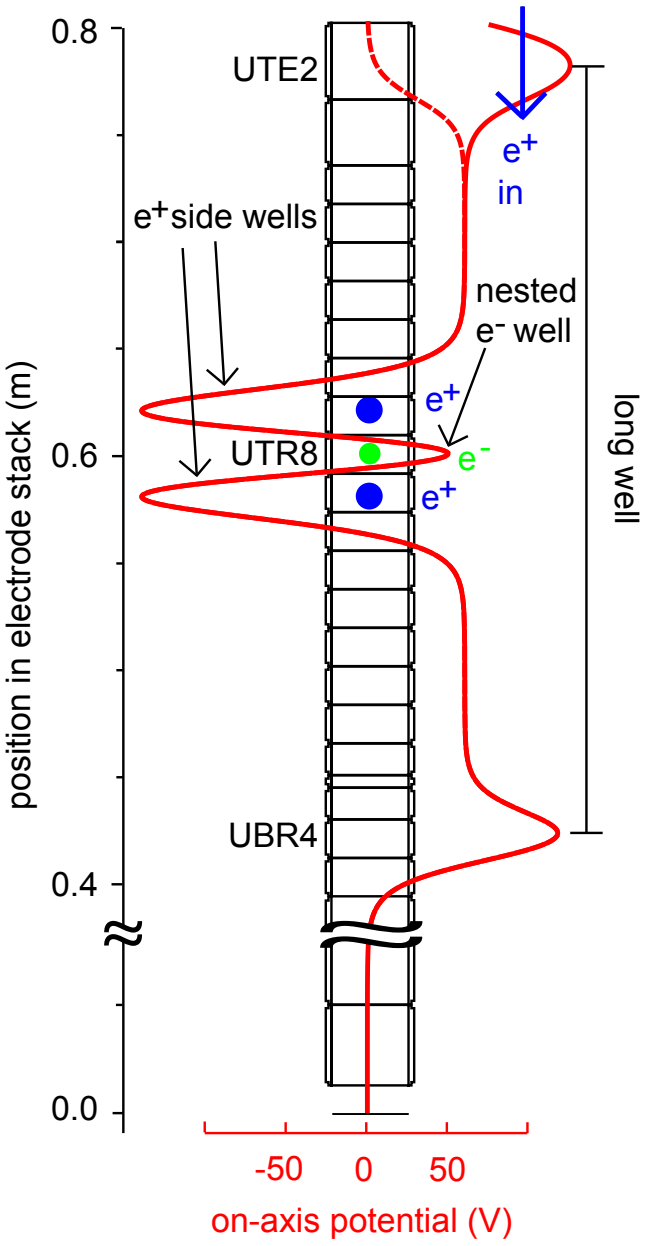

FIGURE 7.8: The nested potential well used to catch e^+ from the positron accumulator. The top barrier on electrode UTE1 is briefly pulsed down (dashed line) to allow e^+ to enter, and then re-established to trap e^+ between UTE1 and UBR4. Collisions with the e^- plasma held on electrode UTR8 cool the e^+ into two wells on either side of UTR8.

7.4.2 Electron Cooling of Positrons

The positron accumulator ejects e^+ every 30 s. The e^+ from the previous ejection must cool into one of the side wells in Figure 7.8 within 30 s, so they are not lost when the top barrier of the nested potential well (UTE2) is opened for the next e^+ ejection. The axial kinetic energy would have to be transferred to cyclotron energy to take advantage of the fast synchrotron cooling of e^+ in the 1-T field of the cryogenic Penning trap. With only 10^7 e^+ in the nested potential (the number of e^+ in each ejection from the positron accumulator), it takes more than 100 s for all of the e^+ to cool into the side wells of Figure 7.8 [94]. To cool the e^+ more quickly, e^- are loaded into the nested potential well of Figure 7.8.

Electrons loaded via photoemission are moved to the upper part of the electrode stack by moving them from one electrode to the next using the technique described in Section 7.1.1. These e^- form a plasma with a measured radius of approximately 1 cm and density of approximately 10^8 cm^{-3}. As the e^+ pass by the e^- plasma, they lose energy by collisions with e^-. The e^+ have approximately 35 eV of kinetic energy as they near the e^- plasma, as determined by the applied potentials of Figure 7.8 and the potential due to the e^- space charge, which is calculated using EQUILSOR. The e^+ need only lose approximately 3 eV of energy to become trapped in the side wells of Figure 7.8. The e^- cool the e^+ into the side wells of Figure 7.8 within a few seconds.

Using 1.5×10^8 cooling e^- results in over five times as many e^+ trapped and cooled in the cryogenic Penning trap compared with using no cooling e^-, given that there is only 30 s of cooling time available between e^+ ejections.

7.4.3 Stacking Positron Ejections

Many ejections from the positron accumulator are stacked in the cryogenic Penning trap to reach the hundreds of millions necessary for $\overline{\mathrm{H}}$ production trials. The positron accumulator ejects approximately 10^7 e^+ every 30 s. 60% of these e^+ enter the cryogenic Penning trap and 85% of these are caught in the long well of Figure 7.8 and cooled with e^-. Positron ejections from the positron accumulator are repeatedly caught and cooled in this fashion to load up to 2×10^8 e^+. The e^+ loading rate for this technique is 2.4×10^4 e^+/s/mCi — higher than any other loading rate of e^+ into a cryogenic Penning trap reported in the literature.

The cooling e^- can be removed after 2×10^8 e^+ are loaded since the large number of e^+ can now provide the cooling. The e^- are carefully swept out as shown in Figure 7.9(a). No e^+ loss is detected during the e^- sweep-out. With the e^- removed, the nested well is now replaced by the single-electrode, deeper e^+ well shown in Figure 7.9(b).

More e^+ can be loaded but the growing e^+ plasma becomes somewhat unstable in the anharmonic single-electrode well of Figure 7.9(b). As a result, the plasma radius slowly increases. To counteract this radial expansion, the single-electrode well is periodically transformed into the 7-electrode long harmonic well shown in Figure 7.10, and a rotating electric field is applied to electrode UTRW using a 5 MHz, 2-V_{rms} drive for 150 s. The long, harmonic potential well is then transformed back into the deep single-electrode potential well of Figure 7.9(b). This plasma compression cycle is done every 30 minutes during long e^+ loads. Both the single-electrode well of Figure 7.9(b) and the long harmonic well of Figure 7.10 are made increasingly deeper as more e^+ are loaded, as indicated by the dashed lines in the respective figures. Using this technique, up to 4×10^9 e^+ have been trapped and cooled in the cryogenic Penning trap. Figure 7.11 shows a linear loading trend up to 4×10^9 e^+. The linear trend demonstrates that e^+ cooling of the incoming e^+

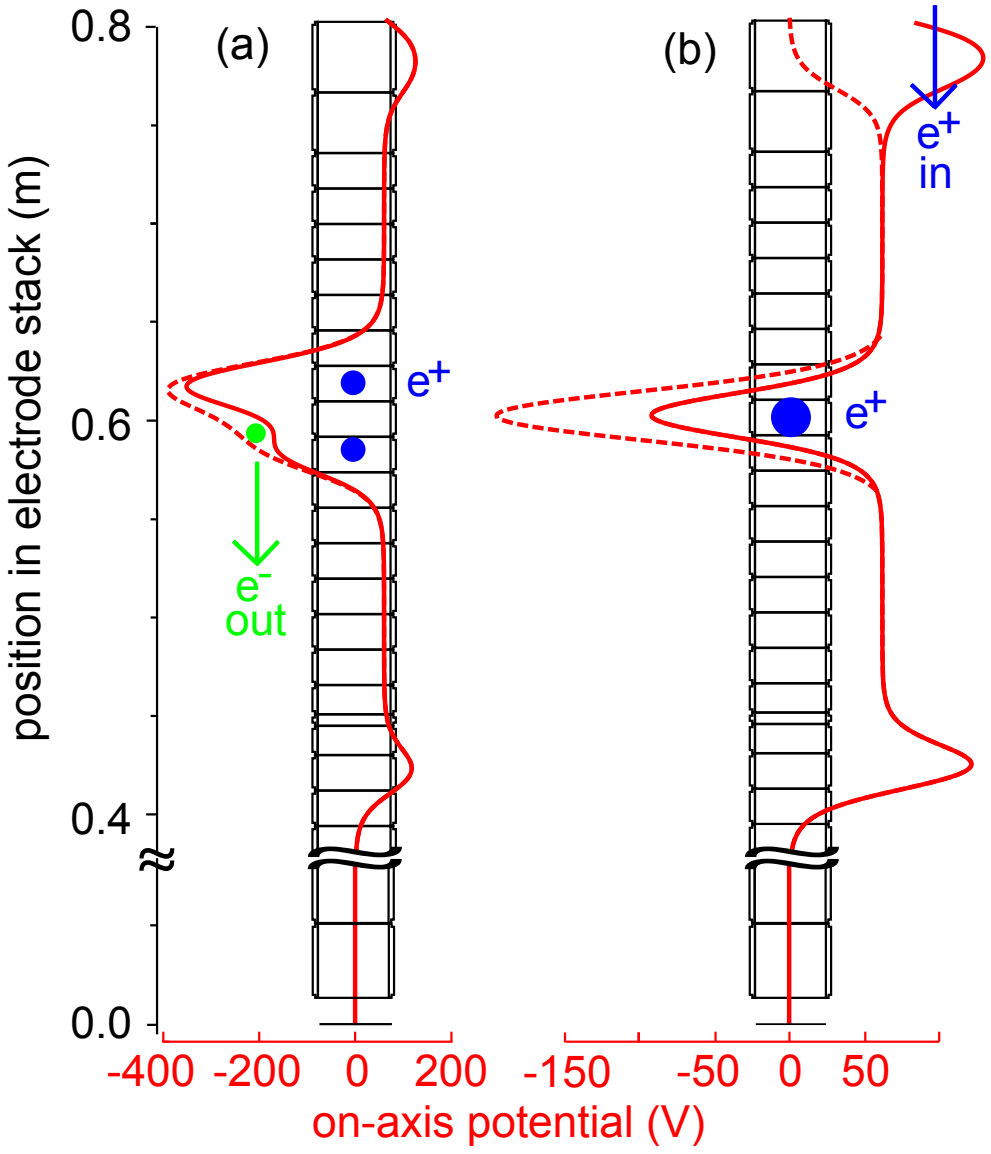

FIGURE 7.9: Electrode stack settings used to sweep e^- from the nested potential well (a) and a single-electrode potential well with 2×10^8 e^+ used to catch and cool more e^+ (b). The single-electrode well in (b) is made deeper (dashed lines) to accommodate increasing numbers of e^+.

is as efficient as the e^- cooling using the nested potential well. The linear trend therefore demonstrates that Ps production and e^+-e^- annihilation during the e^- cooling phase are not significant loss mechanisms. Although the e^+ loading rate is linear up to 4×10^9 e^+, the e^+ plasma spontaneously becomes very unstable for larger e^+ numbers and the radius rapidly expands, resulting in e^+ losses on the electrode stack walls. Since we have no $\overline{H}$ experiment that requires more than 4×10^9 e^+, we have not yet explored the parameters required to keep plasmas stable with even larger numbers of e^+.

The plasma of 4×10^9 e^+ is the largest number of e^+ ever contained in a single ion trap.

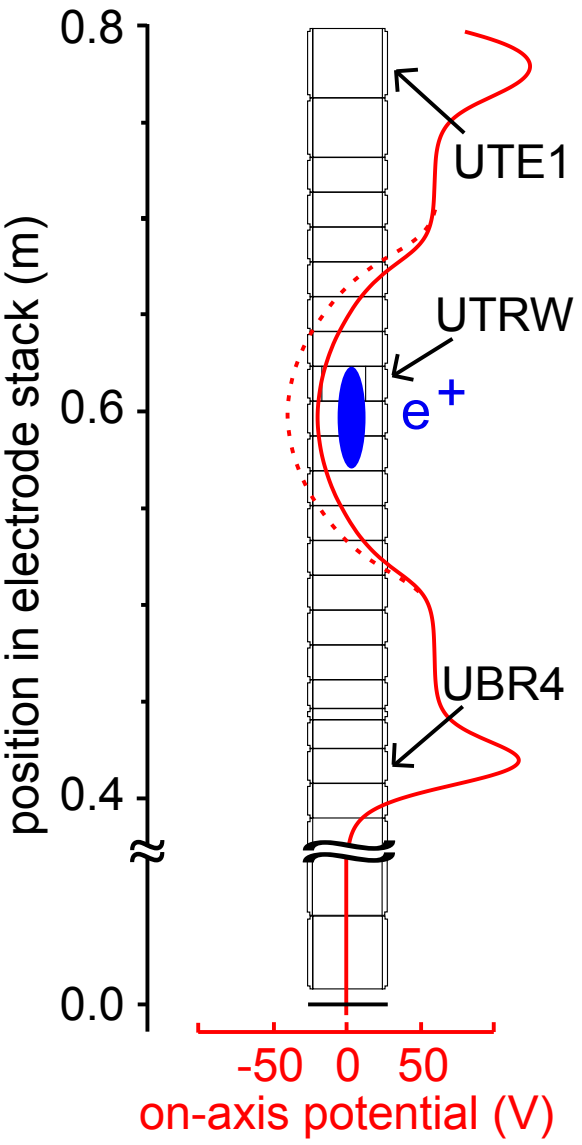

FIGURE 7.10: The seven-electrode-long harmonic well that is used to radially compress the growing e^+ plasma (solid line). The depth of the potential well increases as the number of e^+ increases (dashed line). The potential well depth after 1×10^9 e^+ are loaded is shown by the dashed line.

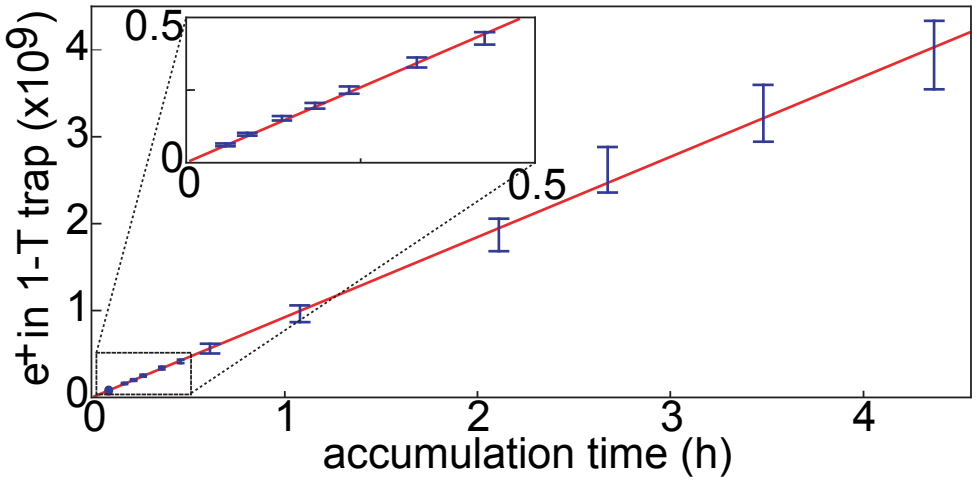

FIGURE 7.11: Linear stacking up to 4×10^9 e^+. The inset shows e^+ loading when e^- cooling is used exclusively. The same linear trend fits the e^- and e^+ cooling regimes.

Chapter 8

Antihydrogen Production

ATRAP uses two methods of $\overline{\mathrm{H}}$ production: Three-body-recombination (TBR) and two-stage charge exchange. In three-body recombination (Section 8.1), plasmas of e^+ and $\bar{p}$ are mixed in a nested potential well where e^+-e^+ collisions remove energy so that $\overline{\mathrm{H}}$ can form. Two-stage charge exchange (Section 8.2) is used by ATRAP to produce cold, Rydberg $\overline{\mathrm{H}}$ that might be more easily captured in the Penning-Ioffe trap.

8.1 Three-Body Recombination

8.1.1 Creating Antihydrogen by Three-Body Recombination

Antihydrogen production via three-body recombination was first proposed by Gabrielse *et al* shortly after the first $\bar{p}$ were trapped in an ion trap [95]. Three-body recombination has since produced thousands of $\overline{\mathrm{H}}$ atoms per trial [96], more than any other $\overline{\mathrm{H}}$ production method used in the laboratory.

Three-body recombination occurs when $\bar{p}$ are made to pass through a e^+ plasma. Two e^+ elastically scatter in the vicinity of an $\bar{p}$. One e^+ becomes bound to the $\bar{p}$ to form $\bar{H}$, while the other e^+ takes away excess energy. The process (shown schematically in Figure 8.1) is written as

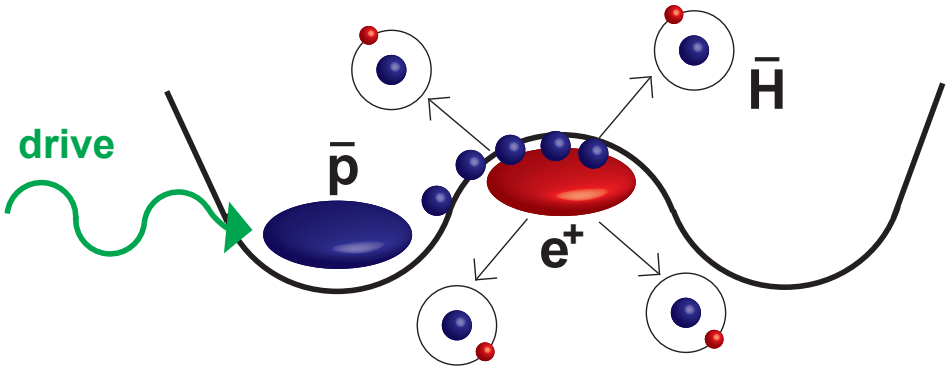

FIGURE 8.1: A schematic demonstrating three-body recombination using an rf drive to mix the $\bar{p}$ with the e^+.

$$e^+ + e^+ + \bar{p} \rightarrow \bar{H} + e^+. \tag{8.1}$$

The antihydrogen recombination rate per $\bar{p}$ via three-body recombination is written as

$$\nu_{TBR} = (n_{e^+}\sigma_{TBR}v_{e^+})\left(\frac{4}{3}\pi b_{min}^3 n_{e^+}\right), \tag{8.2}$$

where $b_{min} = q^2/(4\pi\epsilon_0 k_B T)$ is the minimum distance of closest approach. A few relations simplify the recombination rate: $\sigma_{TBR} \propto b_{min}^2$ and $b_{min} \propto T^{-1}$ and $v_{e^+} \propto T^{1/2}$. Therefore $\nu_{TBR} \propto n_{e^+}^2 T^{-9/2}$. The recombination rate is heavily dependent on the e^+ density and temperature. The constant of proportionality has been calculated in the zero-field limit, and in the limit that $\|\vec{B}\| \rightarrow \infty$, and found to vary by two orders of magnitude in those calculations. This simplified rate explanation is also complicated by collisions that can ionize the $\bar{H}$ before it decays to a more tightly-bound state.

ATRAP uses a variety of methods to excite $\bar{p}$ into a neighbouring e^+ plasma. Initially, the two plasmas (of opposite charge) are held in separate wells (as in Figure 8.1). Antiprotons are given additional energy to move them into the e^+ well using either noise drives, coherent chirped drives, slow chirped drives, or chirped drives with e^+ well sweeps [60]. The mixing times range from 2 ms to 15 min.

8.1.2 Trapping Antihydrogen Created by Three-Body Recombination in a Ioffe Trap

When the Ioffe trap is energized, any $\overline{H}$ created at the center of the Ioffe field remains trapped if it has less than 375 mK of kinetic energy (the depth of the Ioffe magnetic potential) and as long as radiative decays towards the ground state do not result in a e^+ spin flip. Such a spin flip would change an atom from a low-field-seeking state, to a high-field-seeking state that would be repelled from the trap. After completing the $\bar{p}$-e^+ mixing steps, the $\bar{p}$ and e^+ that do not form $\overline{H}$ are swept from the Penning-Ioffe trap using axial electric fields of +5 V/cm and then −5 V/cm. Antihydrogen is detected from annihilation products when the Ioffe trap is turned off and the $\overline{H}$ is free to strike the Penning-trap electrode stack.

The ATRAP detectors cannot distinguish between $\overline{H}$ and $\bar{p}$ annihilations. In principle, this could be a problem, since $\bar{p}$ could also be trapped by a magnetic bottle [97]. However, the observed annihilations detected when the Ioffe trap is turned off cannot result from magnetically trapped $\bar{p}$ for two reasons. First, the axial coils of the Ioffe trap remain energized when the radial field is turned off. Any $\bar{p}$ trapped by the coils remain trapped by the axial fields while the $\overline{H}$ exit radially. Second, the 5-V/cm electric field provides enough force on the $\bar{p}$ that they cannot remain trapped in the magnetic bottle of the axial coils of the Ioffe

trap unless they have at least 137 eV of cyclotron energy [97]. No plausible source of such high cyclotron energies can be identified.

ATRAP [98] has successfully trapped $\overline{\mathrm{H}}$ produced via three-body recombination in a Penning-Ioffe trap. From twenty trials using different parameters in various drive techniques, an average of 5 ± 1 $\overline{\mathrm{H}}$ atoms per trial (105 $\overline{\mathrm{H}}$ atoms in total) is detected. Figure 8.2 shows the combined analysis of the twenty trials. The data is put into 1-s bins with the dark blue bin being the time window in which the Ioffe trap is turned off, and $\overline{\mathrm{H}}$ are released. Figure 8.2(a) shows the total counts per bin over twenty trials, Figure 8.2(b) shows the probability that the signal attributed to 105 $\overline{\mathrm{H}}$ could be from a fluctuation in background counts — a chance of 1 in 10^7. Figure 8.2(c) shows the combined signal of twenty control trials where no particles are loaded into the trap but the Ioffe trap is energized and turned off in the same manner as for $\overline{\mathrm{H}}$ trapping trials. The lack of signal in the relevant time bin demonstrates that the sudden flux change from quickly turning off the Ioffe trap magnets does not induce false signals in the detector electronics.

8.2 Two-Stage Charge Exchange

Advances in trapping and storage of large numbers of cryogenic $\bar{\mathrm{p}}$ and e^+ encouraged the proposal of a novel, laser-controlled, two-stage charge-exchange process to form $\overline{\mathrm{H}}$ [99]. The two-stage process is shown schematically in Figure 8.3. Cs is laser-excited to a Rydberg state by two laser excitations. First, 852-nm laser light excites the Cs atoms from the ground state to an intermediate excited state ($6\mathrm{S}_{1/2}$ to $6\mathrm{P}_{3/2}$), then 511-nm laser light excites the Cs atoms to a Rydberg state ($6\mathrm{P}_{3/2}$ to $n\mathrm{D}_{5/2}$). The Rydberg Cs can donate its Rydberg e^- as it passes through a e^+ cloud, producing Rydberg positronium (Ps). The Rydberg Ps are neutral atoms, and, as such, they are not confined by the electrostatic potentials that confine the e^+ and $\bar{\mathrm{p}}$. Since the momentum distributions of the e^+ within the plasma and Cs

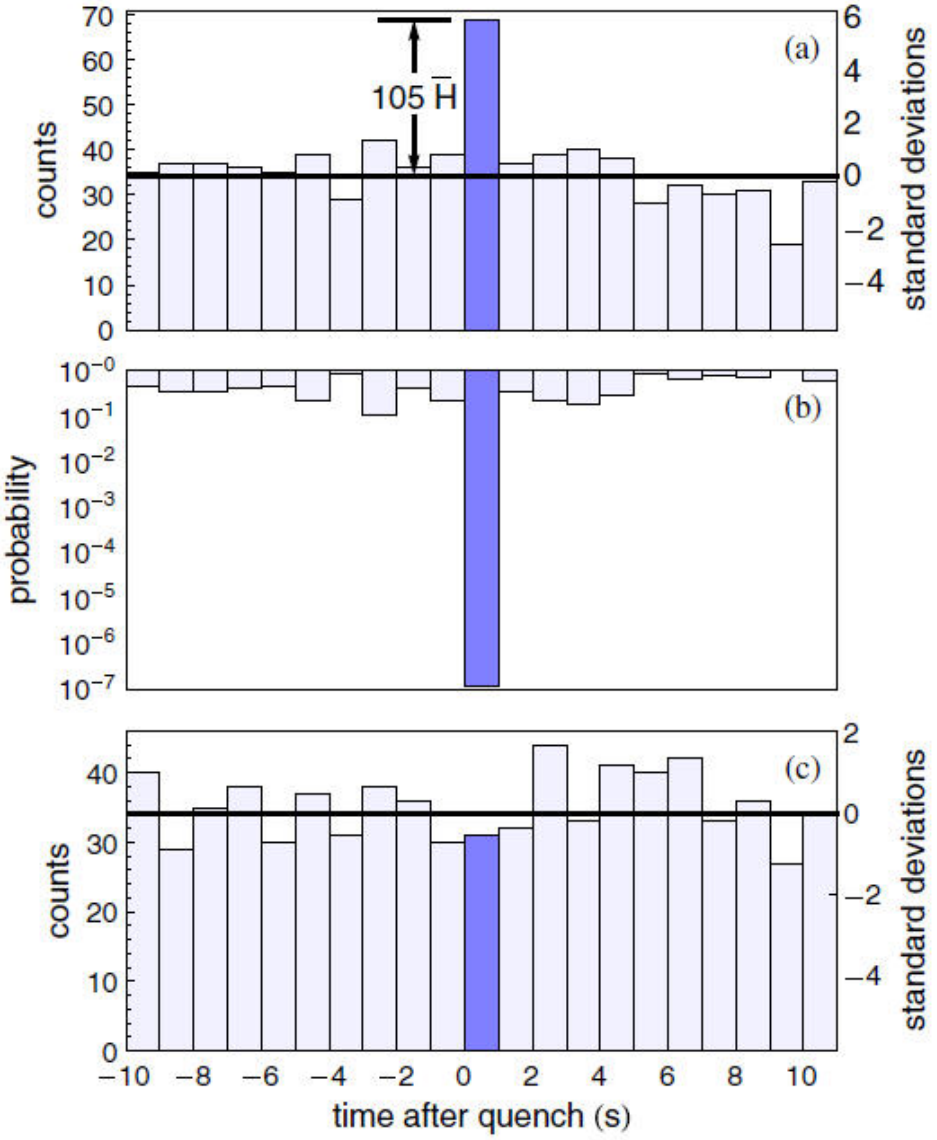

FIGURE 8.2: Statistics from twenty $\bar{H}$ trapping trials. The total trapped $\bar{H}$ signal (a), the probability that the trapped $\bar{H}$ signal is due to a spike in background signal detection (b), and the results of twenty control trials where the Penning-Ioffe trap is operated as in normal $\bar{H}$ trapping trials but with no particles in the trap (c). Figure from [12].

Rydberg e^- are isotropic, the Rydberg Ps exit the e^+ cloud isotropically. Some of this Rydberg Ps has a trajectory pointing towards the cloud of trapped $\bar{p}$, and those Rydberg Ps can undergo a second charge exchange to produce $\bar{H}$ and a free e^-. These processes are resonant, resulting in the Rydberg Ps and $\bar{H}$ having a binding energy similar to that of the Rydberg Cs. The charge-exchange processes are written as

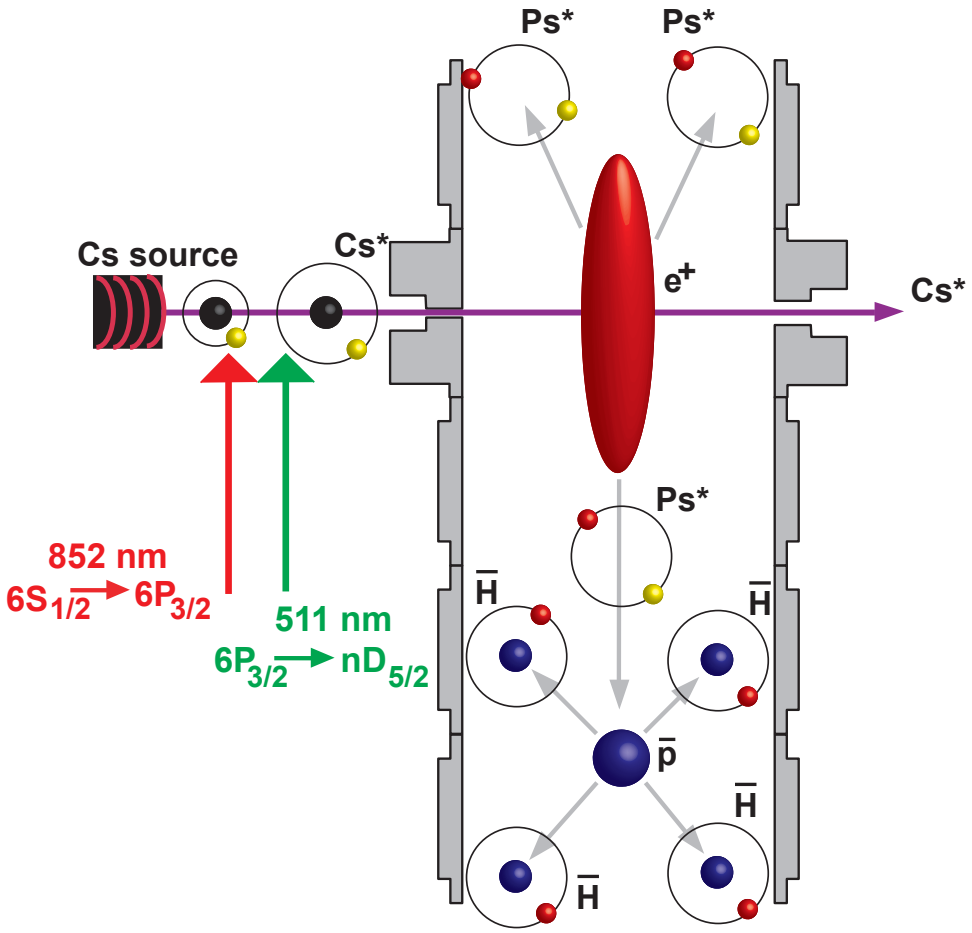

FIGURE 8.3: A schematic demonstrating two-stage charge exchange in the ATRAP cryogenic Penning trap.

$$Cs^* + e^+ \rightarrow Ps^* + Cs^+$$
$$Ps^* + \bar{p} \rightarrow \bar{H}^* + e^-. \tag{8.3}$$

The cross sections of the two charge-exchange processes in Equation (8.3) are (for sufficiently slow particles and atoms) approximately [99]:

$$\sigma_{Ps} = 9.7 n_{Cs}^4 \pi a_0^2 \tag{8.4}$$
$$\sigma_{\bar{H}} = 58 n_{Ps}^4 \pi a_0^2 \approx 14.5 n_{Cs}^4 \pi a_0^2. \tag{8.5}$$

These cross-sections have values on the order of $10^8 a_0^2$ for $n = 42$, due to the n^4 term.

Two-stage charge exchange has some important advantages over the more-often used three-body recombination. These advantages are especially important considering the final goal of trapping large numbers of $\overline{\mathrm{H}}$ atoms. Three-body recombination requires that the $\bar{\mathrm{p}}$ are driven out of their potential well and into the e^+ cloud. The energy added to the $\bar{\mathrm{p}}$ in this process leads to hotter $\overline{\mathrm{H}}$ being produced, making them more difficult to trap in the 375-mK-deep Ioffe trap. The $\bar{\mathrm{p}}$ in two-stage charge exchange remain in the same potential well, and their temperature and energy are largely unchanged during the process since the Rydberg Ps atoms (which are neutral and low mass) bring the e^+ to the $\bar{\mathrm{p}}$ for $\overline{\mathrm{H}}$ production. This lack of heating may allow for better use of our ability to adiabatically cool the $\bar{\mathrm{p}}$ to 3.5 K [26].

Another important advantage of two-stage charge exchange is that it allows for control over the binding energy of the $\overline{\mathrm{H}}$ atoms. The results of classical trajectory Monte Carlo calculations and Runge-Kutta simulations [99] [100] show that the $\overline{\mathrm{H}}$ produced after the second charge-exchange process have a narrow distribution of n-states just slightly below that of the Rydberg Cs atoms that start the two-stage charge-exchange process.

One final disadvantage of three-body recombination when compared to two-stage charge exchange is that, in three-body recombination, the $\bar{\mathrm{p}}$ must enter the dense e^+ plasma, acquiring its rotational velocity ($v_\theta = |\vec{E} \times \vec{B}|/B^2$) within one cyclotron period. Equation 2.19 shows that an $\bar{\mathrm{p}}$ that enters a e^+ plasma with density 1×10^7 cm^{-3} (a typical density for ATRAP $\overline{\mathrm{H}}$ experiments) acquires a rotational velocity of 100 r m/s, where r is the radius in mm. Antiprotons with $r > 1.0$ mm will acquire enough velocity (375-mK $\overline{\mathrm{H}}$ have a speed of 100 m/s) that the resulting $\overline{\mathrm{H}}$

produced are not confined by the Ioffe trap. In two-stage charge exchange, the $\bar{p}$ do not enter the e^+ plasma at all, thereby avoiding this effect.

The most obvious disadvantage of using two-stage charge exchange (as compared to three-body recombination) is the smaller production rate. Larger numbers of e^+ and $\bar{p}$ and longer run times are needed to make comparable numbers of $\overline{H}$.

ATRAP used the two-stage charge-exchange process to create $\overline{H}$ in a cryogenic Penning trap in 2004 [101]. A beam of Cs atoms produced by heating a Cs metal dispenser were optically excited to a Rydberg state using a diode laser and a copper-vapour laser. The Rydberg Cs beam passed through a hole in the electrode stack, and through a cloud of 1.4×10^6 e^+, undergoing a charge exchange to create Rydberg Ps. Approximately 1300 Rydberg Ps could be detected in a pair of ionizing detection wells about 1.5 cm from the e^+ cloud, indicating a total production of approximately 42 000 Rydberg Ps atoms [102]. Some Rydberg Ps traveled along the axis of the electrode stack, moving through a cloud of 2.4×10^5 $\bar{p}$ located less than 0.5 cm away. Using a detection well to Stark ionize the $\overline{H}$ and trap the $\bar{p}$ for counting, ATRAP detected a total of 14 $\overline{H}$ over 6 trials. Assuming an isotropic distribution of $\overline{H}$ production, these 14 $\overline{H}$ would indicate that between 100 and 200 $\overline{H}$ were produced.

Many aspects of the original experiment have been upgraded to produce $\overline{H}$ via two-stage charge exchange in the latest generation of ATRAP cryogenic Penning traps. The pulsed, fixed-frequency copper-vapour laser used in the excitation of Cs in 2004 has been replaced with a tunable, narrow-linewidth, continuous-wave laser system built by the Mainz contingent of ATRAP [103]. Given the improvements described in Chapters 5 and 7, positrons are loaded 10 000 times faster and about 2 500 times as many e^+ are available for Rydberg Ps production. Antiproton loading techniques have also been improved, resulting in 50 times more $\bar{p}$ available for $\overline{H}$ production.

The following sections give the details for this upgraded experiment for the three steps that make up two-stage charge exchange: The creation of a beam of Rydberg Cs atoms (Section 8.2.1, Section 8.2.2), the first charge exchange to produce Rydberg Ps (Section 8.2.3), and the second charge exchange to produce $\overline{\mathrm{H}}$ (Section 8.2.4).

8.2.1 Rydberg Cs Apparatus

The new apparatus used to produce Rydberg Cs within the vacuum space of the cryogenic Penning trap is shown in Figure 8.4. Cs atoms are provided by a resistively heated Cs metal dispenser (AS-3-CS-150-V from ALVATECH) containing 150 mg of Cs. It is heated to 600 K by applying between 4 and 5 A of current for approximately 6 minutes. Once warmed up, the current is decreased by 0.25 A and left at this current for the remainder of the experiment — typically 20-30 minutes.

One concern is that the Cs source might heat the 1.2-K electrodes. Several layers of thermal shielding prevent excess heating of the electrode stack. The first layers of thermal shielding are the 4.2-K Cs enclosure and 4.2-K radiation baffle mounted on the titanium flange in Figure 8.4. The 1.2-K, 0.8-mm-diameter baffles, also shown in Figure 8.4, provide more thermal protection for the electrode stack, while also collimating the Cs beam. The temperature of the electrode stack and current applied to the Cs source are shown in Figure 8.5. After 26 minutes of applied current to the Cs oven, the electrode stack warms by less than 0.4 K.

As shown in Figure 8.4, Cs enters the electrode stack through a 0.8-mm-diameter hole in the electrode in which the e^+ are held (the electrode labeled CS in Figure 3.4) and exits through a 2.5-mm-diameter hole on the opposite end. The larger-diameter exit hole ensures that Cs atoms will not be deposited onto the

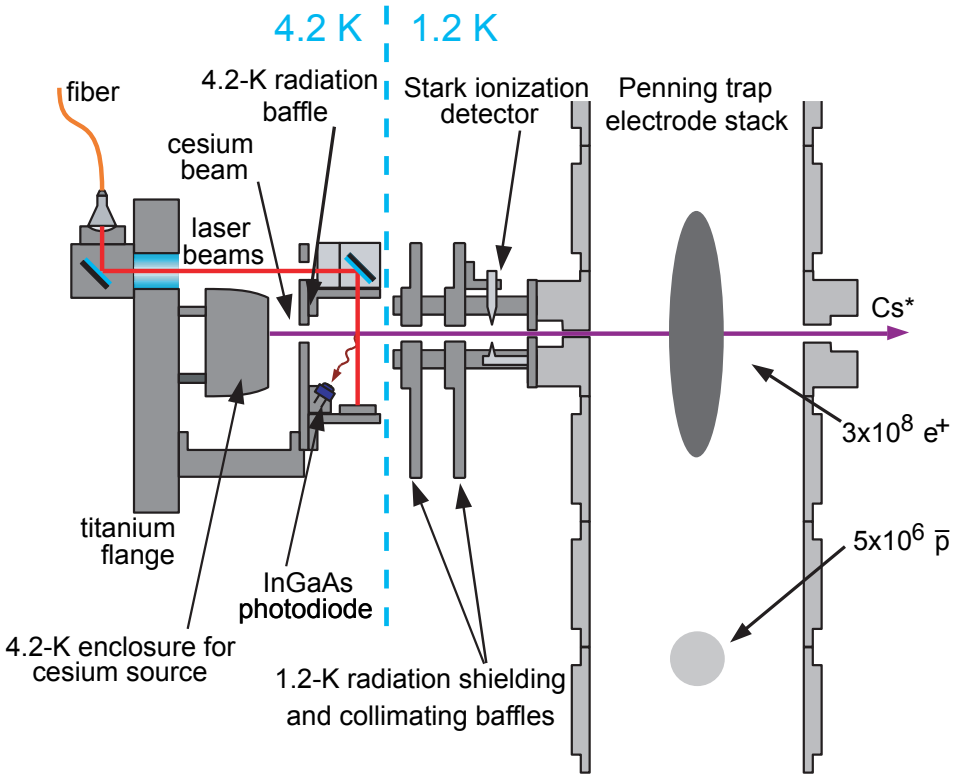

FIGURE 8.4: The Rydberg Cs apparatus. Laser light is transmitted through a single fiber into the 4.2-K apparatus. The Cs oven is heated and the emitted Cs is excited to Rydberg Cs. Photodiodes and a Stark-ionization detector are used to measure fluorescence and ions, respectively. Figure adapted from reference [103] (not to scale).

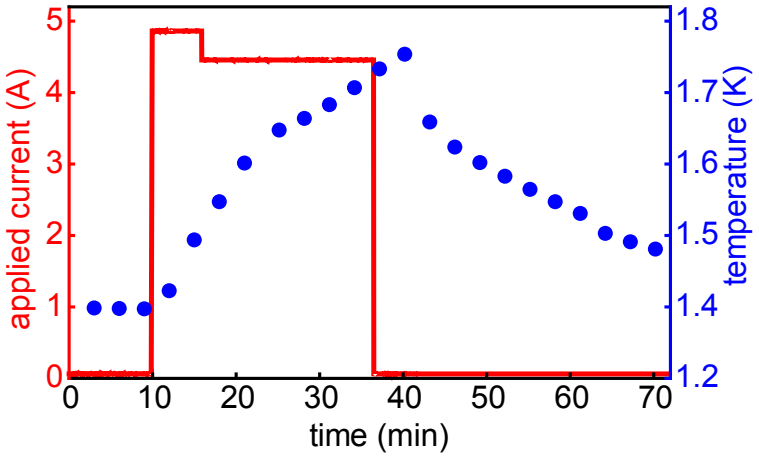

FIGURE 8.5: The electrode stack temperature while current is applied to the Cs oven. The limited increase in temperature indicates good thermal shielding between the 1.2-K electrode stack and the 600-K Cs oven.

inside surface of the electrode, which might otherwise cause shorts between electrodes or electric potential imperfections due to surface charging or patch potentials.

The Mainz group within ATRAP built tunable laser sources (shown schematically in Figure 8.6), for exciting Cs atoms to Rydberg states [103]. The first transition ($6S_{1/2}$ to $6P_{3/2}$) is driven by 852-nm laser light provided by an external-cavity diode laser (ECDL), while the second transition ($6P_{3/2}$ to $nD_{5/2}$) is driven by 511-nm laser light provided by a 1022-nm ECDL and a frequency-doubling cavity. The frequency-doubling cavity outputs up to 200 mW of 511-nm laser light.

Because of narrower linewidths, this laser system creates 10 times more Rydberg Cs atoms compared to the system used in 2004. The lasers are tunable over 10 GHz, allowing the 511-nm laser to excite Cs to a wide range of Rydberg states ($20 \leq n \leq$ ionization) and to make Rydberg Cs with the Zeeman shift from the 1-T field of the Penning trap, as well as that from the 3.2-T field of the Penning-Ioffe trap.

The Cs excitation laser beams enter the cryogenic Penning trap through a single fiber and produce Rydberg Cs *in situ*, at the intersection of the laser beams and the Cs beam in Figure 8.4. The fiber is mounted on the 4.2-K titanium flange that holds the Cs source in Figure 8.4. The end of the fiber is butted up against a 10-mm ball lens with a refractive index of 2.0, which collimates the optical fiber output. The laser light passes through a 0.6-cm-thick MgF_2 window glued into the 4.2-K titanium flange shown in Figure 8.4 and is deflected down to intersect the path of the Cs atoms.

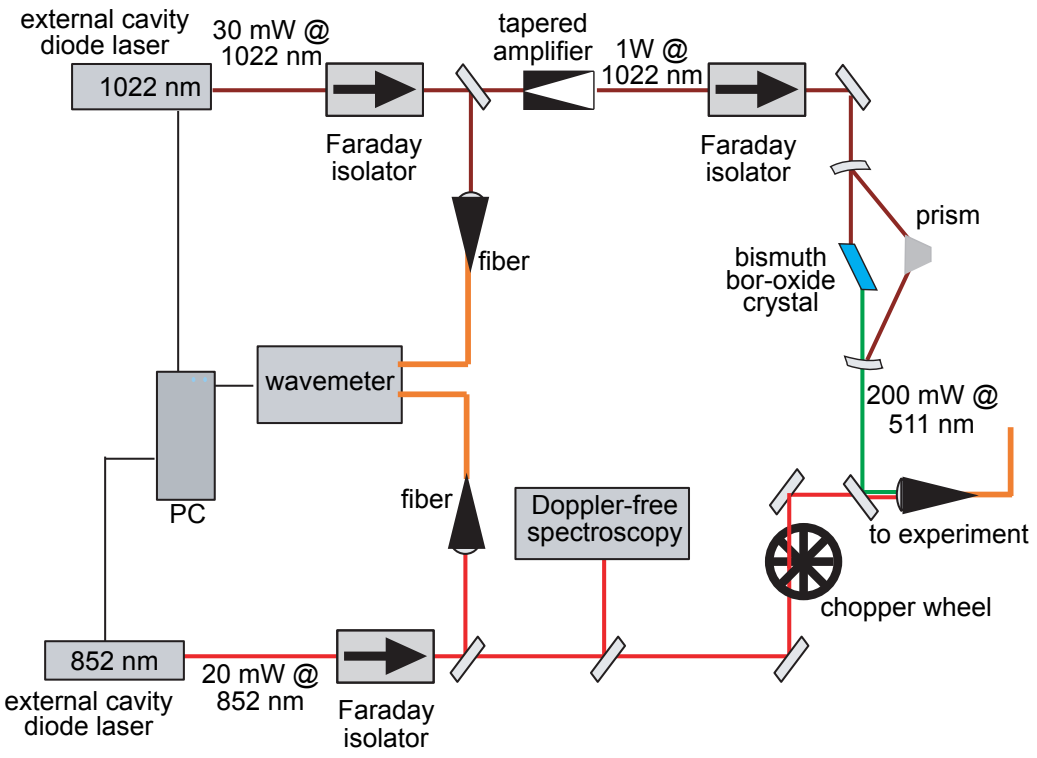

FIGURE 8.6: The Mainz laser system used to excite Cs to a Rydberg state.

8.2.2 Cs Excitation States

The Cs excitation takes place in a large magnetic field (due to the 1-T superconducting solenoid) and thus the energy levels of the atoms are Zeeman shifted. Simplified level diagrams of a Cs atom in a 0-T and 1-T magnetic field are shown in Figure 8.7.

8.2.2.1 $6S_{1/2}$ to $6P_{3/2}$

The Hamiltonian for calculating the Zeeman shift for the ground-state Cs atom in a large field can be approximated

$$H_B = A_{hfs} m_I m_J + \mu_B B_0 (g_J m_J + g_I m_I), \tag{8.6}$$

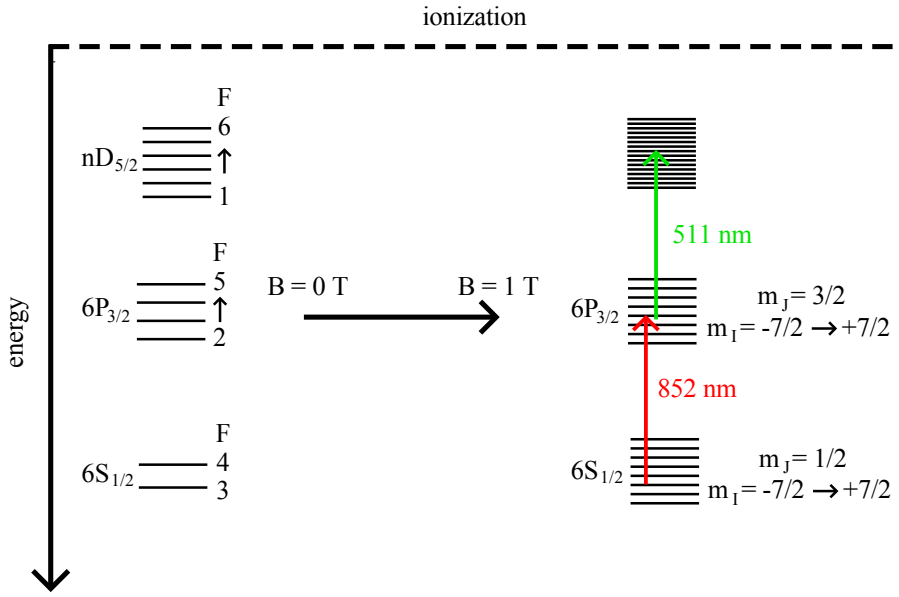

FIGURE 8.7: A simplified level diagram of a Cs atom in a 0-T field (left) and 1-T field (right).

where B_0 is the magnetic field, assumed to be in the z-direction, A_{hfs} is a hyperfine constant, $I = 7/2$ and m_I are the nuclear angular momentum and its projection onto the z-direction, J and m_J are the total angular momentum of the e^- and its projection onto the z-direction, and μ_B is the Bohr magneton.

The 1-T scale of the magnetic field puts the ground-state Cs atoms in an intermediary regime where the strength of the magnetic interaction is comparable to the hyperfine splitting, and thus both are included in Equation (8.6). Perturbation theory is no longer applicable on either the magnetic interaction term or the hyperfine splitting term. One therefore needs to diagonalize $H_{hfs} + H_B$ to find the eigenvalues.

The energy levels of the $6P_{3/2}$ state are not shifted due to the hyperfine splittings ($A_{hfs}m_I m_J$ in Equation (8.6)) nearly as much as the $6S_{1/2}$ state. $A_{6S_{1/2}} = h \cdot 2.298$ GHz, while $A_{6P_{3/2}} = h \cdot 50.288$ MHz [104]. Therefore, the energy levels of the $6P_{3/2}$ state can be calculated with the first term in Equation (8.6) treated as a perturbation.

8.2.2.2 $6P_{3/2}$ to $nD_{5/2}$

The Mainz laser system is tunable, allowing us to choose an optimal Cs Rydberg state for two-stage charge-exchange experiments. An nD state is chosen since it will mix with higher-ℓ states in the 1-T magnetic field more readily than nS states. These higher-ℓ states have longer lifetimes, increasing the likelihood that the Rydberg Cs atoms will survive the 6-cm trip from the Cs excitation point to the e^+ plasma at the center of the electrode stack in Figure 8.4.

The choice of n is influenced by many factors, thorough discussions of which are contained in references [30] and [31]. A higher-n Rydberg Cs state leads to a larger cross section (Equation (8.3)) and longer lifetimes. On the other hand, higher-n states are less desired since the nD state mixes with more higher-ℓ states, making the dipole matrix element for excitation smaller. Also, the higher-n states Stark-ionize in smaller electric fields and therefore can be ionized by the electric fields caused by the Penning trap electrodes or the charged plasmas. The optimal Rydberg Cs state is found to be approximately 42, and therefore we use the $42D_{5/2}$ state.

For the $42D_{5/2}$ Cs, the hyperfine interaction is negligible, but the diamagnetic term can no longer be ignored. Thus, the Hamiltonian due to the magnetic field is

$$H_B = \mu_B B_0(g_l m_l + g_S m_S + g_I m_I) + \frac{1}{8}\frac{e^2 B_0^2}{m_e c^2} r^2 \sin^2\theta. \tag{8.7}$$

To find the eigenvalues, a diagonalization of the Hamiltonian including all states with $10 \leq n \leq 60$ is required. Details of this diagonalization are contained in [31]. The eigenvalues are in good agreement with Rydberg levels found experimentally in a 1-T field (to within a few GHz up to $n = 47$).

8.2.2.3 Detection of Cs Excitation

An InGaAs photodiode is mounted near the Cs excitation region in Figure 8.4 to detect fluorescence from the $6P_{3/2}$ state. This fluorescence is used to ensure that the 852-nm laser is correctly tuned, and to monitor the Cs beam intensity. Figure 8.8 shows a measurement of this fluorescence as the Cs oven is heated.

After the radiation baffles, but before the electrode stack, a Stark-ionization detector (Figure 8.4) is used to monitor the number of Rydberg Cs created. A voltage of +60 or −60 V is applied to the top electrode of the Stark-ionization detector to create a +300 or −300 V/cm field. This field is large enough to Stark-ionize the $nD_{5/2}$ ($n > 32$) states. The current due to the ionized Cs^+ or the freed e^- is then measured on the bottom electrode. Figure 8.9 shows the signal from the Stark-ionization detector as Rydberg Cs passes through it and the applied voltage is tuned between −60 and +60 V to detect both Cs^+ (at positive voltages) and e^- (at negative voltages).

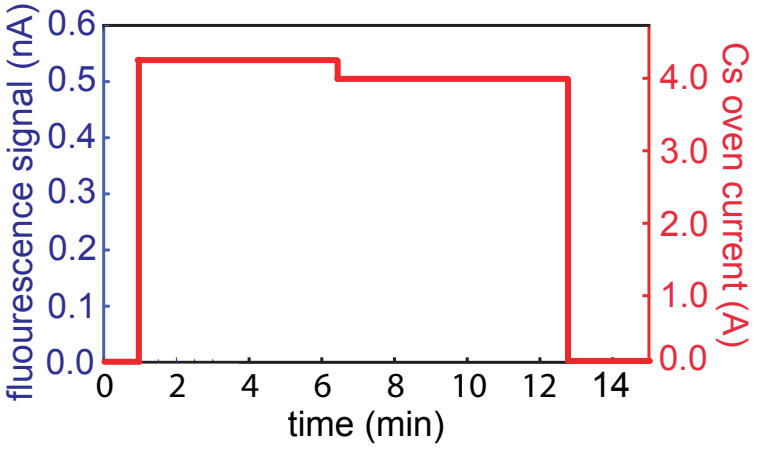

FIGURE 8.8: Detected fluorescence indicating the intensity of the Cs beam, and that the the $6S_{1/2}$ to $6P_{3/2}$ transition is being driven.

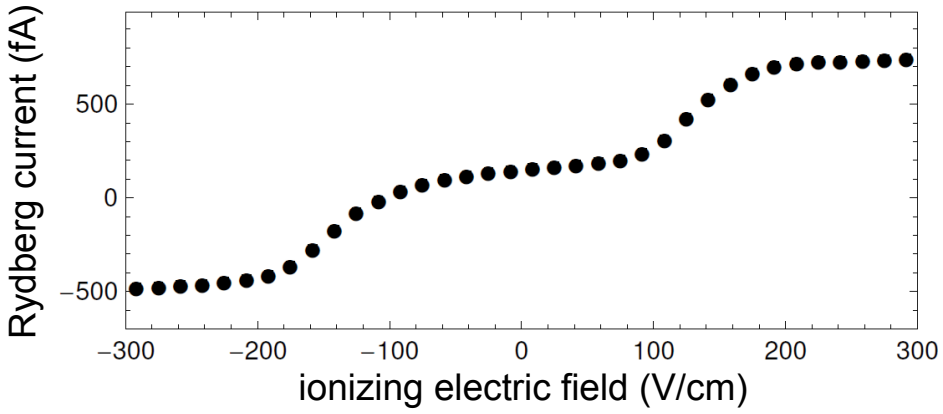

FIGURE 8.9: Ionization signal indicating the production of Rydberg Cs atoms. Figure from [30].

8.2.3 Positronium Production

To produce Rydberg Cs, for Rydberg Ps, the first step is to tune the laser frequencies to maximize the fluorescence (Figure 8.8) detected at the InGaAs diode in Figure 8.4. The 852-nm laser is tuned to resonance with the $6S_{1/2}$ $m_J = 1/2$ m_I - to - $6P_{3/2}$ $m_J = 3/2$ m_I transition by maximizing the fluorescence approximately 6 minutes after applying heat to the Cs source. With this laser tuned, the signal from the Stark-ionization detector (Figure 8.4 and Figure 8.9) is monitored to find the optimal frequency for the 511-nm laser. Once the peak frequencies are found, the Cs oven is turned off and the electrode stack is given 5 minutes to cool back down to 1.2 K.

After the electrode stack is cooled, 3×10^7 e^+ are loaded into the cryogenic Penning trap using the method outlined in Section 7.4. The upper-stack rotating wall is used to radially compress the e^+ plasma to approximately 4.5 mm, as described in Section 7.1.2. The potential structure used for Rydberg Ps production is shown in Figure 8.10. Several factors influence the choice of potential structure. The e^+ plasma is confined by a harmonic potential well which is centered on the electrode through which Rydberg Cs will enter the electrode stack, as shown in Figure 8.10. This potential well is designed such that 0 V is applied to the center electrode,

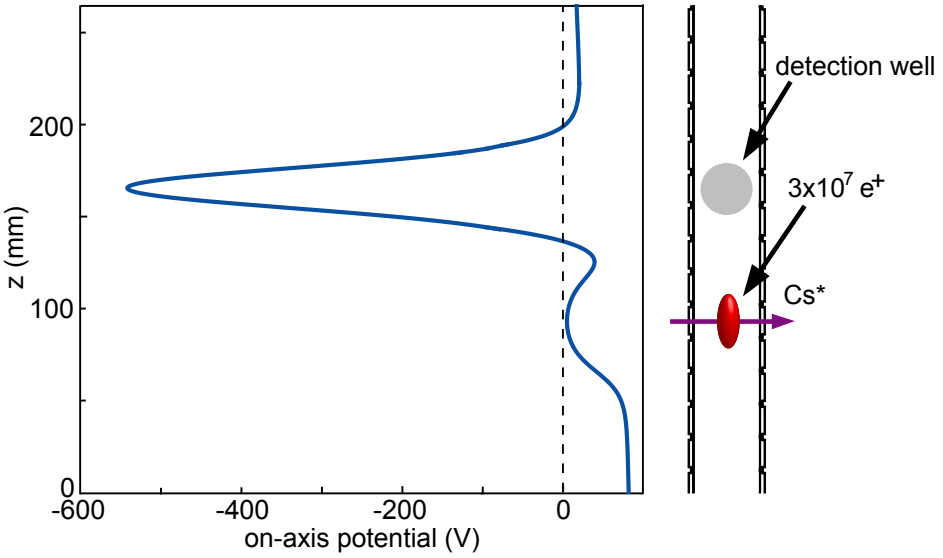

FIGURE 8.10: On-axis potential well structure used to hold e^+ and produce Rydberg Ps.

thereby avoiding the possibility of Stark-ionizing the incoming Rydberg Cs by the radial electric field due to this applied potential. The depth of the potential well is made as shallow as possible to prevent its electric field from ionizing the outgoing Rydberg Ps atoms.

The harmonicity of the potential affects radial expansion of the e^+ plasma during the experiment. If the plasma radius increases over the course of the experiment, then the e^+ plasma density decreases, thereby decreasing the Rydberg Ps production rate. Figure 8.11 shows the radial expansion of a e^+ plasma held in the harmonic well in Figure 8.10, compared to a e^+ plasma held in a 100-V single-electrode well, indicating that a harmonic well is needed to avoid expansion.

The Cs oven is heated a second time, and the excitation lasers again excite the Cs atoms to a Rydberg state. The Rydberg Cs beam enters the electrode stack and undergoes a charge exchange within the e^+ plasma, producing Rydberg Ps. Some Rydberg Ps will travel axially towards the 550-V-deep detection well (Figure 8.10). The detection well subtends a small solid angle (approximately $\pi/8$ sr — comparable to the solid angle that can be subtended by the $\bar{p}$ plasma when producing $\overline{H}$

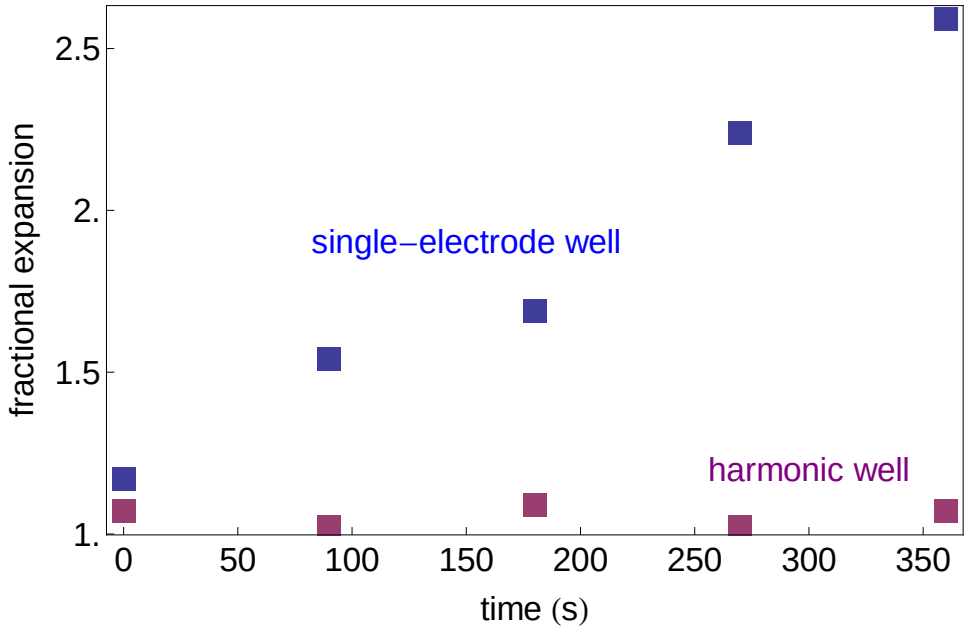

FIGURE 8.11: The fractional increase of the e^+ plasma radius while the plasma is held in a single-electrode, 100-V deep well (blue) and a multi-electrode harmonic well (purple).

by two-stage charge exchange). The Rydberg Ps are ionized by the large electric field in the 550-V-deep detection well and the e^+ is trapped within this well. The potential structure is designed so that the e^- from the ionized Rydberg Ps are accelerated towards the bottom of the electrode stack. This potential structure avoids the situation in which the e^- are allowed to make multiple passes through the e^+ plasma, which could result in collisions between e^+ and e^- that heat the e^+. Such heating could dramatically reduce the cross section of the charge-exchange process if the relative speed of the e^+ increases above the speed of the Rydberg e^- of the Cs atom [99].

At the end of the trial, any e^+ in the detection well are directed towards the degrader at the bottom of the Penning-trap electrode stack. Resulting 511-keV photons are counted using the scintillating fiber detectors discussed in Section 4.2.2. Figure 8.12 shows the deduced number of Rydberg Ps (the fiber counts times 203, as discussed in Section 4.2.2) for different durations of the Rydberg Cs beam. At

first, the number of Rydberg Ps increases linearly with time. Rydberg Ps production then levels off, as the e^+ in the holding well are depleted. The longest trials result in approximately 7.5×10^5 Rydberg Ps atoms detected, indicating a total of 2.6×10^7 Rydberg Ps in 4π sr (assuming an isotropic distribution).

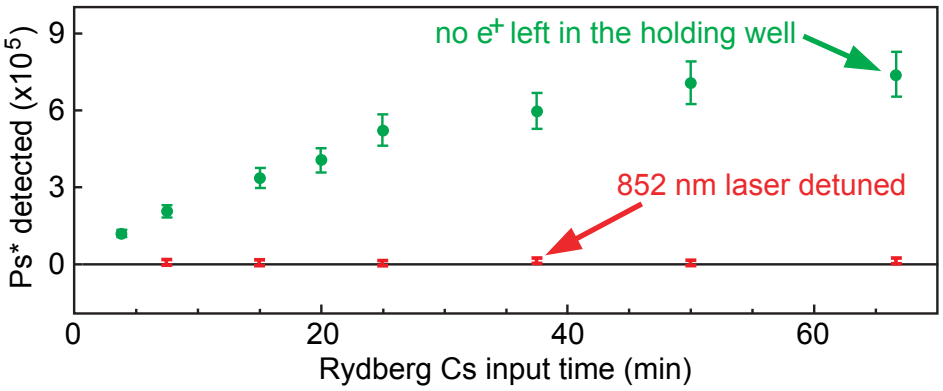

FIGURE 8.12: Rydberg Ps production results as a function of Rydberg Cs input time. Figure from reference [31]. The number of detected Rydberg Ps is deduced from the fiber counts seen when e^+ (from Stark-ionized Rydberg Ps) annihilate on the degrader at the bottom of the cryogenic Penning trap.

Control trials are performed with the 852-nm detuned, but with all other experiment parameters kept the same. For these control trials, the Cs enters the electrode stack in the ground state. The cross section for charge exchange of ground-state Cs is approximately 7 orders of magnitude smaller than that of $n = 42$ Cs. As expected, and as shown in Figure 8.12, these control trials do not result in any e^+ captured in the ionizing detection well.

8.2.4 Antihydrogen Production and Detection

The first step in $\overline{H}$ production via two-stage charge exchange is to load 5×10^6 $\bar{p}$ into the cryogenic Penning trap using the methods outlined in Chapter 7. The $\bar{p}$ are held in the lower part of the electrode stack while the Cs source is heated and the lasers are tuned to produce Rydberg Cs. Once the lasers are tuned, the current to the Cs source is turned off and the trap is allowed to cool for 5 minutes.

Once the trap has cooled, 300×10^6 e^+ are loaded into the cryogenic Penning trap and compressed to a radius of approximately 4.5 mm.

The $\bar{p}$ and e^+ are confined in the potential structure shown in Figure 8.13. The structure of this nested potential is influenced by the same factors that influence the potential structure used in Rydberg Ps production. The added $\bar{p}$ potential well is made harmonic and shallow to avoid $\bar{p}$ radial expansion and the Stark-ionization of Rydberg Ps and of Rydberg $\overline{H}$. The $\bar{p}$ are held as close to the e^+ as possible to maximize the number of Rydberg Ps atoms that enter the $\bar{p}$ cloud.

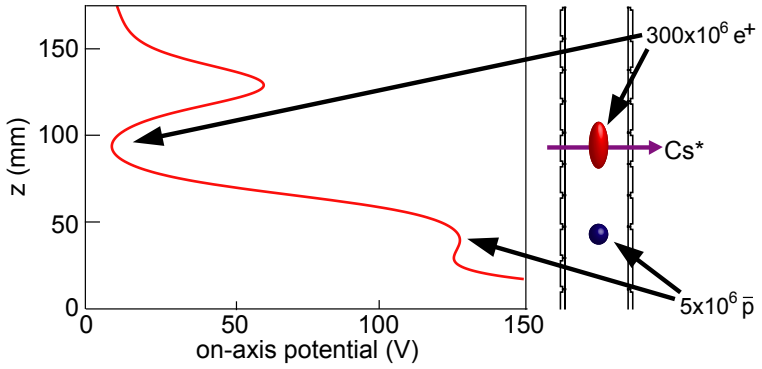

FIGURE 8.13: On-axis potentials used to hold 3×10^8 e^+ and 5×10^6 $\bar{p}$ for $\overline{H}$ production using two-stage charge exchange.

As in the Rydberg Ps production method, the Cs source is operated at a current of between 4 and 5 A for 6 minutes, after which the applied current is decreased by 0.25 A for the remainder of the experiment. The excitation lasers are admitted to create Rydberg Cs atoms that enter the electrode stack and undergo the first charge exchange, creating an isotropic distribution of Rydberg Ps. Some of these Rydberg Ps atoms travel axially down the electrode stack (Figure 8.13) and undergo a second charge exchange in the cloud of $\bar{p}$ to create $\overline{H}$. Since the momentum distributions of the e^+ and $\bar{p}$ are expected to be approximately isotropic, the $\overline{H}$ exit the $\bar{p}$ cloud with an approximately isotropic angular distribution. The $\overline{H}$ are neutral, and, therefore, not bound by the electrostatic potentials holding the charged particles. For these initial experiments, the Ioffe magnet is not energized, allowing the $\overline{H}$ to travel to the electrode stack walls, where they annihilate.

The $\bar{p}$ annihilations are easily detected by the scintillating paddles and fibers discussed in Section 3.1.5. The Trigger-1 data, as discussed in Section 4.5, is analyzed using a set of twelve criteria developed by Dr. Robert McConnell [30]. Each of these criteria have an associated merit rating which reflects how well that criteria differentiates between an $\bar{p}$ annihilation events and cosmic-ray background events. Using a high merit rating results in fewer accepted $\bar{p}$ events in return for a reduced cosmic-ray background count rate. We use a merit rating which results in a 40% detection efficiency for $\bar{p}$ annihilations and a background count rate of 2 Hz.

During the $\overline{H}$ production, the 852-nm laser beam is chopped (at a frequency of 9.3 Hz or 117 Hz), as shown by the chopper wheel in Figure 8.6. Chopping this laser modulates the production of Rydberg Cs atoms that enter the electrode stack, thus modulating $\overline{H}$ production. The difference between the number of $\bar{p}$ counts when Cs is in the ground-state (N_{off}) and the number of $\bar{p}$ counts when the Cs is in the Rydberg state (N_{on}) is defined to be ΔN, the number of excess $\bar{p}$ counts .

The $\bar{p}$ counts from a single two-stage charge exchange trial with 9.3-Hz chopper-wheel frequency are shown in Fig 8.14. Figure 8.14(a) shows the number of $\bar{p}$ counts ($N_{on} + N_{off}$) in 150-s time bins. Figure 8.14(b) shows the cumulative number of $\bar{p}$ counts ($N_{on} + N_{off}$) after each 150-s time bin. Figure 8.14(c) shows the number of excess $\bar{p}$ counts (ΔN) in 150-s time bins. Figure 8.14(d) shows the cumulative number of excess $\bar{p}$ counts (ΔN) after each 150-s time bin. The uncertainty in the number of $\bar{p}$ counts in Figure 8.14(c) and (d) is the square root of the total number of counts ($N_{on} + N_{off}$) in the binned and cumulative cases, respectively.

Towards the end of the run in Figure 8.14, the N_{off} $\bar{p}$ count rate accelerates. This phenomena, which is due to $\bar{p}$ escaping their potential well, is attributed to decreased cooling capacity of the 1-K Pot (Section 3.1.3) that was particular to

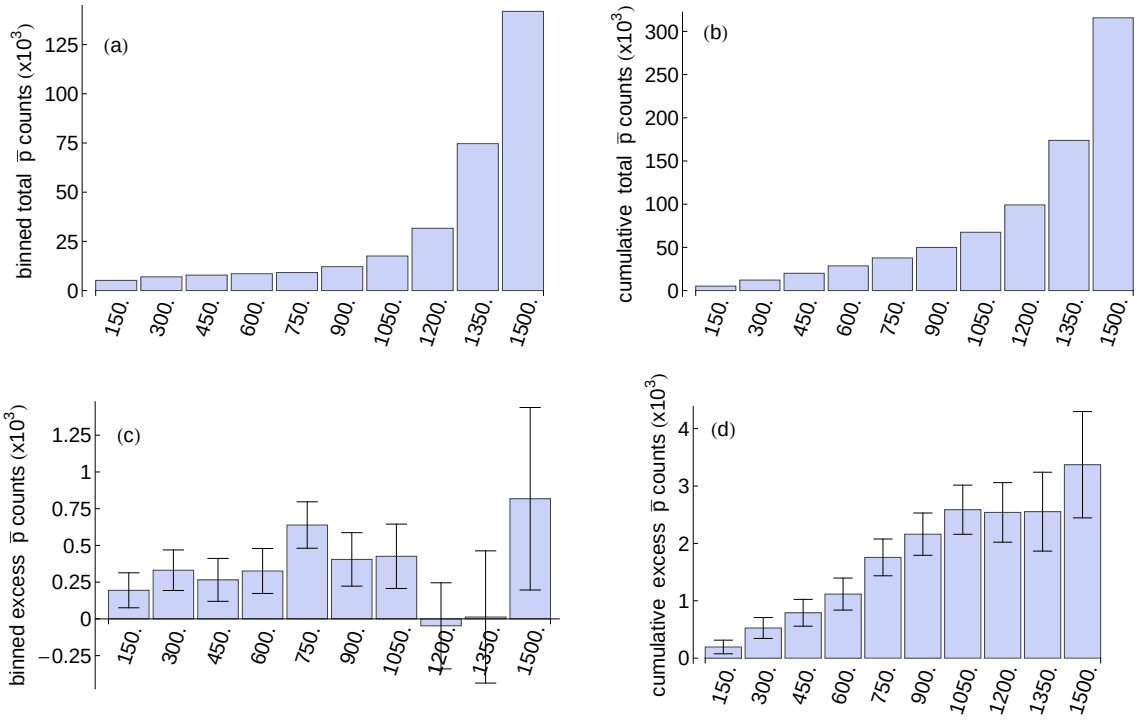

FIGURE 8.14: The results from a single two-stage charge exchange trial with 9.3-Hz chopper-wheel frequency. The total number of $\bar{p}$ counts (total of when the 852-nm laser is off and on) per 150-s bin (a). The cumulative total of $\bar{p}$ counts (b). The number of excess $\bar{p}$ counts per 150-s bin (c). The cumulative number of excess $\bar{p}$ counts (d).

the 2011 beam run. Two-stage charge exchange trials from 2010 ran the Cs source for over 2400 s before the temperature increased by 0.4 K [30] — an increase that took place in 2011 after only 1560 s (Figure 8.5).

Increased $\bar{p}$ losses lead to a larger total number of $\bar{p}$ detected, thereby increasing the uncertainty in ΔN. It is difficult to determine if there are any excess $\bar{p}$ counts during the last 450 s of the trial shown in Figure 8.14. Therefore, only the data from the first 1200 s of each trial is used to determine the number of excess $\bar{p}$ counts.

The same control-trial method used for Rydberg Ps production is used here. The 852-nm laser is detuned so that ground-state Cs enters the electrode stack instead of Rydberg Cs. As was demonstrated in the Rydberg Ps trials, these control trials result in no Rydberg Ps formation, and so no $\overline{H}$ formation is expected: the number

of excess $\bar{p}$ counts (ΔN) should be zero. This result is confirmed experimentally, as summarized by the red points in Figure 8.15 and discussed in Section 8.2.5.

8.2.5 Discussion of Results

During the 2010 and 2011 beam runs, we completed 11 two-stage charge exchange trials (Figure 8.15). Six trials (three trials with a 9.3-Hz chopper-wheel frequency and three trials with a 117-Hz chopper-wheel frequency) produced excess $\bar{p}$ counts (an average of 2000 $\bar{p}$ counts per 1200-s trial) and five control trials that did not produce excess $\bar{p}$ counts. The number of excess $\bar{p}$ counts when using either chopper-wheel frequency is consistent. Therefore, the mechanism that creates excess $\bar{p}$ counts is correlated with Rydberg Cs entering the electrode stack. This mechanism also turns on and off much faster than the time constant of either laser-modulation frequency ($(9.3\text{ Hz})^{-1} = 108$ ms and $(117\text{ Hz})^{-1} = 8.5$ ms).

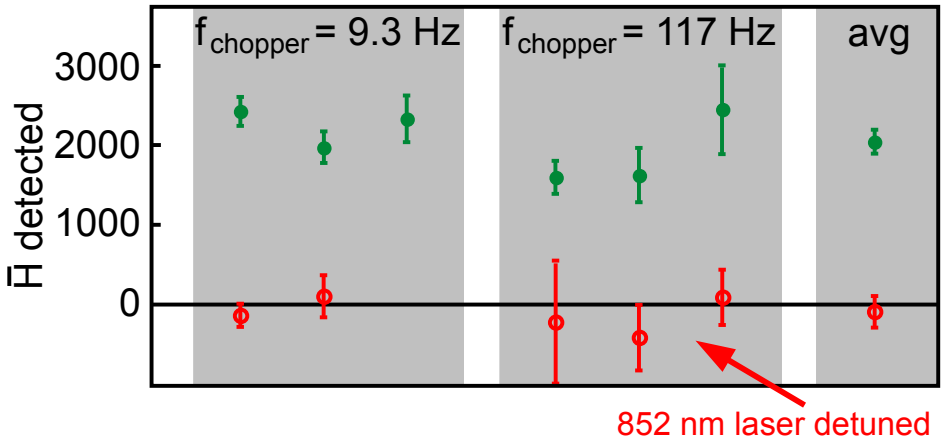

FIGURE 8.15: $\bar{H}$ production results using two different chopper frequencies. An average of approximately 2000 $\bar{H}$ atoms are produced, per trial.

The operation of the Cs source as a heating mechanism of the electrodes and of the $\bar{p}$ inside these electrodes is ruled out immediately due to the long time

scale associated with heating and cooling the cryogenic Penning trap, as shown in Figure 8.5. Thus, this heating cannot cause our excess $\bar{p}$ counts.

Another potential mechanism caused by Rydberg Cs entering the cryogenic Penning trap electrode stack is due to e^- and e^+ from ionized Ps. These particles could gain energy if they are accelerated by parts of the nested potential well. The hot e^- or e^+ could heat the $\bar{p}$, giving them enough energy to escape the very shallow potential well that holds them. This mechanism activates quickly, with a time constant of approximately 10 ms [26], and $\bar{p}$ losses would correlate with Rydberg Cs entering the cryogenic Penning trap electrode stack. The hot e^- and e^+ must cool by synchrotron radiation, which has a time constant of 2.6 s in a 1-T field. This time constant is much longer than the period at either chopper-wheel frequency, thus ruling out e^- and e^+ heating as a mechanism that would result in excess $\bar{p}$ counts.

The results of the two-stage charge-exchange experiments are easily explained by the production of $\overline{H}$. Antihydrogen production would be correlated with Rydberg Cs entering the electrode stack and producing an isotropic distribution of Rydberg Ps, as discussed in Section 8.2.3, when using either chopper-wheel frequency. The control trials would not produce $\overline{H}$ since Rydberg Ps is not produced when the 852-nm laser is detuned. The Rydberg Cs atoms require approximately 200 μs to travel between the laser-excitation region and the center of the electrode stack, which is much less than the time constant associated with either chopper-wheel frequency. Therefore, $\overline{H}$ will be produced when the 852-nm laser passes through the chopper wheel and $\overline{H}$ production will cease when the 852-nm laser is blocked by the chopper wheel.

Therefore, we attribute the excess $\bar{p}$ counts to $\overline{H}$ atoms that are produced in the cryogenic Penning trap electrode stack and annihilate on the surface of the electrode-stack. An average of approximately 2000 $\overline{H}$ per 1200-s trial are detected

using either chopper frequency (Figure 8.15). Since the laser is blocked 50% of the time and data during the turning on and off of the laser is discounted (approximately 5% of data), the 2000 $\overline{\mathrm{H}}$ are produced within a time window of 540 s per trial. Summing over all trials, more than 1.2×10^4 $\overline{\mathrm{H}}$ atoms were detected.

Chapter 9

Conclusions

Before I began my work at the AD, ATRAP had already demonstrated the ability to hold charged particles and produce $\overline{\mathrm{H}}$ in a Penning-Ioffe field [105], [106], though no trapped $\overline{\mathrm{H}}$ were detected. ATRAP had also demonstrated the feasibility of laser-controlled, two-stage charge-exchange $\overline{\mathrm{H}}$ production, detecting 20 $\overline{\mathrm{H}}$ per trial [101]. The focus of my work at ATRAP was to greatly increase the number of e^+ available for experiments in the cryogenic Penning trap and to use those e^+ to produce larger numbers of $\overline{\mathrm{H}}$ via laser-controlled, two-stage charge exchange.

Advancements in particle loading and counting techniques are where a majority of my contributions lay. Many facets of the neon moderator and gas-buffer accumulator have been studied and optimized. The rate at which slow e^+ exit the surface of the frozen-neon moderator on the ^{22}Na source has been increased by more than a factor of two. The slow e^+ rate has been measured experimentally for the first time using precisely-calibrated numbers of accumulated e^+. The e^+ accumulation rate in the room-temperature positron accumulator has increased by more than a factor of two as a direct result of the increased slow e^+ rate. The e^+ loading rate into the cryogenic Penning trap has been increased by a factor of four, due to the increased slow e^+ rate, and increased e^+ transfer and e^- cooling efficiencies.

parameter	previous value	current value	unit
slow e^+ rate	1.2×10^5	2.60×10^5	e^+/s/mCi
e^+ accumulation rate	2.1×10^4	4.4×10^4	e^+/s/mCi
e^+ trapping rate	5.3×10^3	2.4×10^4	e^+/s/mCi
total e^+ trapped	3.5×10^8	4.0×10^9	e^+

TABLE 9.1: Summary of e^+ results.

Table 9.1 displays a summary of positron-related rates and values that have been improved during the course of my work. Larger numbers of e^+ can be attained at a faster rate than previously possible, increasing the frequency of $\overline{H}$ production and trapping experiments.

The rotating wall of the cryogenic Penning trap is used to radially compress e^+ plasmas. This rotating wall is an important instrument in loading and controlling e^+ plasmas. It is used to periodically compress growing e^+ plasmas, making it possible to load 4.0×10^9 e^+ into the cryogenic Penning trap — the largest number of e^+ held in a single Penning trap.

Positron and electron charge-counting techniques in the cryogenic Penning trap have been compared using identical plasmas of each species. Despite very different processes occurring when e^+ or e^- hit the surface of a Faraday cup, the experiments indicate that appropriately biasing the Faraday cup results in accurate particle counting. Measurements of the center-of-mass and quadrupole plasma mode frequencies, along with the number of particles in the plasma, are used to completely parameterize e^+ plasmas in the cryogenic Penning trap. This measurement technique is used to determine the radius of a e^+ plasma, as well as to measure changes in the e^+ plasma temperature. Precise knowledge of the $\bar{p}$ and e^+ plasma geometries, densities, and temperatures will allow for the optimization of $\overline{H}$ production techniques.

Antihydrogen is produced via three-body recombination and trapped in the cryogenic Penning-Ioffe trap. An average of 5 ± 1 $\overline{H}$ atoms trapped per trial. The $\overline{H}$

remained confined in the Penning-Ioffe trap for up to 1000 s — long enough to ensure radiative decay to the ground state.

Two-stage charge exchange is used to create $\overline{\mathrm{H}}$ without directly heating the $\bar{\mathrm{p}}$. This process creates $\overline{\mathrm{H}}$ that should be more easily trapped in a Ioffe trap compared to $\overline{\mathrm{H}}$ created via three-body recombination. A total of 11 two-stage charge exchange trials were performed (6 trials that produced $\overline{\mathrm{H}}$ and 5 control trials). Two-stage charge exchange trials produced just over 2000 $\overline{\mathrm{H}}$ atoms per trial (over 1.2×10^4 $\overline{\mathrm{H}}$ atoms in total). These results are important steps towards the long-term goal of precise spectroscopic measurements of $\overline{\mathrm{H}}$.

Though not thoroughly discussed in this thesis, during my time at ATRAP, I played a part in many other scientific results. The 2010 beam run saw several important leaps forward in our understanding of the $\bar{\mathrm{p}}$ plasmas we use to produce $\overline{\mathrm{H}}$. The centrifugal separation of $\bar{\mathrm{p}}$ and e^- was demonstrated [27], which was the first demonstration of centrifugal separation using elementary particles. Antiproton temperatures were determined by monitoring the $\bar{\mathrm{p}}$ loss rate as the confining potential was reduced. It was discovered that $\bar{\mathrm{p}}$ do not cool to the temperature of the electrode-stack walls. The steady-state $\bar{\mathrm{p}}$ temperature (17 K) was reduced to at least 3.5 K via adiabatic cooling [26]. In 2012, an apparatus used to measure the magnetic moment of a single proton was shipped to CERN to perform the same measurement using an $\bar{\mathrm{p}}$. The apparatus was installed over a vacant $\bar{\mathrm{p}}$ extraction line. I prepared the diagnostics and energy-tuning cell of the extraction line and maintained these instruments over the course of the 2012 beam run. The experiment was a success, determining the $\bar{\mathrm{p}}$ magnetic moment to a precision of 4.4 parts per million — 680 times smaller than previously realized. All of 2013 and 2014 were spent constructing and testing the next generation of cryogenic Penning-Ioffe trap and Rydberg Cs apparatus used in two-stage charge exchange. After two iterations of Ioffe-trap enclosure, the completed apparatus was successfully cooled to cryogenic temperatures at the end of 2014. The Ioffe trap was operated at

full current and e^- plasmas were loaded and moved throughout the lower part of the Penning trap electrode stack. My hope is that even though my work on this new cryogenic Penning-Ioffe trap has not resulted in any scientific results thus far, the stage is set for many fruitful years of research for future ATRAP graduate students.

The future of $\overline{\mathrm{H}}$ physics in ATRAP is bright, but there is still much work to do. Antihydrogen atoms produced via three-body recombination have been trapped in a combined Penning-Ioffe field, but more than 5 atoms per trial would be desirable for precise spectroscopic results. Antihydrogen production via two-stage charge exchange has been demonstrated as an efficient method of $\overline{\mathrm{H}}$ production. If this process can be performed in a combined Penning-Ioffe trap, it could lead to large numbers of trapped $\overline{\mathrm{H}}$ by taking advantage of the large numbers of cold $\bar{\mathrm{p}}$ that ATRAP can now produce. With a new cryogenic Penning-Ioffe trap and the imminent arrival of even lower-energy $\bar{\mathrm{p}}$ from the Extra-Low ENergy Antiproton ring (ELENA), ATRAP may soon be performing precision spectroscopic measurements using large numbers of trapped $\overline{\mathrm{H}}$ atoms.

Bibliography

[1] Gerhart Lueders. Proof of the tcp theorem. *Ann. Phys.*, 281(1-2):1004, April 1957. URL http://dx.doi.org/10.1006/aphy.2000.6027.

[2] K.A. Olive et al (Particle Data Group). 2014 review of particle physics. *Chin. Phys. C*, 38:090001, 2014. URL http://pdg.lbl.gov/index.html.

[3] C.D. Anderson. The positive electron. *Phys. Rev.*, 43(6):491, March 1933. URL http://link.aps.org/doi/10.1103/PhysRev.43.491.

[4] P.B. Schwinberg, R.S. Van Dyck Jr., and H.G. Dehmelt. New comparison of the positron and electron g factors. *Phys. Rev. Lett.*, 47(24):1679, December 1981. URL http://link.aps.org/doi/10.1103/PhysRevLett.47.1679.

[5] O. Chamberlain, E. Segre, C. Wiegand, and T. Ypsilantis. Observation of antiprotons. *Phys. Rev. Lett.*, 100(3):947, November 1955. URL http://link.aps.org/doi/10.1103/PhysRev.100.947.

[6] G. Gabrielse, X. Fei, K. Helmerson, S.L. Rolston, R. Tjoelker, A. Trainor, H. Kalinowsky, J. Haas, and W. Kells. First capture of antiprotons in a penning trap: A kiloelectronvolt source. *Phys. Rev. Lett.*, 57(20):2504, November 1986. URL http://link.aps.org/doi/10.1103/PhysRevLett.57.2504.

[7] G. Baur et al. Production of antihydrogen. *Phys. Lett. B*, 368(3):251, February 1996. URL http://dx.doi.org/10.1016/0370-2693(96)00005-6.

[8] G Gabrielse, N.S Bowden, P Oxley, A Speck, C.H Storry, J.N Tan, M Wessels, D Grzonka, W Oelert, G Schepers, T Sefzick, J Walz, H Pittner, T.W Hänsch, and E.A Hessels. Stacking of cold antiprotons. *Phys. Lett. B*, 548(3): 140, November 2002. URL http://dx.doi.org/10.1016/S0370-2693(02)02850-2.

[9] G. Gabrielse, N.S. Bowden, P. Oxley, A. Speck, C.H. Storry, J.N. Tan, M. Wessels, D. Grzonka, W. Oelert, G. Schepers, T. Sefzick, J. Walz, H. Pittner, T.W. Hänsch, and E.A. Hessels. Background-free observation of cold antihydrogen with field-ionization analysis of its states. *Phys. Rev. Lett.*, 89(21):213401, October 2002. URL http://link.aps.org/doi/10.1103/PhysRevLett.89.213401.

[10] M. Amoretti et al (ATHENA Collaboration). Production an detection of cold antihydrogen atoms. *Nature*, 419:456, September 2002. URL http://www.nature.com/nature/journal/v419/n6906/abs/nature01096.html.

[11] G.B. Andresen et al(ALPHA Collaboration). Trapped antihydrogen. *Nature Lett.*, 468:673, March 2010. URL http://www.nature.com/nature/journal/v468/n7324/full/nature09610.html.

[12] G. Gabrielse, R. Kalra, W. S. Kolthammer, R. McConnell, P. Richerme, D. Grzonka, W. Oelert, T. Sefzick, M. Zielinski, D. W. Fitzakerley, M. C. George, E. A. Hessels, C. H. Storry, M. Weel, A. Muellers, and J. Walz. Trapped antihydrogen in its ground state. *Phys. Rev. Lett.*, 108(11):113002, March 2012. URL http://link.aps.org/doi/10.1103/PhysRevLett.108.113002.

[13] C. Amole et al (ALPHA Collaboration). Resonant quantum transitions in trapped antihydrogen atoms. *Nature Lett.*, 483:439, March 2012. URL http://www.nature.com/nature/journal/v468/n7324/full/nature09610.html.

[14] S. Pakvasa, W.A. Simmons, and T.J. Weiler. Test of equivalence principle for neutrinos and antineutrinos. *Phys. Rev. D*, 39(6):1761, March 1989. URL http://link.aps.org/doi/10.1103/PhysRevD.39.1761.

[15] G. Gabrielse, A. Khabbaz, D.S. Hall, C. Heimann, H. Kalinowsky, and W. Jhe. Precision mass spectroscopy of the antiproton and proton using simultaneously trapped particles. *Phys. Rev. Lett.*, 82(16):3198, April 1999. URL http://link.aps.org/doi/10.1103/PhysRevLett.82.3198.

[16] R.J.Hughes and M.H. Holzscheiter. Constraints on the gravitational properties of antiprotons and positrons from cyclotron-frequency measurements. *Phys. Rev. Lett.*, 66(7):854, February 1991. URL http://link.aps.org/doi/10.1103/PhysRevLett.66.854.

[17] S.G. Karshenboim. A constraint on antigravity of antimatter from precision spectroscopy of simple atoms. *Astronomy Letters*, 35:663, October 2009. URL http://link.springer.com/article/10.1134%2FS1063773709100028.

[18] Alpha Collaboration and A.E. Charman. Description and first application of a new technique to measure the gravitational mass of antihydrogen. *Nature Comms.*, 4(1785), April 2013. URL http://www.nature.com/ncomms/journal/v4/n4/ncomms2787/metrics/blogs.

[19] T.D. Hänsch. The hydrogen atom in a new light. *Meth. Laser Spec.*, page 163, 1986. URL http://link.springer.com/chapter/10.1007/978-1-4615-9459-8_22.

[20] C.G. Parthey et al. Improved measurement of the hydrogen 1s-2s transition frequency. *Phys. Rev. Lett.*, 107(20):203001, November 2011. URL http://link.aps.org/doi/10.1103/PhysRevLett.107.203001.

[21] N.F. Ramsey. Experiments with separated oscillatory fields and hydrogen masers. *Rev. Mod. Phys.*, 62:541, July 1990. URL http://dx.doi.org/10.1103/RevModPhys.62.541.

[22] Y. Enomoto et al (ASACUSA Collaboration). Synthesis of cold antihydrogen in a cusp trap. *Phys. Rev. Lett.*, 105(24):243401, December 2010. URL http://link.aps.org/doi/10.1103/PhysRevLett.105.243401.

[23] S. Maury. The antiproton decelerator (ad). *Hyperfine Int.*, 109(1-4):43, August 1997. URL http://link.springer.com/article/10.1023%2FA%3A1012632812327.

[24] J. Estrada, T. Roach, J.N. Tan, P. Yesley, and G. Gabrielse. Field ionization of strongly magnetized rydberg positronium: A new physical mechanism for positron accumulation. *Phys. Rev. Lett.*, 84(5):859, January 2000. URL http://link.aps.org/doi/10.1103/PhysRevLett.84.859.

[25] F.J. Wysocki, M. Leventhal, A. Passner, and C.M. Surko. Accumulation and storage of low energy positrons. *Hyperfine Interactions*, 44(1-4):185–200, March 1989. URL http://link.springer.com/article/10.1007%2FBF02398669?LI=true.

[26] G. Gabrielse, W.S. Kolthammer, R. McConnell, P.Richerme, R. Kalra, E. Novitski, D. Grzonka, W. Oelert, T. Sefzick, M. Zielinski, D. Fitzakerley, M.C. George, E.A. Hessels, C.H. Storry, M. Weel, A. Mullers, and J. Walz. Adiabatic cooling of antiprotons. *Phys. Rev. Lett.*, 106(7):073002, February 2011. URL http://link.aps.org/doi/10.1103/PhysRevLett.106.073002.

[27] G. Gabrielse, W.S. Kolthammer, R. McConnell, P. Richerme, J. Wrubel, R. Kalra, E. Novitski, D. Grzonka, W. Oelert, T. Sefzick, J.S. Borbely, D. Fitzakerley, M.C. George, E.A. Hessels, C.H. Storry, M. Weel, A. Mullers,

J. Walz, and A. Speck. Centrifugal separation of antiprotons and electrons. *Phys. Rev. Lett.*, 105(21):213002, November 2010. URL http://link.aps.org/doi/10.1103/PhysRevLett.105.213002.

[28] J. DiSciacca, M. Marshall, K. Marable, G. Gabrielse, S. Ettenauer, E. Tardiff, R. Kalra, D.W. Fitzakerley, M.C. George, E.A. Hessels, C.H. Storry, M. Weel, D. Grzonka, W. Oelert, and T. Sefzick. One-particle measurement of the antiproton magnetic moment. *Phys. Rev. Lett.*, 110: 130801, March 2013. URL http://dx.doi.org/10.1103/PhysRevLett.110.130801.

[29] W.S. Kolthammer. Antimatter plasmas within a penning-ioffe trap. *Thesis*, 2011.

[30] R.P. McConnell. Laser-controlled charge-exchange production of antihydrogen. *Thesis*, 2011.

[31] A. Muellers. Production of antihydrogen via double charge exchange. *Thesis*, 2012.

[32] F.M. Penning. Die glimmentladung bei niedrigem druck zwischen koaxialen zylindern in einem axialen magnetfeld. *Physica*, 3(9):873, November 1936. URL http://www.sciencedirect.com/science/article/pii/S0031891436803139.

[33] W. Paul. Electromagnetic traps for charged and neutral particles. *Rev. Mod. Phys.*, 62(3):531, 1990. URL http://link.aps.org/doi/10.1103/RevModPhys.62.531.

[34] R.S. Van Dyck Jr., P.B. Schwinberg, and H.G. Dehmelt. New frontiers in high energy physics. 1978.

[35] K. Blaum, Yu.N. Novikov, and G. Werth. Penning traps as a versatile tool for precise experiments in fundamental physics. *Contemporary Physics*, 2009. URL http://arxiv.org/ftp/arxiv/papers/0909/0909.1095.pdf.

[36] F.G. Major, V.N. Gheorghe, and G. Werth. Charged particle traps. *Springer series*, 2005.

[37] G. Gabrielse and F.C. Mackintosh. Cylindrical penning traps with orthogonalized anharmonicity compensation. *Intl. J. of Mass Spec. and Ion Proc.*, 57:1, March 1984. URL http://gabrielse.physics.harvard.edu/gabrielse/papers/1984/CylindricalTrap.pdf.

[38] G. Gabrielse, L. Haarsma, and S.L. Rolston. Open-endcap penning traps for high precision experiments. *Int. Journal of Mass Spectrometry and Ion Processes*, 88(2-3):319, April 1989. URL http://dx.doi.org/10.1016/0168-1176(89)85027-X.

[39] W.H. Wing. On neutral particle trapping in quasistatic electromagnetic fields. *Prog. Quant. Electr.*, 8:181, 1984. URL http://dx.doi.org/10.1016/0079-6727(84)90012-0.

[40] T. Bergeman, G. Erez, and H.J. Metcalf. Magnetostaic trapping fields for neutral atoms. *Phys. Rev. A*, 35(4):1535, February 1987. URL http://pra.aps.org/pdf/PRA/v35/i4/p1535_1.

[41] E. Majorana. Atomi orientati in campo magnetico variabile. *Il Nuovo Cimento*, 9(2):43, February 1932. URL http://link.springer.com/article/10.1007%2FBF02960953.

[42] T.M. Squires, P. Tesley, and G. Gabrielse. Stability of a charged particle in a combined penning-ioffe trap. *Phys. Rev. Lett.*, 86(23):5266, June 2001. URL http://link.aps.org/doi/10.1103/PhysRevLett.86.5266.

[43] G.B. Andresen et al (ALPHA Collaboration. Evaporative cooling of antiprotons to cryogenic temperatures. *Phys. Rev. Lett.*, 105(1):013003, July 2010. URL http://link.aps.org/doi/10.1103/PhysRevLett.105.013003.

[44] D.H.E. Dubin and T.M. O'Neil. Trapped nonneutral plasmas, liquids, and crystals (the thermal equilibrium states). *Rev. Mod. Phys.*, 71(1):2423, January 1999. URL http://link.aps.org/doi/10.1103/RevModPhys.71.87.

[45] D.J. Heinzen, J.J. Bollinger, F.L. Moore, W.M. Itano, and D.J. Wineland. Rotational equilibria and low-order modes of a non-neutral ion plasma. *Phys. Rev. Lett.*, 66(16):2080, April 1991. URL http://link.aps.org/doi/10.1103/PhysRevLett.66.2080.

[46] D.H.E. Dubin. Theory of electrostatic fluid modes in a cold spheroidal non-neutral plasma. *Phys. Rev. Lett.*, 66(16):2080, April 1991. URL http://link.aps.org/doi/10.1103/PhysRevLett.66.2076.

[47] D.H.E. Dubin. Equilibrium and dynamics of uniform density ellipsoidal non-neutral plasmas. *Phys. Fluids B*, 5(2):295, February 1993. URL http://dx.doi.org/10.1063/1.860571.

[48] D.H.E. Dubin. Displacement eigenmodes for cold-fluid and warm-fluid magnetized plasma oscillations. *Physics of Plasmas*, 12:042107, March 2005. URL http://dx.doi.org/10.1063/1.1854153.

[49] R.L. Spencer, S.N. Rasband, and R.R. Vanfleet. Numerical calculation of axisymmetric non-neutral plasma equilibria. *Phys. Fluids B*, 5(12):4267, December 1993. URL http://dx.doi.org/10.1063/1.860594.

[50] J. Wrubel, G. Gabrielse, W.S. Kolthammer, P. Larochelle, R. McConnell, P. Richerme, D. Grzonka, W. Oelert, T. Sefzick, M. Zielinski, J.S. Borbely, M.C. George, E.A. Hessels, C.H. Storry, M. Weel, A. Muellers, J. Walz, and A. Speck. Pumped helium system for cooling positron and electron

traps to 1.2 k. *Nucl. Instr. Meth. A*, 640(1):232, June 2011. URL http://dx.doi.org/10.1016/j.nima.2011.01.030.

[51] Z.D. Zhang, W. Oelert, D. Grzonka, and T. Sefzick. The antiproton annihilation detector system of the atrap experiment. *Chinese Science Bulletin*, 54: 189, January 2009. URL http://link.springer.com/article/10.1007%2Fs11434-008-0536-6.

[52] D.J. Heinzen, J.J. Bollinger, F.L. Moore, W.M. Itano, and D.J. Wineland. Rotational equilibria and low-order modes of a non-neutral ion plasma. *Phys. Rev. Lett.*, 66(16):2080, April 1991. URL http://prl.aps.org/pdf/PRL/v66/i16/p2080_1.

[53] M.D.Tinkle, R.G.Greaves, and C.M.Surko. Low-order longitudinal modes of single-component plasmas. *Phys. Plasmas*, 2(8):2880, August 1995. URL http://dx.doi.org/10.1063/1.871188.

[54] A.Speck, G. Gabrielse, P. Larochelle, D. LeSage, B. Levitt, W.S. Kolthammer, R. McConnell, J. Wrubel, D. Grzonka, W. Oelert, T. Sefzick, Z. Zhang, D. Comeau, M.C. George, E.A. Hessels, C.H. Storry, W. Weel, and J. Walz. Density and geometry of single component plasmas. *Phys. Lett. B*, 650:119, June 2007. URL http://www.sciencedirect.com/science/article/pii/S0370269307004285.

[55] M. Amoretti et al (ATHENA Collaboration). Positron plasma diagnostics and temperature control for antihydrogen production. *Phys. Rev. Lett.*, 91 (5):055001, August 2003. URL http://prl.aps.org/abstract/PRL/v91/i5/e055001.

[56] A. Speck. Two techniques produce slow antihydrogen. *Thesis*, 2005.

[57] A.H. Weiss and K.F. Canter. Positron stimulated secondary electron emission from cu(100). *Proceedings on the 6th International Conference on Positron Annihilation*, page 162, April 1982.

[58] C. Amsler. Proton-antiproton annihilation and meson spectroscopy with the crystal barrel. *Rev. Mod. Phys.*, 70(4):1293–1339, October 1994. URL http://dx.doi.org/10.1103/RevModPhys.70.1293.

[59] D.L. Eggleston, C.F. Driscoll, B.R. Beck, A.W. Hyatt, and J.H. Malmberg. Parallel energy analyzer for pure electron plasma devices. *Phys. Fluids B*, 4:3432, October 1992. URL http://dx.doi.org/10.1063/1.860399.

[60] P. Richerme. Trapped antihydrogen in its groundstate. *Thesis*, 2012.

[61] T.J. Murphy and C.M. Surko. Positron trapping in an electrostatic well by inelastic collisions with nitrogen molecules. *Phy. Rev. A*, 46(9), November 1992. URL http://pra.aps.org/abstract/PRA/v46/i9/p5696_1.

[62] R.G. Greaves and C.M. Surko. Inward transport and compression of a positron plasma by a rotating electric field. *Phys. Rev. Lett.*, 85(4), August 2000. URL http://prl.aps.org/abstract/PRL/v85/i9/p1883_1.

[63] C.M. Surko. the buffer-gas positron accumulator and resonances in positron-molecule interactions. 2007. URL http://ntrs.nasa.gov/search.jsp?R=20080040755.

[64] Richard B. Firestone. Lbnl isotopes project nuclear data dissemination home page. March 2002. URL http://ie.lbl.gov/toi.html.

[65] R. Krause-Rehberg, L. Buettner, F. Boerner, and N. van der Walt. A ^{22}na source capsule for use in uhv. URL http://positron.physik.uni-halle.de/poster/Poster_SLOPOS9.pdf.

[66] V.A. Kuzminikh, I.A. Tsekhanovski, and S.A. Vorobiev. Backscattering of positrons from thick targets. *Nucl. Instr. Meth.*, 118(1):269–271, June 1974. URL http://www.sciencedirect.com/science/article/pii/0029554X74907150.

[67] P.G. Coleman, L. Albrecht, K.O. Jensen, and A.B. Walker. Backscattering of positrons from thick targets. *J. Phys. Condens. Matter*, 4(50):10311–10322, June 1992. URL http://iopscience.iop.org/0953-8984/4/50/018.

[68] G.R. Massoumi, Peter J. Schultz, W.N. Lennard, and J. Ociepa. Positron emission yields for encapsulated 22na sources. *Nucl. Instr. and Meth. in Physics Research B*, 30(4):592–597, April 1988. URL http://www.sciencedirect.com/science/article/pii/0168583X8890136X.

[69] H.Huomo, R. Jones, J. Hurst, A. Vehanen, J. Throwe, S.G. Usmar, and K.G. Lynn. Deposition and characterization of 22na sources for use with monoenergetic positron neams. *Nucl. Instr. and Meth. in Physics Research A*, 284: 359, 1989. URL http://www.sciencedirect.com/science/article/pii/0168900289903021.

[70] K.F. Canter, P.G. COleman, T.C. Griffith, and G.R. Heyland. Measurement of total cross sections for low energy positron-helium collisions. (positron backscattering from metal surface). *J Phys. B: At. Mol. Phys.*, 5, August 1972. URL http://apl.aip.org/resource/1/applab/v57/i22/p2374_s1.

[71] T.S. Stein, W.E. Kauppila, and L.O. Roellig. Near-thermal energy width of moderated high energy positrons. *Phys. Lett.*, 51A(6), April 1975. URL http://www.sciencedirect.com/science/article/pii/0375960175906313.

[72] S. Pendayala and J.Wm. McGowan. A gold moderator surface preparation for increased slow positron yield. *J. Electron Spectr.*, 19(1), 1980. URL http://www.sciencedirect.com/science/article/pii/0368204880800417.

[73] A.P. Mills. Efficient generation of low-energy positrons. *Appl. Phys. Lett.*, 35(5), September 1979. URL http://apl.aip.org/resource/1/applab/v35/i5/p427_s1.

[74] A.P. Mills. further improvements in the efficiency of low-energy positron moderators. *Appl. Phys. Lett.*, 37(7), October 1980. URL http://apl.aip.org/resource/1/applab/v37/i7/p667_s1.

[75] R.J. Wilson and A.P. Mills. Positron and positronium emission from tungsten (111). *Phys. Rev. B*, 27(7), April 1983. URL http://prb.aps.org/abstract/PRB/v27/i7/p3949_1.

[76] P.J. Schultz, K.G. Lynn, W.E. Frieze, and A. Vehanen. Observation of defects associated with the cu/w(110) interface as studied with variable-energy positrons. *Phys. Rev. B*, 27(11), June 1983. URL http://prb.aps.org/abstract/PRB/v27/i11/p6626_1.

[77] B.L. Brown, W.S. Crane, and A.P. Mills Jr. Generation of highly monochromatic positrons using cold moderators. *Appl. Phys. Lett.*, 48(11), March 1986. URL http://apl.aip.org/resource/1/applab/v48/i11/p739_s1.

[78] A.P. Mills, P.M. Platzmann, and B.L. Brown. Slow-positron emission from metal surfaces. *Phys. Rev. Lett.*, 41(15), October 1978. URL http://prl.aps.org/abstract/PRL/v41/i15/p1076_1.

[79] E.M. Gullikson and A.P. Mills Jr. Positron dynamics in rare-gas solids. *Phys. Rev. Lett.*, 57(3):376–378, July 1986. URL http://prl.aps.org/abstract/PRL/v57/i3/p376_1.

[80] N. Schwentner, F.-J. Himpsel, V. Saile, M. Skibowski, W. Steinmann, and E.E. Koch. Photoemission from rare-gas solids: electron energy distributions from the valence bands. *Phys. Rev. Lett.*, 34:528, March 1975. URL http://journals.aps.org/prl/abstract/10.1103/PhysRevLett.34.528.

[81] A. Ore and J.L. Powell. Three-photon annihilation of an electron-positron pair. *Phys. Rev.*, 75(11), June 1949. URL http://prola.aps.org/pdf/PR/v75/i11/p1696_1.

[82] A.P. Mills Jr. and E.M. Gullikson. Solid neon moderator for producing slow positrons. *Phys. Rev. Lett.*, 49(17):1121–1123, October 1986. URL http://apl.aip.org/resource/1/applab/v49/i17/p1121_s1.

[83] R. Khatri, M. Charlton, P. Sferlazzo, K.G. Lynn, A.P. Mills, and L.O. Roellig. Improvement of rare-gas solid moderators by using conical geometry. *App. Phys. Lett.*, 57(22), November 1990. URL http://apl.aip.org/resource/1/applab/v57/i22/p2374_s1.

[84] C.M. Surko, A. Passner, M. Leventhal, and F.J. Wysocki. Bound states of positrons and large molecules. *Phys. Rev. Lett.*, 61(6):1831–1834, October 1988. URL http://prl.aps.org/abstract/PRL/v61/i16/p1831_1.

[85] J.P. Sullivan, J.P. Marler, S.J. Gilbert, S.J. Buckman, and C.M. Surko. Excitation of electronic states of ar, h2, and n2 by positron impact. *Phys. Rev. Lett.*, 87(7), August 2001. URL http://prl.aps.org/abstract/PRL/v87/i7/e073201.

[86] F. Anderegg, E.M. Hollmann, and C.F. Driscoll. Rotating field confinement of pure electron plasmas using trivelpiece-gould modes. *Phys. Rev. Lett.*, 81 (22), November 1998. URL http://prl.aps.org/abstract/PRL/v81/i22/p4875_1.

[87] J.R. Danielson and C.M. Surko. Torque-balanced high-density steady states of single-component plasmas. *Phys. Rev. Lett.*, 94(3), January 2005. URL http://prl.aps.org/abstract/PRL/v94/i3/e035001.

[88] S.J. Gilbert, C. Kruz, R.G. Greaves, and C.M. Surko. Creation of a monoenergetic pulsed positron beam. *App. Phys. Lett.*, 70(15):1944, April 1997. URL http://dx.doi.org/+10.1063/1.118787.

[89] D. Comeau, A. Dror, D.W. Fitzakerley, M.C. George, E.A. Hessels, C.H. Storry, M. Weel, D.Grzonka, W. Oelert, G. Gabrielse, R. Kalra, W.S. Kolthammer, R. McConnell, P. Richerme, A. Mllers, and J. Walz. Efficient transfer of positrons from a buffer-gas-cooled accumulator into an orthogonally oriented superconducting solenoid for antihydrogen studies. *New J. Phys.*, 14, April 2012. URL http://iopscience.iop.org/1367-2630/14/4/045006.

[90] R.D. Dixon and L.A. Lott. Work function of ultrahigh-vacuum-deposited beryllium films. *J. Appl. Phys.*, 40(12), 1969. URL http://jap.aip.org/resource/1/japiau/v40/i12/p4938_s1.

[91] G. Gabrielse, X. Fei, L.A. Orozco, S.L. Rolston, R.L. Tjoelker, T.A. Trainor, J. Haas, H. Kalinowsky, and W. Kells. Barkas effect observed with antiprotons and protons. *Phys. Rev. A*, 40(1):481, July 1989. URL http://pra.aps.org/pdf/PRA/v40/i1/p481_1.

[92] V. Anferov. Energy degrader optimization for medical beam lines. *Nucl. Instr. Meth. A*, 496(1), 2003. URL http://dx.doi.org/10.1016/S0168-9002(02)01625-X.

[93] S.L. Rolston and G. Gabrielse. Cooling antiprotons in an ion trap. *Hyperfine Interact.*, 44:233, 1988. URL http://gabrielse.physics.harvard.edu/gabrielse/papers/1988/CoolingAntiprotonsInIonTrap.pdf.

[94] D. Comeau. Atrap buffer-gas positron accumulator. *Thesis*, 2013.

[95] G. Gabrielse, S.L. Rolston, and L. Haarsma. Antihydrogen production using trapped plasmas. *Phys. Lett. A*, 129(1):38–42, May 1988. URL http://www.sciencedirect.com/science/article/pii/0375960188904707.

[96] G. Gabrielse, S.L. N.S. Bowden, P. Oxley, A. Speck, C.H. Storry, J.N. Tan, M. Wessels, D. Grzonka, W. Oelert, G. Schepers, T. Sefzick, J. Walz, H. Pittner, T.W. Hänsch, and E.A. Hessels. Background-free observation of cold antihydrogen with field-ionization analysis of its states. *Phys. Rev. Lett.*, 89(21):213401, October 2002. URL http://link.aps.org/doi/10.1103/PhysRevLett.89.213401.

[97] P. Richerme, G. Gabrielse, S. Ettenauer, R. Kalra, E. Tardiff, D.W. Fitzakerley, M.C. George, E.A. Hessels, C.H. Storry, M. Weel, A. Mullers, and J. Walz. Using electric fields to prevent mirror-trapped antiprotons in antihydrogen studies. *Phys. Rev. A*, 87(2):023422, February 2013. URL http://link.aps.org/doi/10.1103/PhysRevA.87.023422.

[98] G. Gabrielse, R.Kalra, W.S. Kolthammer, R. McConnell, P. Richerme, D. Grzonka, W. Oelert, T. Sefzick, M. Zielinski, D.W. Fitzakerley, M.C. George, E.A. Hessels, C.H. Storry, M. Weel, A.Mullers, and J. Walz. Trapped antihydrogen in its ground state. *Phys. Rev. Lett.*, 108(11):113002, October 2012. URL http://link.aps.org/doi/10.1103/PhysRevLett.108.113002.

[99] E.A. Hessels, D.M. Homan, and M.J. Cavagnero. Two-stage rydberg charge exchange: An efficient method for production of antihydrogen. *Phys. Rev. A*, 57(3):1668, March 1998. URL http://link.aps.org/doi/10.1103/PhysRevA.57.1668.

[100] M.L. Wakk, C.S. Norton, and F. Robicheaux. Two-stage rydberg charge exchange in a strong magnetic field. *Phys. Rev. A*, 72(5):052702, November 2005. URL http://link.aps.org/doi/10.1103/PhysRevA.57.1668.

[101] C.H. Storry, A. Speck, D. LeSage, N. Guise, G. Gabrielse, D. Grzonka, W. Oelert, G. Schepers, T. Sefzick, H. Pittner, M. Herrmann, J. Walz, T.W. Hänsch, D. Comeau, and E.A.Hessels. First laser-controlled antihydrogen production. *Phys. Rev. Lett.*, 93(26):263401, December 2004. URL http://link.aps.org/doi/10.1103/PhysRevLett.93.263401.

[102] C.H. Storry, A. Speck, D. LeSage, N. Guise, G. Gabrielse, D. Grzonka, W. Oelert, G. Schepers, T. Sefzick, H. Pittner, M. Herrmann, J. Walz, T.W. Hänsch, D. Comeau, and E.A.Hessels. Laser-controlled production of rydberg positronium via charge exchange collisions. *Phys. Lett. B*, 597(3-4): 263401, September 2004. URL http://dx.doi.org/10.1016/j.physletb.2004.07.044.

[103] A. Muellers, S. Boettner, D. Kolbe, T. Diehl, A. Koglbauer, M. Sattler, M. Stappel, R. Steinborn, J. Walz, G. Gabrielse, R. Kalra, W. S. Kolthammer, R. P. McConnell, P. Richerme, D. W. Fitzakerley, M. C. George, E. A. Hessels, C. H. Storry, M. Weel, D. Grzonka, and W. Oelert. A semiconductor laser system for the production of antihydrogen. *New J. Phys.*, 14(5):055009, May 2012. URL http://iopscience.iop.org/1367-2630/14/5/055009/.

[104] D.A. Steck. Cs d-line data. 2010. URL http://steck.us/alkalidata/cesiumnumbers.pdf.

[105] G. Gabrielse, P. Larochelle, D. Le Sage, B. Levitt, W.S. Kolthammer, I. Kuljanishvili, R. McConnell, J. Wrubel, F.M. Esser, H. Glückler, D. Grzonka, G. Hansen, S. Martin, W. Oelert, J. Schillings, M. Schmitt, T. Sefzick, H. Soltner, Z. Zhang, D. Comeau, M.C. George, E.A. Hessels, C.H. Storry,

M. Weel, A. Speck, F. Nillius, J. Walz, and T.W. Hänsch. Antiproton confinement in a penning-ioffe trap for antihydrogen. *Phys. Rev. Lett*, 98(11): 113002, March 2007. URL http://dx.doi.org/10.1103/PhysRevLett.98.113002.

[106] G. Gabrielse, P. Larochelle, D. Le Sage, B. Levitt, W.S. Kolthammer, R. McConnell, P. Richerme, J. Wrubel, A. Speck, M.C. George, D. Grzonka, W. Oelert, T. Sefzick, Z. Zhang, A. Carew, D. Comeau, E.A. Hessels, C.H. Storry, M. Weel, and J. Walz. Antihydrogen production within a penning-ioffe trap. *Phys. Rev. Lett.*, 100:113001, 2008. URL http://dx.doi.org/10.1103/PhysRevLett.100.113001.